Modelling the Non-linear Dynamics of Polymer Solutions in Complex Flows

A thesis submitted to the University of Manchester for the degree of

Doctor of Philosophy

in the Faculty of Engineering and Physical Sciences

January 2011

Sunday C. Omowunmi

School of Chemical Engineering and Analytical Science

Contents

List of Figures

List of Tables

Nomenclature

β - contraction ratio

χ_L - dimensionless vortex length

Wi - Weissenberg Number

T_R - Trouton ratio

η - shear viscosity

η_p - polymer viscosity

η_s - solvent viscosity

η_E - extensional viscosity

Re - Reynolds number

AR_u - upstream aspect ratio

El - elasticity number

Ma - Mach number

De - Deborah number

λ - relaxation time

$\boldsymbol{\tau}$ - extra stress tensor

$\boldsymbol{\tau}_p$ - polymer stress component

$\boldsymbol{\tau}_s$ - Newtonian (solvent) stress component

$\boldsymbol{\sigma}$ - Cauchy stress tensor

N_1 - first normal stress difference

N_2 - second normal stress difference

Ψ - first normal stress coefficient

Ψ - second normal stress coefficient

ρ - density

$\overset{\triangledown}{\mathcal{A}}$ - upper convected time derivative of $\mathcal{A}$

$\overset{\triangle}{\mathcal{A}}$ - lower convected time derivative of $\mathcal{A}$

$\boldsymbol{A}$ - configuration tensor

$\dot{\boldsymbol{D}}$ - rate of deformation tensor

$\dot{\varepsilon}$ - extensional strain

G' - storage modulus

G'' - loss modulus

D_h - hydraulic diameter

U - mean velocity

Abstract

The flow of polymer solutions in the high Elasticity number, El, regime in complex geometries may lead to strong viscoelastic behaviour and eventually become unstable as the Weissenberg number, Wi, is increased beyond a critical level. So far, the success of numerical simulations in predicting the highly non-linear behaviour of polymer solutions in complex flows has been limited.

In this thesis, selected constitutive models are evaluated under the high El flow regime in the cross-slot and contraction benchmark flows using a numerical technique based on the finite volume method. The numerical technique is implemented within the OpenFOAM framework and thoroughly validated in the benchmark flow. A modification to the FENE dumbbell model based on the non-affine deformation of polymer solutions is proposed, which enabled the prediction of some non-linear material functions and also enhanced numerical stability, allowing a higher Wi to be attained.

Asymmetric flow instability in the cross-slot flow has been studied. Time-dependent stability diagrams were constructed based on Wi and the strain, ε, both of which govern the stretching of a polymer chain. In the contraction flow, elastic instability is simulated for the first time in this geometry. Substantial time-dependent asymmetric flow patterns were predicted as seen in experiments. The effect of the contraction ratio is investigated through a stability diagram. Three-dimensional finite element simulations were also carried out to study the effect of the aspect ratio in the contraction flow of a Phan-Thien-Tanner fluid. The simulations suggest that a lip vortex mechanism is a signature for the onset of strong viscoelastic behaviour.

Declaration

I declare that no portion of the work referred to in the thesis has been submitted in support of an application for another degree or qualification of this or any other university or other institute of learning.

Acknowledgments

I wish to specially thank my supervisor Dr. Xue-Feng Yuan for his support and insightful discussions throughout the course of this research. I wish also to thank Dr. Jeff Odell for his advisory comments during our EPSRC consortium meetings, and my collaborators working on experimental microfluidic systems: Alfredo Lanzaro, Dr. Zhou Li, and Dr. Simon Haward for their contributions to this work. I want to thank Joseph Dawes for his contribution in the area of OpenFOAM. I am grateful to my sponsors: the Overseas Research Scholarship Award Scheme (ORSAS) and the School of Chemical Engineering and Analytical Science (CEAS) for their financial support. Finally, I am heartily grateful to my parents for their support, to Bright for his kindness, and to Blessing for standing by me throughout the writing-up of the thesis.

Dedication

This work is dedicated to the King before whom *"everything flows"* (Judges 5:5 [7, 8]).

Copyright Statement

Part I

Background, Motivation, and Theory

Chapter 1

Introduction

1.1 Rheological Properties of Polymeric Liquids

Polymeric liquids are one of the most extensively studied complex fluids due to their industrial relevance. They are macromolecules with each backbone consisting of one or more repeating structural units. Their common defining feature is the presence of a mesoscopic length scale (typically of the order of 10-100 nm), which is responsible for their characteristic properties. They undergo thermal motions resulting in constantly changing configurations by rotation around chemical bonds. Block copolymers and micellar solutions often self-assemble into supramolecular ordered structures with molecular weight of the order of tens to hundreds of thousands g/mol. Bond interactions between these ordered structures may even lead to the formation of more complex structures with a higher molecular weight.

In rheological flows, the conformation of the macromolecules, namely their orientation and degree of stretch, is continuously modified along the streamlines, and their rheological response is governed by the flow-induced evolution of their microstructure. Their rheological behaviour is determined by the coupling between their microstructure and the local deformation. Due to their mesoscopic length scale the resulting stress on the fluid element is not just related to the instantaneous deformation rate but to the entire deformation history with a fading memory. Elasticity is generated by the fluid when the deformation rate exceeds their characteristic relaxation rate due to thermal motions that restore them to their equilibrium position.

The unique properties of polymeric liquids are exploited in many industrial applications. They are widely used in industrial processes ranging from macro-scale manufacturing processes such as extrusion and blow moulding, to micro-scale technologies such as micro-injection moulding and fibre-spinning. The most common feature of these materials that is of engineering interest is the presence of a shear-rate dependent viscosity, which declines at high deformation rates. Another very important rheological property of these materials is the presence of normal stresses, which is responsible for their rod-climbing or *Weissenberg* effect. They are also characterised by an elongational viscosity that is much larger than that of a Newtonian fluid, a property which is very useful in fibre spinning and ink-jet printing.

1.2 Computational Rheology

Computational rheology involves the design, development and implementation of numerical recipes capable of simulating the complex behaviour of non-Newtonian fluid flows. The scope of the field of computational rheology is usually restricted to materials that can be classified as viscoelastic fluids [9]. The challenge for computational rheologists is to develop accurate numerical schemes based on physically-realistic mathematical models capable of predicting the behaviour of viscoelastic fluids in complex flows. Several years of research have seen the development of various numerical techniques and constitutive models based on macroscopic and microscopic approaches. Models based on the macroscopic description of a viscoelastic fluid express the stress endured by a fluid element in terms of the history of the deformation experienced by that element. This is often called a *constitutive equation*. Microscopic models, on the other hand, do not furnish a closed form constitutive equation without recourse to closure approximations. There are a number of microscopic levels of description of a fluid, namely: kinetic theory, atomistic modelling (non-equilibrium molecular dynamics), and quantum mechanics [10]. A new generation hybrid approach, the micro-macro, such as the CONNFFESSIT (Calculation of Non-Newtonian Flow: Finite Elements and Stochastic Simulation Technique) approach, couples the microscopic scale of the kinetic theory with the macroscopic scale of continuum mechanics [11, 12]. The polymer stress is computed with a stochastic simulation

technique and coupled to a macroscopic flow solver for computing the flow fields.

The numerical solution to the macroscopic models governing the flow of a viscoelastic fluid involves two stages: firstly, the discretization of the governing equations in space (and time for transient flows) to obtain a set of algebraic equations, and secondly, the resulting algebraic equations are solved using a suitable numerical algorithm. Numerical schemes based on classical CFD namely, finite difference, finite elements, finite volume, boundary integral and spectral methods have been applied with appropriate modifications for viscoelastic problems. Such modifications are required because conventional discretization schemes were orignially developed for solving elliptic equations, whereas the governing equations for viscoelastic fluids in strong flows may become hyperbolic in nature. Numerical algorithms for solving the algebraic equations arising from the discretization of the governing equation for viscoelastic flows have also evolved from methods based on classical CFD.

Keunings [13] stated that a rigorous exercise in computational rheology should involve a number of steps including: (1) getting the numbers, and (2) checking their numerical accuracy. Step (1) involves obtaining numerical solutions to the non-linear algebraic equations at significant values of Weissenberg number Wi, which is a measure of the elasticity of a viscoelastic fluid. In step (2) the numerical results obtained are critically evaluated to ensure that they represent sufficiently accurate approximations to the exact solutions of the governing equations.

The task of "getting the numbers" is beset by the infamous High Wessienberg Number Problem (HWNP), which manifests itself in benchmark flows as loss of convergence of numerical algorithms at limiting values of Wi. This problem was first identified in the mid 1970's and has been linked with numerical approximation errors [14]. Although, it might be safe to say that significant progress has been made over the past 30 years on the HWNP, progress in industrial rheology might have been been seriously slowed down by the availability of only very few commercial viscoelastic flow solvers. Moreover, without access to the source codes commercial solvers are highly restrictive in their use.

Traditionally, the accuracy of numerical techniques are often validated through rigorous mesh refinement. These steps of Keunings have been hampered in the past by the need for expensive mesh refinement and lack of sufficient computer resource to handle the

resulting calculations.

1.3 The Benchmark Flow Problem

Contraction flows have been used for many years as a test problem in computational rheology. So far computational rheology has been able to predict some of the phenomena observed in various flow geometries, including: corner vortex growth and lip-vortex growth with increasing elastic character of the fluid; effects of concentration and stretching of polymer chains; effects of the contraction ratio, re-entrant corner curvature, and more recently, effects of the aspect ratio of the geometry [15] on the non-linear dynamics of viscoelastic fluids. Despite these achievements, the accuracy of numerical simulations in predicting complex flow behaviour in this geometry remains very limited.

Using microfluidic geometries, sophisticated experimental techniques in recent times have exposed more intriguing dynamics of viscoelastic fluids [16, 17, 18, 19]. Due to the small characteristic length scales associated with these devices, very high deformation rates can be achieved in them, which can stretch polymer chains by several orders of magnitude compared with their equilibrium size. The experimental techniques are readily accessible by low-viscosity elastic fluids and they can explore the rich non-linear viscoelastic behaviour of dilute polymer solutions in the low to moderate Reynolds number, Re, and high Weissenberg number, Wi, flow regime. The ratio of the Weissenberg number to the Reynolds number is referred to as the elasticity number, $El = Wi/Re$, thus this flow regime is characterised by high El. New unstable elastic flow phenomena have been recently observed in this flow regime in both the contraction [16] and cross-slot [19] flow configurations. These experimental techniques are particularly useful in microfluidic rheometry [20] and for highly stretching industrial flow applications. Such flow regimes will prove very valuable for testing both the validity of viscoelastic models and the robustness of numerical techniques.

1.4 The Aim of the Present Work

The aim of the present research is to numerically investigate the elastic dynamics of polymer solutions in complex flows. The work will evaluate the capability of viscoelastic models to predict observed flow behaviour in the high El flow regime. This work is part of a combined experimental and computational approach to investigate the non-linear dynamics of polymer solutions in microfluidics. The ultimate goal of the research is to develop a better understanding of microfluidic systems for the efficient design and optimisation of these systems in a wide range of applications.

The failure of numerical simulations to predict the behaviour of polymer solutions in complex flows is due to the inability of the constitutive model to mimic some important physics in the flow and/or the breakdown of the numerical techniques at relatively low Weissenberg number, Wi. In order to achieve the present aim, a numerical technique based on the finite volume method will be implemented in the OpenFOAM C++ class library. The robustness of this technique will be evaluated in the contraction benchmark flow by detailed comparisons with a very stable numerical solver [21]. The coarse-grained FENE (Finitely Extensible Non-linear Elastic) dumbbell model and the network-theory based Phan-Thien-Tanner model, which is one of the most advanced macroscopic constitutive models for polymer solutions will be used for this study. The FENE dumbbell model will be refined to better capture the rheological properties of polymer solutions.

This thesis is organised into three parts. The remainder of Part I consists of the literature review and theoretical models. Chapter 2 discusses numerical techniques for viscoelastic flows leading up to the present time, aimed at predicting the behaviour of polymer solutions and overcoming the challenges of the HWNP. It also reviews viscoelastic phenomena that are observed for polymer solutions in the benchmark flow, including the very recent microfluidic experiments mentioned above. In Chapter 3, theoretical models are presented and the proposed modification to the dumbbell model is described. Part II consists of the implementation of the present computational technique, which is discussed in Chapter 4, while the validation of the technique is discussed in Chapter 5. Part III presents numerical simulations of the elastic dynamics of polymer solutions in the cross-channel and contraction geometries. In Chapter 6, elastic instability in the

cross-slot is investigated. The constitutive models are compared in the steady symmetric flow regime and time-dependent stability diagrams are constructed to study the flow transitions. Chapter 7 presents numerical simulations of elastic flow instability in two-dimensional contraction flow for the first time. The constitutive models are evaluated in the high El flow regime by their ability to predict observed flow phenomena. The effects of the fluid inertia and the contraction ratio of the geometry are also investigated. Chapter 8 contains the three-dimensional simulation of a polymer solution in an 8:1 contraction flow using the finite element POLYFLOW solver. A systematic study of the effects of varying the aspect ratio of the channel on the flow fields from a 2-D flow to a strongly 3-D flow is performed. In Chapter 9, the work is summarised and future work is recommended.

Chapter 2

Non-Newtonian Dynamics of Polymer Solutions

2.1 Introduction

Industrial applications of rheological flows abound and there are a wide range of materials that can be classified as "complex" or "viscoelastic" including polymer solutions, melts, emulsions, suspensions, and biological fluids [22]. Many processes involving these materials are characterised by geometries having sharp or slightly rounded corners and often generate strong inhomogeneous flows, such as in extrusion and ink-jet printing. Understanding these flows can be very useful in optimising both the geometric and material designs in order to increase the production rate of such industrial processes.

Computational rheology has focused on the prediction of the behaviour of viscoelastic fluids in benchmark flows, which produce similar flow patterns as obtainable in the industrial processes. In these flow configurations, regions of different flow type often co-exist, including strong shearing flow near the wall, strong extensional flow along the centreline, and other secondary flows as well as mixed flows. In addition, the pressure drop that is usually required to drive the fluid through the flow cell is often considerably greater compared to an equivalent Newtonian fluid. This excess pressure drop provides information about the stretching of polymer molecules, which can be used to quantify the apparent elongational viscosity of the fluid.

A geometry which is commonly used as a benchmark for studying such flows consists

of a converging section followed by an expansion section (see Fig. 2.1). In this geometry, the fluid approaches the contraction region from upstream with an elevated velocity to conserve mass by continuity, and thus generating a velocity gradient in the flow direction. This induces a strong extensional flow in the vicinity of the re-entrant corner, which stretches the polymer molecules as they enter the narrow channel. Immediately downstream of the re-entrant corner, the polymer relaxes due to the entropic restoring force of the chains. Further downstream the memory of the molecules might be completely eliminated as they enter the downstream diverging section for a relatively long re-entrant length.

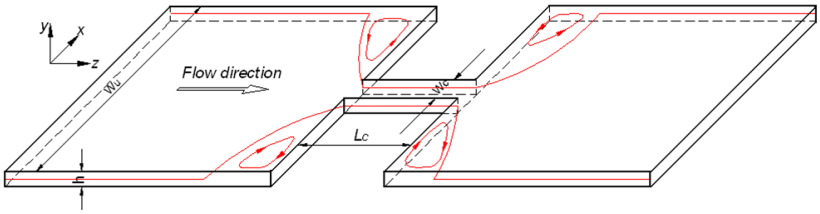

Figure 2.1: A planar contraction-expansion flow cell geometry

The attraction of this geometry is its simplicity and the ease with which it lends itself to experimental studies, yet it can lead to very interesting flow patterns. It had been long established as a benchmark geometry for testing numerical codes. However, early attempts to predict experimental observations in this geometry were largely frustrated by the presence of singularities at the re-entrant corners, which caused the breakdown of numerical codes at significant values of Weissenberg number, a situation which is well-known to rheologists as the High Weissenberg Number Problem (HWNP) [23]. In addition to this numerical limitation, the predictability of numerical simulations was also greatly precluded by the inability of constitutive equations to capture the physics of complex fluids, particularly in the non-linear flow regime. Therefore, the pursuit of computational rheology has been to develop robust numerical techniques as well as modelling approaches capable of predicting the behaviour of viscoelastic fluid in such flows. In the sections following, computational techniques aimed at overcoming the HWNP will be reviewed. Then the progress made in numerical simulations in predicting viscoelastic phenomena in the contraction flow will be discussed as well as some recent experimental techniques.

2.2 Computational Techniques for Viscoelastic Flows

The development of the field of computational rheology has been primarily motivated by the need to predict experimental observations. A series of detailed experimental studies in the contraction flow in the late 70's [24, 25] and in the 80's [26, 27] were very influential in some of the early developments in numerical techniques, which were intended to reproduce the observed flow features. Most of these developments were based on the finite element method and the efforts were driven towards extending the range of Weissenberg number over which a converged solution can be obtained. The hyperbolic nature of viscoelastic constitutive equations, which is complicated by the presence of a singularity in the flow geometry has been identified as the main cause of the loss of convergence of numerical schemes.

The numerical work of Marchall and Crochet [28, 29] was one of the early papers that led the way in developing stable computational techniques for viscoelastic flow problems. In their first attempt [28], the velocity field was interpolated by new Hermitian shape functions, which ensured that the stress approximation spaces are able to represent the velocity field gradient and eliminate spurious oscillations due to steep velocity and stress gradients that occurs at relatively low Wi, thus increasing the range of Wi over which a convergent solutions could be obtained. In their second attempt [29], they proposed a new mixed finite element method, which uses a combination of bilinear sub-elements for the stress and streamline-upwinding (SU) for the constitutive equation. In this method, the resulting non-linear algebraic equations, as with most finite element method, is solved by a fully coupled approach using iterative schemes such as the Newton's method. The disadvantage of such a fully coupled approach is the requirement for large data storage and increased CPU time. Therefore, due to the limitations in computational resource relatively few computational nodes have been used with the finite element method. A decoupled approach may also be used with the finite element method based on Picard iteration, in which the conservation equations and constitutive equation are solved separately with much cheaper resource usage. In their decoupled finite element method, Fortin and Fortin [30] used the streamline-upwinding technique and a new upwinding method, namely the Lesaint-Raviart method to discretise the constitutive equation. The main advantage of

this method is the reduction in the number of degrees of freedom of some field variables, which minimised computational cost but the gain in numerical stability was rather modest. Some of these numerical techniques have been further refined over many years and made available in the finite element solver, POLYFLOW [31], which has been used extensively for modelling complex industrial problems involving simultaneous mass and heat transfer in mixing problems [32], as well as instabilities in extrusion flows [33], and foaming process [34].

The idea of the streamline upwinding (SU) technique of Marchal and Crochet [29] is to modify the test functions used in the constitutive equation in order to add some anisotropic diffusion along the streamlines, which vanishes as the element size reduced to zero. In this method the test function is only modified for the advective term in the constitutive equation, which is often referred to as "inconsistent". The streamline-upwind/Petrov-Galerkin (SUPG) finite element formulation of Brooks and Hughes [35] is consistent in the sense that it applies the same test function to every term in the constitutive equation. Marchal and Crochet showed that SU allowed numerical simulations of the stick-slip problem up to Deborah numbers as high as 27 whereas the SUPG method results in spurious numerical oscillations, thus SU technique achieves stability at the expense of consistency. However, it has been shown that the use of the inconsistent SU method may degrade numerical accuracy in problems containing singularities and large stress gradients whereas both high-order of accuracy and stability may be realised using the SUPG method [36].

Numerical techniques based on other methods for viscoelastic flow problems had also emerged over the past decade. The finite volume method is particularly attractive because of the requirement for less computer memory usage compared with the finite element method. The finite volume method uses iterative schemes rather than direct methods to solve the set of linear algebraic equations resulting from the discretisation of the governing equations. The staggered grid finite volume method seemed to be the precursor of the non-staggered grid arrangement for viscoelastic flow calculations. The non-staggered grid arrangement requires special techniques, such as the Rhie-Chow interpolation to resolve the problem of decoupling of the variables. In both methods special discretisation schemes are required for treating the convection terms in the governing equations.

Earlier authors studying viscoelastic flows used the staggered grid arrangement and one of the predictor-corrector family of algorithms with appropriate modifications for viscoelastic problems. Some of the earlier finite volume calculations for viscoelastic flows to appear in the simulation literature are the works of Yoo and Na [37] and Darwish and Whiteman [38]. Both group of authors used the staggered grid arrangement for the field variables but the SIMPLE (Semi-Implicit Method for Pressure Linked Equations-Revised) and PRIME (PRessure Implicit Momentum Explicit) iterative algorithms, respectively. Yoo and Na [37] discretised the constitutive equations using either central differencing or upwind differencing whilst Darwish and Whiteman [38] used the third-order accurate SMART scheme. The high order calculations of Darwish and Whiteman produced better accuracy compared with the numerical simulations of the other authors but at the cost of solution convergence.

Sasmal [39] presented a finite volume scheme based on a staggered grid arrangement using the upwind differencing and the Elastic Viscous Split Stress (EVSS) method to achieve numerical stability beyond previously reported simulations by finite element calculations. They also implemented a scheme similar in technique to the under-relaxation scheme for their steady-state problem, which satisfies the condition for convergence by increasing the diagonal dominance of the discretised constitutive equation. Although the simulations represent significant progress in developing numerical techniques based on the finite volume method, their work was mainly hampered by limited computer resources and hence the authors could not thoroughly investigate solution convergence with mesh refinement.

Some recent contributions in the finite volume method have been based on the collocated grid arrangement, in which all field variables are located at the centre of the control volumes [21, 40]. The specific advantage of this method over the staggered grid method lies in the ease with which it can be adapted for complex geometries and boundary conditions [41]. The collocated finite volume method of Oliveira et al. [21] was implemented using the SIMPLER algorithm, and the second order accurate linear upwind discretisation scheme for the convection terms in the momentum and constitutive equations. In their subsequent paper [42] they implemented a grid-adaptable multi-resolution scheme for general hyperbolic PDEs, which may be combined with a high resolution schemes

in one-dimension. Later on these authors introduced a new high resolution scheme, CUBISTA (the Convergent and Universally Bounded Interpolation Scheme for the Treatment of Advection) for multi-dimensional viscoelastic problems [43]. Recently, the robustness of this technique was demonstrated by rigorous mesh refinement in the benchmark flow [6], which exceeded any previous benchmark results in terms of the range of Wi attained using similar models and comparable mesh density.

2.2.1 Hybrid Schemes

There are a number of hybrid schemes which have also been very successful in computing viscoelastic flow problems, such as the hybrid finite volume/element scheme [44, 45, 46], in which the conservation equations are discretised by finite element method and the finite volume method is used for the constitutive equation. Other hybrid techniques such as the semi-Lagrangian finite volume method [47] and the semi-Lagrangian finite element method [48] have also been implemented, which calculate the velocity by Eulerian method whilst the stress is treated as a Lagrangian particle. The semi-Lagrangian method is based on a similar philosophy as another evolving hybrid technique, the micro-macro approach, which couples the macroscopic conservation equations with either a FokkerPlanck or stochastic equation for the polymer stress [11, 49]. The polymer stress is calculated by Lagrangian tracking of either individual dumbbells in solution or their ensemble average. Such a technique holds prospects for the implementation of more advanced modelling approaches, such as the unified molecular modelling approach proposed by Shima et al. [50]. The model is based on the Self-Consistent-Field (SCF) theory and the reptation theory and can account for the full conformational information of polymer chains interacting through their potentials. It can be used for modelling both homogeneous and inhomogeneous polymer systems, such as copolymers and polymer mixtures under strong flow conditions.

2.2.2 Recent Developments Towards Overcoming the HWNP

It had been long established that one of the consequences of using inappropriate numerical schemes for modelling viscoelastic flows is usually a breakdown of the numerical solution at critical values of Weissenberg number. The HWNP has provoked several in-

terests in stability analysis of viscoelastic models [51, 52, 36], which associated the cause of the HWNP to the loss of positive-definitiveness of the conformation tensor as a result of numerical errors introduced in the discrete approximation of the continuous system. Such numerical errors deteriorate numerical solutions and they can be exacerbated by the presence of steep boundary layers or large stress gradients in region of a singularity in non-smooth computational domains. In principle, these difficulties should be overcome by either mesh refinement or use of higher-order approximation methods. However, while the latter only delays the onset of the critical Weissenberg number, the former actually has an opposite effect because singularity deteriorates the error estimates of an elliptic problem. Near the corner the error behaves like $O(h^{-s})$ for some exponent $s > 0$ for elliptic problems, where h is the characteristic mesh size [36]. For viscoelastic problems the situation is worsened by the hyperbolic nature of the governing equations. The characteristics of hyperbolic partial differential equations are real and correspond to the streamlines, which implies that errors can be propagated along them [36, 53].

Recently, new techniques have been proposed to overcome the HWNP [54, 55]. One approach [54] proposed the reformulation of the constitutive equation by taking the logarithm of the conformation tensor and re-writing the equations in a (matrix) logarithm form. This so-called log-conformation approach guarantees the positive-definitiveness of the conformation tensor and large stress gradients arising around singularities can be resolved. Calculations obtained by the log-conformation method can reach very high Weissenberg numbers. The numerical stability of this method has been demonstrated by some preliminary computational studies [56, 57]. The flow of the Oldroyd-B fluid past a cylinder was computed by Afonso et al. [57] using this modelling approach in the finite volume method and the CUBISTA differencing scheme. They reported an improvement in the critical Weissenberg number by about 90% compared with their previous simulations obtained by traditional method. However, this technique leads to a decrease in numerical accuracy [58], which is probably due to the effect of the log scaling on numerical approximations.

In a completely different approach [55], the constitutive equation can be recast, in terms of certain Lie derivatives, into formulations which closely resembles the symmetric Riccati differential equations. The idea is to derive a discretisation method that preserves

the positive-definitiveness of the conformation tensor in going from the continuous to the discrete level. However, the robustness of this approach in solving practical problems remains to be demonstrated.

2.3 The Contraction Benchmark Flow

Common flow features that are predicted in the contraction benchmark flow will now be reviewed with particular focus on the works that were carried out within the past decade. As noted before, earlier attempts to predict experimentally observed flow features were frustrated by the HWNP. Purnode and Crochet [59] carried out 2-D numerical simulations using a single-mode FENE-P model and material functions corresponding to three different concentrations of PAA solutions of Evans and Walters [60, 61]. Their computations, although successful in reproducing the essential vortex features observed by Evans and Walters [60, 61] the three different contraction ratios and three different PAA concentrations, they did not occur at the same flow rates. This lack of quantitative agreement was explained by the fact that the computations of Purnode and Crochet [59] were 2-D whereas there were obviously three-dimensional flow effects in the experiments of Evans and Walters [61]. Moreover, they explained that the single-mode FENE-P model used in their simulation may be too simple to fully mimic the complex flow behaviour of PAA solutions [59].

Xue et al. [62] used an implicit finite volume technique to implement 3D time-dependent numerical simulations for a UCM (upper convected Maxwell) fluid having parameters fitted as in the Boger fluids of Walters and Webster [63]. Their simulations show no corner vortex in planar contraction, which was consistent with experimental observation. However, their computation predicted a tiny lip vortex at very low Wi, which grew in size with increasing flow rate, whereas in experimental conditions a lip vortex was only observed at very high Wi for Boger fluids in planar contraction. This discrepancy was also attributed to the fact that the UCM model was too simple to predict the precise physics of Boger fluids at high Wi.

Xue et al. [62, 64, 65] presented time-dependent 3D numerical simulations for the UCM and PTT fluids in the contraction flow based on an implicit finite volume scheme. These

calculations generally showed better predictability of experimental observations compared to previous 2D simulations. They constructed an elasticity number vs Mach number ($El - Ma$) diagram for the flow of a specific fluid in a 4:1 contraction, characterizing vortex mechanisms under the competing influence of elasticity and inertia. The diagram was, however, based on speculations rather than actual simulation results and was used to explain the experiments of Evans and Walters [60], which reported that the dominating vortex mechanism, either the salient corner vortex or the lip vortex mechanism, was determined by the concentration (or viscosity) of the polymer. At low values of El, corresponding to low polymer concentration, inertial effects dominated resulting in a lip vortex mechanism, whereas at high values of El, which described concentrated polymers or polymer melts, a salient corner mechanism dominated. The diagram also speculated an unstable flow regime in the high $El - Ma$ flow region.

Oliveira and Pihno [66] numerically studied the 2-D flow through a 4:1 planar contraction of the UCM and the simplified PTT fluids using a finite volume method based on a collocated grid arrangement. Their computation for the UCM model predicted a lip vortex enhancement mechanism, which is observed for Boger fluids in axisymmetric contractions [67, 63] and shear-thinning fluids in planar contractions [60]. The appearance of a lip vortex for the flow of Boger fluids in planar contractions is supported by previous numerical simulations [62, 68] but it was not observed in experiments. The predicted lip vortex mechanism for the UCM model was also characterized by a single remaining vortex not seen in previous numerical simulations. This was explained by the fact that the other authors did not pursue their calculations up to high enough Weissenberg number where this feature was predicted. The predicted flow patterns for the simplified PTT fluid were also consistent with experimental observations.

A hybrid finite volume/finite element method was used by Aboubacar et al. [69, 70] to study the flow of viscoelastic fluids using the Oldroyd B and the PTT models, in planar and axisymmetric 4:1 sharp and rounded-corners contractions. Their combined finite volume/finite element method solves the momentum equations by a finite element method, whereas the constitutive equation is solved by a finite volume scheme. The predictions for the Oldroyd-B and the PTT models in the planar sharp-corner contractions were consistent with the results of previous simulations [62, 66, 68]. In the axisym-

metric sharp-corner contraction, the Oldroyd-B fluids exhibited vortex enhancement in agreement with experimental observations for Boger fluids. No lip vortex activity was predicted for axisymmetric or rounded-corner contractions.

Alves and his co-workers [71, 72, 73, 74] carried out a number of numerical studies on the UCM, Oldroyd-B and PTT fluids in planar contractions of various contractions ratios up to 100. They used a finite volume method and the CUBISTA differencing scheme to represent the stress derivative in the constitutive equation, reporting that the scheme avoids oscillations of the solution field near sharp stress gradients. The prediction of the flow patterns for contraction ratios $\beta \geq 4$ showed that vortex enhancement follows a lip vortex mechanism in agreement with the visualization of Evans and Walters [60]. However, the attempt to use the material functions obtained by fitting the model to the experimental data in their calculations gave only a semi-quantitative agreement with experimental measurements.

Recently, Oliveira et al. [75] studied the effects of contraction ratios $2 \leq \beta \leq 100$ on viscoelastic flow through an axisymmetric contraction using the Oldroyd-B and the PTT models, for a wide range of Wi. The authors constructed vortex pattern maps, with contraction ratio and Weissenberg number as independent parameters, which demonstrated the role of these dimensional groups in controlling vortex growth dynamics and pressure-drop characteristics. The authors also studied the effect of the extensional parameter of the PTT model ($0 \leq \epsilon \leq 0.5$) on the Couette correction. Their results showed that for small values of ϵ, the Couette correction of the PTT model is a monotonic decreasing function of Wi whilst for high values of ϵ it is a monotonic increasing function.

2.3.1 Some Experimental Studies in Microfluidics

The sudden contraction-expansion microfluidic geometry may be used to generate strong viscoelastic flows. The geometry is useful for studying flows obtainable in microfluidic polymer processing applications, such as micro-injection moulding, fibre spinning, and film blowing, as well as in micro-rheometric devices. In particular, the flow configuration resembles a number of features in an inkjet printhead where the extensional flow of a non-Newtonian fluid is manipulated to control the rate at which droplets are formed. A number of experimental works have been carried out on viscoelastic fluids in such

geometries [67, 76] mainly using Boger fluids, which are specially prepared such that their viscosity is high enough to eliminate inertial effect. The justification for studying such fluids was based on the need to develop robust numerical methods [77]. Boger fluids are often very dilute solutions and hence they can be described by relatively simple constitutive equations, thereby eliminating the complexity introduced by complicated constitutive equations in developing numerical methods for modelling such flows. The low to moderate Re and high Wi (i.e high El) viscoelastic flow regimes have also been explored by recent experimental techniques in the literature [16, 78, 79, 80].

Rothstein and McKinley [78] experimentally studied the flow of a dilute monodispersed PS/PS Boger fluid through a 4:1:4 axisymmertic contraction-expansion geometry for a wide range of Weissenberg number. Using digital particle image velocimetry (DPIV) for visualization and velocity field measurements, the authors observed large upstream growth of the corner vortex with increasing Wi. Their pressure measurements showed a large extra pressure drop, which they attributed to non-linear hydrodynamic coupling in the strong inhomogeneous extensional flow near the contraction plane. According to the authors, this resulted in an additional dissipative contribution to the polymeric stress, which manifested as the large extra pressure drop. This extra pressure drop was not previously predicted by numerical simulation. In a separate experiment in axisymmetric contraction-expansion flow with contraction ratios $2 \leq \beta \leq 8$, Rothstein and McKinley [81] studied the role of transient extensional rheology on vortex growth mechanism. Their results showed that the role of contraction ratio on vortex growth dynamics may be rationalized by using a dimensionless ratio of the elastic normal stress difference in steady shear flow to that in transient uniaxial flow.

Nigen and Walters [79] investigated the vortex behaviour and pressured drop in the flow of two Boger fluids in both axisymmetric and planar contractions of various contraction ratios $2 \leq \beta \leq 32$. This experiment demonstrated the surprisingly different behaviour of Boger fluids in axisymmetric and planar contractions. Large vortices were observed in the axisymmetric contraction, but virtually none in the planar case. Moreover, in the planar contraction it was impossible to distinguish between Newtonian and Boger fluids of the same shear viscosity, so far as pressure drop was concerned, whereas in the axisymmetric case the Boger fluids exhibited an enhanced pressure drop.

Recently Rodd et al. [16, 80] presented the visualization of some slightly shear-thinning polymer solutions in the contraction-expansion microfluidic geometry having a contraction ratio of 16:1. In their first paper [16], the authors reported the flow of dilute to semi-dilute polymer solutions for a wide range of Wi and for elasticity number ranging between $3.8 \leq El \leq 89$ for the first time in this flow geometry. This achievement was explained by the small characteristic length scale of the device. Within this range many interesting flow regimes were observed as well as significant vortex enhancement of up to 200%. From their experimental results they presented a $Wi - Re$ operating space diagram representing the various flow regimes observed. A number of flow regimes were identified including a Newtonian-like flow at low Wi, steady viscoelastic flow, unsteady asymmetric flow, and unsteady diverging flow with vortex growth. In their second paper [80], they conducted similar experiments using dilute polymer solutions with the aim of studying the effect of the solvent viscosity on the flow patterns, which showed similar flow patterns as obtained by varying the fluid concentration.

A large number of experiments have also been conducted in our laboratory [82, 83, 84, 85] using microfluidic contraction geometries showing many interesting flow features as described above, which depicts that these highly non-linear flow behaviours are a result of the combination of the length scales of the geometry and the high El. Investigations were also conducted to study the effect of the fluid inertia and the contraction ratio on the flow patterns. Many of these results showed time-dependent asymmetric vortex structures at high El, and the tendency of the fluid to remain in that state were opposed by the influence of increasing fluid inertia or decreasing contraction ratio of the geometry.

2.4 Summary

The development of computational techniques with the aim of overcoming the HWNP encountered in viscoelastic flows have been discussed from early developments to the current state of the research. This subject remains an active area of research in computational rheology. Numerical simulations and experimental research in the contraction geometry has also been reviewed. Although numerical simulations have achieved significant success with regards to the HWNP and in predicting some of the observed flow features in this

geometry, it is obvious that it has not yet attained its full capability, especially in simulating features observed in microfluidic flows. Recent experiments show that the physics of polymer molecules (even in very dilute amount) in microfluidic devices is very rich. Instability phenomena are readily accessible in these geometries using relatively low-viscosity polymer solutions due to very high elasticity numbers achievable in them. This opens up a new research area for computational rheology to explore these flow regimes based on simple constitutive equations that could capture at least the salient physics of dilute polymer solutions in flow.

Chapter 3

Theoretical Models

3.1 Introduction

The starting point of modelling a viscoelastic fluid is to define a suitable constitutive model that describes the behaviour of the fluid. This may be derived from first principle based on classical theories such as the polymer network theory. Models may also be derived less rigorously from existing models based on a simple molecular concept. The constitutive equation together with the conservation laws for mass and linear momentum yield a closed set of partial differential equations that can be solved by means of a suitable grid-based numerical scheme. A viscoelastic fluid may also be described in terms of its microstructural dynamics based on the molecular theory. In this case, the parameters appearing in the resulting models have direct physical interpretations with respect to molecular quantities. In such models a suitable closure approximation is required to furnish a closed-form constitutive equation which can be solved by conventional CFD techniques.

3.1.1 Theory of Polymer Models

Although the behaviour of macromolecules in solutions or melts can be quite complicated, the understanding of these systems has been greatly enhanced by the use of mechanical models. This is possible because their macroscopic behaviour is dominated by their macro scale properties due to the large size of macromolecules. Polymer molecules can be ide-

alised by a system of beads which are joined together by rigid rods or interconnecting springs subject to Brownian motion and hydrodynamic interactions with neighbouring molecules. The multiplicity of the interactions between the macromolecules may be simplified by expressing the relationship of the behaviour of a single molecule to the average behaviour of its neighbours using the idea of a surrounding tube, which was introduced by de Gennes [86] and formalised mathematically by Doi and Edwards [87]. These interactions may be summed up in a drag tensor, which depends on the position vector of the molecules and increases with chain length [88].

In dilute solutions the concept is much simpler because the molecules are far apart and hydrodynamic interaction is restricted to the respective molecules. The polymer molecules may be described by single-chain dynamics, such as the Rouse chain or the Rouse-Zimm chain using essentially three model parameters: the number of beads, the Hookean force constant, and hydrodynamic friction coefficient. The Rouse model has successfully predicted some of the linear viscoelastic properties including the zero-shear rate viscosity and multiple relaxation modes in dilute polymers. Because of the mathematical complexities of the dynamic equations of the Rouse chain, calculations of the non-linear rheological behaviour of dilute polymers are often reduced down to just two beads and an interconnecting spring - the elastic dumbbell. The elastic dumbbell model is probably the crudest idealisation of polymer molecules, which is capable of predicting their basic conformational changes such as orientation and stretch. Despite their inherent simplicity they have proven very useful in developing understanding of the relation between polymer chain dynamics and rheological phenomena [89].

However, the elastic dumbbell model cannot describe some important non-linear behaviour of dilute polymers and the linear spring force law on which it is based has to be modified to facilitate the prediction of non-linear material functions. The predicting ability of the model may also be enhanced by introducing the concept of a variable drag coefficient which depends on the dumbbell end-to-end distance. In this chapter, these modifications are presented and a further refinement of this model, based on the non-affine kinematics of polymer solutions, will be described. The Phan-Thien-Tanner model will also be presented.

3.2 The Linear Elastic Dumbbell Kinetic Theory

In the dumbbell kinetic theory, polymer chains are represented as beads and interconnecting springs suspended in a Newtonian solvent. Consider 2 beads having position vectors $\boldsymbol{r}_1$, $\boldsymbol{r}_2$ connected by an entropic spring. Neglecting hydrodynamic interaction we can write the equation of motion for the beads as the resultant of the spring force, $\boldsymbol{F}_i^S$, the drag force, $\boldsymbol{F}_i^D$, and the Brownian force, $\boldsymbol{F}_i^B$, acting on the ith bead as [36]

$$m_i \frac{d^2\boldsymbol{r}_i}{dt^2} = \boldsymbol{F}_i^S + \boldsymbol{F}_i^D + \boldsymbol{F}_i^B, \quad i = 1, 2, \tag{3.1}$$

where $\boldsymbol{F}_i^D$ is defined by Stokes law as

$$\boldsymbol{F}_i^D = -\zeta_i \left(\frac{d\boldsymbol{r}_i}{dt} - (\boldsymbol{v}_0 + (\nabla \boldsymbol{v})^T \boldsymbol{r}_i) \right) \tag{3.2}$$

$\boldsymbol{v} = \boldsymbol{v}_0 + (\nabla \boldsymbol{v})^T \boldsymbol{r}_i)$ is the solvent velocity, m_i is mass of the bead, and $\zeta_i = 6\pi\eta_s a_i$ is the hydrodynamic drag coefficient, which depends on the bead dimensions, a_i, and the solvent viscosity, η_s. The Brownian force on the bead may be written in terms of the configuration distribution function ψ as

$$\boldsymbol{F}_i^B = -kT \frac{\partial}{\partial \boldsymbol{r}_i} \ln\psi \tag{3.3}$$

in which k is a constant and T is the temperature. Taking $\boldsymbol{Q} = \boldsymbol{r}_2 - \boldsymbol{r}_1$ as the dumbbell end-to-end vector, the continuity equation for ψ can be written as

$$\frac{\partial \psi}{\partial t} + \frac{\partial}{\partial \boldsymbol{Q}} \cdot \boldsymbol{J} = 0 \tag{3.4}$$

which represents the probability balance between ψ and the probability flux vector, $\boldsymbol{J} = \dot{\boldsymbol{Q}}\psi$ [36].

The Fokker-Planck equation can be obtained by combining Eq. 3.1-3.4 and making the following assumptions: 1) the acceleration of the beads is negligible 2) the hydrodynamic drag has no dependence on the orientation of the bead under consideration (i.e. non-deformable spherical beads), and it can be averaged out as $\zeta = \zeta_1 = \zeta_2$. The Fokker-Planck equation can be written as [89]

$$\frac{\partial \psi}{\partial t} + ((\nabla \boldsymbol{v})^T \boldsymbol{Q}) \cdot \frac{\partial \psi}{\partial \boldsymbol{Q}} - \frac{2kT}{\zeta} \frac{\partial^2 \psi}{\partial \boldsymbol{Q}^2} - \frac{2}{\zeta} \frac{\partial}{\partial \boldsymbol{Q}} \cdot (\psi \boldsymbol{F}^s) = 0 \tag{3.5}$$

From Eq. 3.5 the evolution equation for the microstructure may be derived [89]

$$\frac{D}{Dt}\langle \boldsymbol{QQ}\rangle - (\nabla \boldsymbol{v})^T\langle \boldsymbol{QQ}\rangle - \langle \boldsymbol{QQ}\rangle(\nabla \boldsymbol{v}) = \frac{4kT}{\zeta}\boldsymbol{I} - \frac{4}{\zeta}\langle \boldsymbol{QF^s}\rangle \tag{3.6}$$

in which $\langle\cdot\rangle$ is an ensemble average. Recognising the left hand side as the upper convected derivative, and using the Hookean spring force law, $\boldsymbol{F}^s = H\boldsymbol{Q}$ (where H is the spring force constant), we have

$$\overset{\triangledown}{\langle \boldsymbol{QQ}\rangle} = \frac{4kT}{\zeta}\boldsymbol{I} - \frac{4H}{\zeta}\langle \boldsymbol{QQ}\rangle \tag{3.7}$$

Defining the conformation tensor $\boldsymbol{A} = \langle \boldsymbol{QQ}\rangle H/kT$ and simplifying gives

$$\overset{\triangledown}{\boldsymbol{A}} = -\frac{1}{\lambda}(\boldsymbol{A} - \boldsymbol{I}) \tag{3.8}$$

where $\lambda = \zeta/2H$ is the relaxation time. The extra stress tensor may be recovered from $\boldsymbol{A}$ by using the Kramers expression,

$$\boldsymbol{\tau} = 2\eta_s\boldsymbol{D} + \frac{\eta_p}{\lambda}(\boldsymbol{A} - \boldsymbol{I}) \tag{3.9}$$

where η_s is the solvent viscosity, $\eta_p = nkT\zeta/2H$ is the polymer viscosity, and $\boldsymbol{D}$ is the rate of deformation tensor, defined by $\boldsymbol{D} = 1/2(\nabla \boldsymbol{v} + (\nabla \boldsymbol{v})^T)$. With appropriate substitutions using Eq. 3.8 and 3.9 we arrive at the Oldroyd-B constitutive equation [36],

$$\boldsymbol{\tau} + \lambda\overset{\triangledown}{\boldsymbol{\tau}} = 2\eta\Big(\boldsymbol{D} + \frac{\lambda\eta_s}{\eta_s + \eta_p}\overset{\triangledown}{\boldsymbol{D}}\Big) \tag{3.10}$$

in which $\eta = \eta_s + \eta_p$ is the zero shear viscosity, and the expression $\frac{\lambda\eta_s}{\eta_s+\eta_p}$ is often referred to as the retardation time. $(^{\triangledown})$ is the upper convected derivative defined for an arbitrary tensor, $\mathcal{A}$, as follows

$$\overset{\triangledown}{\mathcal{A}} = \frac{\partial \mathcal{A}}{\partial t} + \boldsymbol{v}\cdot\nabla\mathcal{A} - (\nabla \boldsymbol{v})^T\cdot\mathcal{A} - \mathcal{A}\cdot\nabla\boldsymbol{v} \tag{3.11}$$

The extra stress tensor, $\boldsymbol{\tau}$, may be written in terms of the contribution of the Newtonian stress tensor, $\boldsymbol{\tau}_s$, and the elastic stress tensors, $\boldsymbol{\tau}_p$

$$\boldsymbol{\tau} = \boldsymbol{\tau}_s + \boldsymbol{\tau}_p \tag{3.12}$$

in which

$$\boldsymbol{\tau}_s = 2\eta_s\boldsymbol{D} \tag{3.13}$$

and

$$\boldsymbol{\tau}_p + \lambda \overset{\triangledown}{\boldsymbol{\tau}}_p = 2\eta_p \boldsymbol{D} \tag{3.14}$$

The advantage of constitutive equations is their tractability by conventional computational techniques. Such techniques are desirable because of the mathematical complexities of viscoelastic problems, which often make them computationally very expensive.

3.3 The FENE-dumbbell Model

The linear elastic dumbbell model is very limited its use because it can only describe some of the linear viscometric functions of polymer solutions and requires further refinement to improve its predictability. The attractive feature of this model compared with the macroscopic models such as Oldroyd-B is the important microstructural information it contains which is coupled directly with the flow. Although macroscopic models have proven successful in predicting some of the rheological behaviour of polymeric fluids, essential microscopic physics may be masked by computing the stress directly from the macroscopic velocity field. Moreover, a model based on the evolution of the microstructure can provide more direct connection between rheological behaviours and the microstructural conformation of polymer chains.

3.3.1 Non-linear Spring Force Laws

The finitely extensible non-linear elastic (FENE) dumbbell model was introduced through the non-linear spring force law, $\boldsymbol{F} = f(Q)H\boldsymbol{Q}$ [90], in which $f(Q) = 1/(1 - (Q^2/L^2))$ is a non-linear function, $Q^2 = \mathrm{tr}\boldsymbol{A}$ is the dumbbell extension, and L is the ratio of the length of a fully extended dumbbell to its equilibrium configuration. With the closure approximation due to Peterlin [91], the function $f(Q)$ can be approximated by

$$\langle f(Q) \rangle = \frac{1}{1 - \langle Q^2/L^2 \rangle} \tag{3.15}$$

to enable the derivation of the FENE-P constitutive equation that can be written as

$$\overset{\triangledown}{\boldsymbol{A}} = -\frac{1}{\lambda}(\langle f(Q) \rangle \boldsymbol{A} - \boldsymbol{I}) \tag{3.16}$$

The Rallison and Chilcott [92] version of the FENE dumbbell model may be derived from this model by replacing the expression $(\langle f(Q)\rangle \boldsymbol{A} - \boldsymbol{I})$ in Eq. 3.16 by $\langle f(Q)\rangle(\boldsymbol{A} - \boldsymbol{I})$. With this modification by Rallison and Chilcott the model predicts a constant shear viscosity. In both models, the finite extensibility of the dumbbell is preserved as well as many other features. However, the Peterlin approximation does not predict accurately the extensional viscosity in time-dependent flows [93].

3.3.2 Conformation-Dependent Hydrodynamic Drag

The physical mechanism by which large stresses rapidly build up in dilute polymer solutions have long been of interest to researchers in both theoretical and experimental rheology [94, 95], and this has led to different concepts of an unravelling polymer chain (see Fig. 3.1). The physical idea that has been developed to explain this large stress over the years is that of a bead friction coefficient that depends strongly on the interbead distance of the dumbbell through a non-linear friction law [1, 96, 97]. This principle of conformation-dependent hydrodynamic drag assumes that as a chain becomes extended by the flow, the strength of the hydrodynamic friction on the dumbbell will increase as a result of the increased size that the flow can grasp. Thus the spring force will increase rapidly in order to counterbalance the increase in the drag force. In effect, the non-linear hydrodynamic assumption may be viewed as a direct modification to the linear spring force law (see Appendix A).

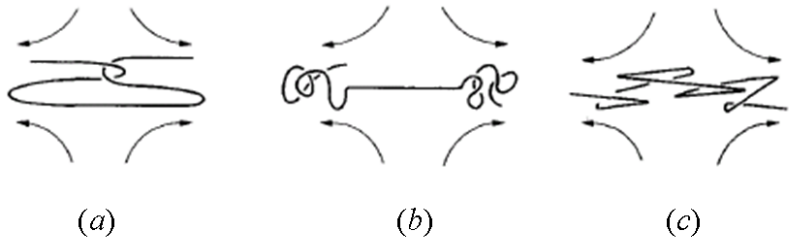

Figure 3.1: Simple models for the unraveling of a single chain [1] (a) knots [2] (b) yo-yo [3] (c) kink [4]

To incorporate conformation-dependent drag in the FENE model, the friction coefficient is expressed as a non-linear function of the configuration tensor using a one parameter

family, $h(\mathrm{tr}\boldsymbol{A})$, which may be written in the form [98],

$$h(\mathrm{tr}\boldsymbol{A}) = 1 - \kappa + \kappa\sqrt{\frac{1}{2}\mathrm{tr}(\boldsymbol{A})} \tag{3.17}$$

which leads to the following modification to the FENE-CR model

$$\overset{\triangledown}{\boldsymbol{A}} = -\frac{\langle f(Q)\rangle}{\lambda h(\mathrm{tr}(\boldsymbol{A}))}(\boldsymbol{A} - \boldsymbol{I}) \tag{3.18}$$

In this model, $\kappa = 0$ corresponds to the constant friction FENE-CR model, $\kappa = 1$ to the FENE-CD model (where CD refers to conformation-dependent) due to Hinch [96] and de-Gennes [97], and $\kappa = 0.02$ to the Larson version of the model [1]. In this form, the shear and extensional rheology of the FENE-CR model is altered. The FENE-CD model predicts a shear-thickening behaviour for the shear viscosity and a first normal stress coefficient which initially grows with shear rate before shear thinning. The elongational viscosity grows faster compared with the constant friction model, with increasing strength of the hydrodynamic drag force which is determined by κ.

3.3.3 The FENE-CD-JS Model

Although the FENE-CD model contains an important physical mechanism, it is relatively crude and requires further refinements. As noted above it predicts a shear-thickening shear viscosity at low shear rates because of the increase in viscous drag introduced by the non-linear hydrodynamics. This is clearly an unwanted feature in dilute polymer solutions. Experimental studies showed that Boger fluids may exhibit shear-thickening behaviour but only at high shear rates [99]. It is believed that this anomaly in the FENE-CD model is due to the dumbbell being stretched excessively in simple shear flow, whereas in such weak flows the polymer chain should only be stretched by a magnitude which is close to the random coil size (≈ 3) [100]. The second shortcoming of the model is that it predicts a vanishing second normal stress difference, whereas experimental measurements show that dilute polymer solutions actually possess a second normal stress difference [101].

The present modification is based on the non-affine deformation of the polymer solutions. Non-affine deformation of polymer chains had been reported in the time-dependent simulation of a single dumbbell chain in a dilute solution [4]. The evolution of the dumbbell with time predicted that the chain initially followed the flow *affinely* until the onset of

strong extensional flow, in which they began to slip by about 65%. This modification can be readily effected in the FENE dumbbell model by replacing the upper-convected time derivative by the Johnson-Segalman (J-S) derivative [102]. This concept was developed from the polymer-network theory and it is based on the assumption that junctions within the network do not follow the imposed macroscopic velocity field exactly [103] in strong flows. Replacing the upper convected time derive in the FENE-CD model (Eq. 3.18) by the J-S derivative gives the FENE-CD-JS model,

$$\overset{\triangledown}{\boldsymbol{A}} + \frac{1}{2}\xi(\boldsymbol{D}\cdot\boldsymbol{A} + \boldsymbol{A}\cdot\boldsymbol{D}) = -\frac{\langle f(Q)\rangle}{\lambda h(\mathrm{tr}(\boldsymbol{A}))}(\boldsymbol{A}-\boldsymbol{I}) \tag{3.19}$$

where ξ is a slip parameter. With this modification, this model now predicts a shear-thinning shear viscosity and a non-zero second normal stress coefficient. It also represents a general form of the Chilcott and Rallison version of the FENE dumbbell model and other forms of the model may be obtained by the choice of model parameters, ξ and κ, as listed in Table 3.1.

Model parameters	Model
$\xi = \kappa = 0$	FENE-CR with constant friction coefficient
$\xi = 0,\ \kappa = 0.02$	FENE-CD with Larson friction law
$\xi = 0,\ \kappa = 1$	FENE-CD with Hinch and de Gennes friction law
$\xi = 0,\ 0.02 < \kappa < 1$	FENE-CD with intermediate friction law
$0 < \xi \leq 1,\ 0.02 \leq \kappa \leq 1$	FENE-CD-JS

Table 3.1: The FENE-CD-JS dumbbell model

Fig. 3.2 shows the prediction of the model in simple shear and uniaxial elongational flows for a range of model parameters. The FENE-CR model is recovered in the limit case $\xi = \kappa = 0$, which predicts a constant shear viscosity and a bounded extensional viscosity at the same level as FENE-CD ($\xi = 0$) and FENE-CD-JS ($\xi = 0.075$) when $\kappa = 0$. For the FENE-CD model, a shear-thickening shear viscosity is predicted but with $\xi = 0.075$ the model now becomes shear-thinning at $Wi \approx 1$, which is also the onset of shear-thickening in the original FENE-CD model. The plots also show that for the non-linear drag model the peak of the elongational viscosity is slightly elevated as κ is increased.

The prediction of the normalised first normal stress difference coefficient is plotted

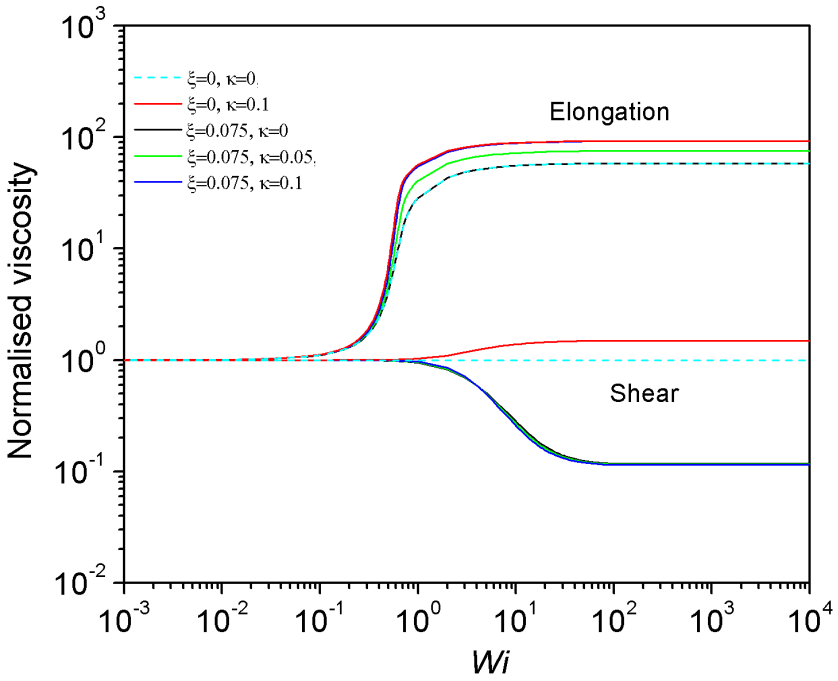

Figure 3.2: Profiles of shear viscosity and elongational viscosities of the FENE-CD-JS model ($L^2 = 100$) in simple shear flow. All the values have been normalised using η_0. On the plot the models represented by $\xi = 0$, $\kappa = 0$ is FENE-CR, and $\xi = 0$, $\kappa > 0$ is FENE-CD

in Fig. 3.3, the and second normal stress difference coefficient in Fig. 3.4. The model predicts a ratio of the second normal stress difference to the first normal stress difference given by $N_2/N_1 = -0.25\xi$, which is within the range measured in experiments [101] as well as that predicted by some phenomenological models such as the Phan-Thien-Tanner model, which predicts $N_2/N_1 = -0.5\xi$, and the Giesekus model, which predicts values within the range $0 \leq N_2/N_1 \leq -0.5\alpha$.

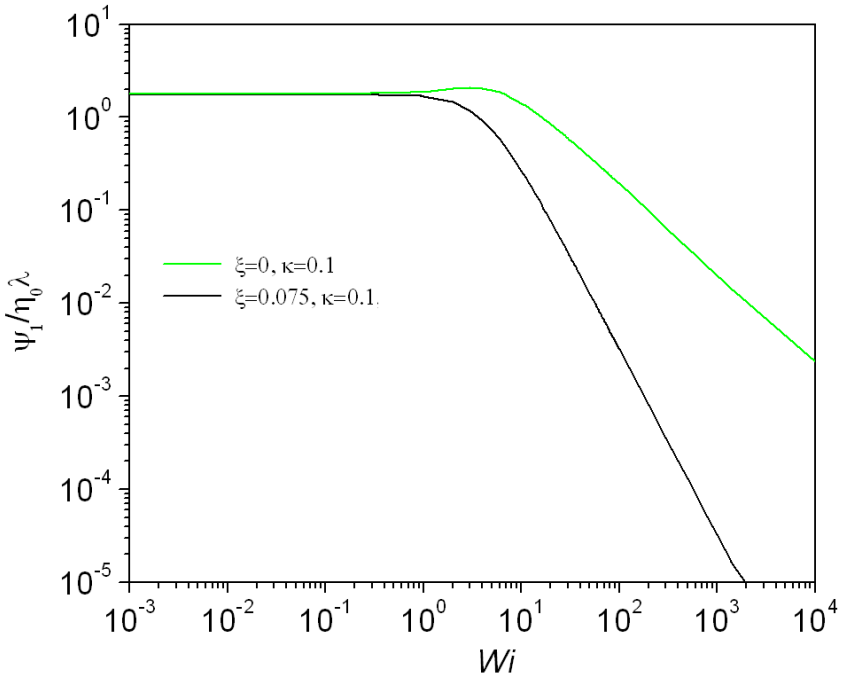

Figure 3.3: Profiles of the first normal stress coefficient of the FENE-CD-JS model ($L^2 = 100$) in simple shear flow

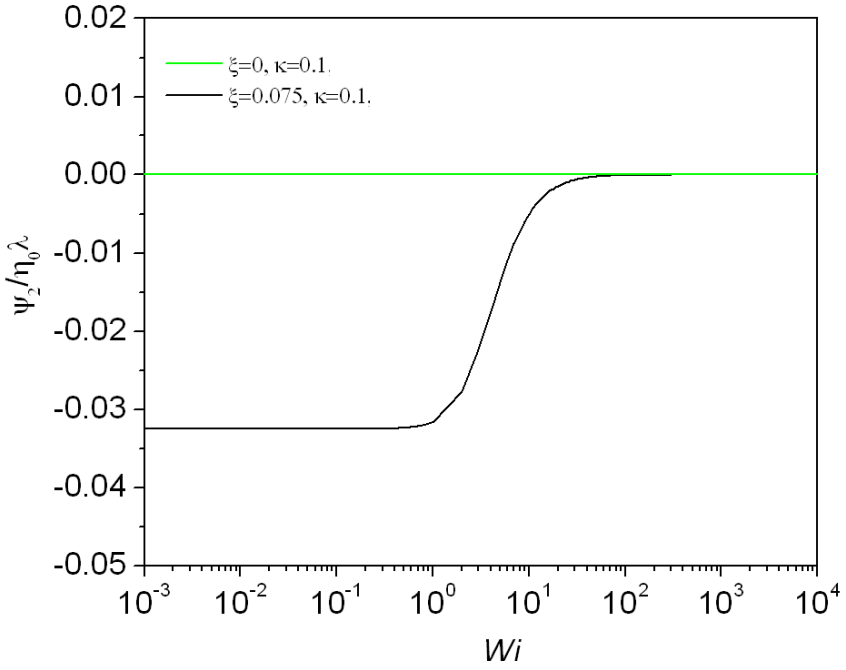

Figure 3.4: Profiles of the second normal stress coefficient of the FENE-CD-JS model ($L^2 = 100$) in simple shear flow

3.4 Differential Viscoelastic Models

The simplest differential constitutive model is the Oldroyd-B model. To account for non-linear viscoelastic behaviour at high rate of deformation (such as shear-thinning, bounded extensional viscosity, and non-zero second normal stress difference), additional terms are incorporated into the differential constitutive equation. A general form of these equations may be written as

$$\boldsymbol{\tau}_p + \lambda \overset{\triangledown}{\boldsymbol{\tau}}_p + \boldsymbol{f}(\boldsymbol{\tau}_p, \boldsymbol{D}) = 2\eta_p \boldsymbol{D} \tag{3.20}$$

in which $f(\boldsymbol{\tau}_p, \boldsymbol{D})$ is a function which depends on the stress tensor, τ_p, and the rate of deformation tensor, $\boldsymbol{D}$. The function is defined in Table 3.2 for some constitutive models which are based on the Oldroyd-B model.

model	$\boldsymbol{f}(\boldsymbol{\tau}_p, \boldsymbol{D})$	model parameter
Oldroyd-B	0	-
Johnson-Segalman	$\frac{1}{2}\xi\lambda(\boldsymbol{D}\cdot\boldsymbol{\tau}_p + \boldsymbol{\tau}_p\cdot\boldsymbol{D})$	ξ
Phan-Thien Tanner	$Z(\boldsymbol{I}_{\boldsymbol{\tau}_p})\boldsymbol{\tau}_p + \frac{1}{2}\xi\lambda(\boldsymbol{D}\cdot\boldsymbol{\tau}_p + \boldsymbol{\tau}_p\cdot\boldsymbol{D})$	ϵ, ξ
	$Z(\boldsymbol{I}_{\boldsymbol{\tau}_p}) = \begin{cases} \frac{\epsilon\lambda}{\eta_p} tr(\boldsymbol{\tau}_p), \text{Linear PTT} \\ \\ \exp[\frac{\epsilon\lambda}{\eta_p} tr(\boldsymbol{\tau}_p)] - 1, \text{Exponential PTT} \end{cases}$	

Table 3.2: A general form for differential constitutive model

3.4.1 The Johnson-Segalman Model

As noted before the Johnson-Segalman model is based on an assumption that relaxes the affine deformation constraint in polymer networks so that the junctions do not follow the macroscopic velocity field exactly. It is given by

$$\boldsymbol{\tau}_p + \lambda \overset{\triangledown}{\boldsymbol{\tau}}_p + \frac{1}{2}\xi\lambda(\boldsymbol{D}\cdot\boldsymbol{\tau}_p + \boldsymbol{\tau}_p\cdot\boldsymbol{D}) = 2\eta_p\boldsymbol{D} \tag{3.21}$$

The limiting cases of the model are given as follows. For $\xi = 0$, the upper convective time derivative is obtained and the model reverts to Oldroyd-B, for $\xi = 2$, the lower convected time derivative is obtained,

$$\overset{\triangle}{\boldsymbol{\tau}}_p = \frac{\partial \boldsymbol{\tau}_p}{\partial t} + \boldsymbol{v}\cdot\nabla\boldsymbol{\tau}_p + \nabla\boldsymbol{v}\cdot\boldsymbol{\tau}_p + \boldsymbol{\tau}_p\cdot(\nabla\boldsymbol{v})^T \tag{3.22}$$

and for $\xi = 1$, the co-rotational time derivative is obtained,

$$\overset{\circ}{\boldsymbol{\tau}}_p = \frac{\partial \boldsymbol{\tau}_p}{\partial t} + \boldsymbol{v} \cdot \nabla \boldsymbol{\tau}_p + \boldsymbol{W} \cdot \tau_p - \boldsymbol{\tau}_p \cdot \boldsymbol{W} \tag{3.23}$$

3.4.2 The Phan-Thien-Tanner Model

The PTT model adopts the Johnson-Segalman derivative in the Oldroyd-B model as well as further expressions for the relaxation time, λ, as a function of the invariants for the stress tensor.

$$\boldsymbol{\tau}_p + \lambda \overset{\triangledown}{\boldsymbol{\tau}}_p + Z(\boldsymbol{I}_{\boldsymbol{\tau}_p})\boldsymbol{\tau}_p + \frac{1}{2}\xi\lambda(\boldsymbol{D} \cdot \boldsymbol{\tau}_p + \boldsymbol{\tau}_p \cdot \boldsymbol{D}) = 2\eta_p \boldsymbol{D} \tag{3.24}$$

where $Z(\boldsymbol{I}_{\boldsymbol{\tau}_p})$ is a scalar function which depends on the first invariant of the stress tensor, $\boldsymbol{I}_{\boldsymbol{\tau}_p}$. For $Z(\boldsymbol{I}_{\boldsymbol{\tau}_p}) = \frac{\epsilon\lambda}{\eta_p} tr(\boldsymbol{\tau}_p)$, the Linear PTT model is obtained, when $Z(\boldsymbol{I}_{\boldsymbol{\tau}_p}) = \exp[\frac{\epsilon\lambda}{\eta_p} tr(\boldsymbol{\tau}_p)] - 1$, the exponential form of the model is obtained. Strain-hardening of the model is due to ϵ. For the exponential form, the elongational viscosity rises through a peak and then declines with increasing deformation rate.

3.5 Conclusions

A modification to the dumbbell model has been described based on the non-affine deformation of polymer solutions, by replacing the upper convected time derivative in the dumbbell model by the Johnson-Segalman derivative. The new model, FENE-CD-JS, is a refined version of the original FENE-CD model, and with this modification it now predicts a shear-thinning shear viscosity and a non-vanishing second normal stress difference. It represents a generalised form of the Chilcott and Rallison chain with a non-linear hydrodynamic drag coefficient and other variants can be obtained based on the choice of model parameters. The stabilising effect of shear-thinning introduced by the J-S derivative will yield more stable numerical simulations compared with the FENE-CD model and hence a wider range of Wi can be achieved by this approach.

Part II

Implementation and Validation of Computational Technique

Chapter 4

Computational Technique

4.1 Introduction

The field operation and manipulation (OpenFOAM) is an open source library [5], which provides a set of tools and solvers in a modular and extensible fashion for a wide range of flow applications including aerodynamics and internal combustion engines. Solvers are either based on the Eulerian simulation technique or the Lagrangian particle tracking method, which can be built upon and manipulated using top-level syntax. The implementation of an iterative solution algorithm for viscoelastic flow problems within the OpenFOAM framework will be discussed in this chapter. The finite volume scheme is stabilized by the Discrete Elastic Viscous Split Stress (DEVSS) formulation [104] used for convection-dominated transport of viscoelastic fluids. The discretised systems of algebraic equations are solved by an iterative scheme based on a predictor-corrector strategy for transient flow calculations. A time-marching scheme is adopted from the onset because it closely follows the trajectory of the physical solutions and enhances numerical stability. Such a transient approach is more appropriate for viscoelastic fluids since they have memory and are better treated as unsteady initial value problems. Moreover, this approach is useful because some industrial viscoelastic applications are unsteady in nature with no real steady-state equilibrium solution.

In Section 4.1.1, an overview of the numerical technique is presented. The discretisation of the various terms of the governing equations are provided in Section 4.2. Higher resolution differencing schemes for the treatment of the convection term in the mo-

mentum and constitutive equations are discussed in Section 4.3. In Section 4.4, the EVSS/DEVSS stabilisation scheme is presented. Section 4.5 discusses the iterative solution technique. Section 4.6 describes the finite element discretisation method employed in the POLYFLOW solver [31].

4.1.1 Discretisation of the Transport Equation

OpenFOAM uses the finite volume method to convert a set of partial differential equations to ordinary differential equations, which can be approximated using various finite-difference schemes. Consider an intensive property, $\boldsymbol{\psi}$. A generic transport equations for this property may be written as,

$$\frac{\partial \rho \boldsymbol{\psi}}{\partial t} + \nabla \cdot (\rho \boldsymbol{v} \boldsymbol{\psi}) = \nabla \cdot \Gamma \nabla \boldsymbol{\psi} + S(\boldsymbol{\psi}) \tag{4.1}$$

in which $\boldsymbol{\psi} = 1$ and $S(\psi) = 0$ for mass conservation, and $\boldsymbol{\psi} = \boldsymbol{v}$ for momentum conservation. $\boldsymbol{v}$ is the fluid velocity, ρ is the fluid density and Γ is the diffusivity. The terms in the transport equation may be identified as follows: $\partial \rho \boldsymbol{\psi} / \partial t$ is the temporal term, $\boldsymbol{v} \cdot \nabla \rho \boldsymbol{\psi}$ is the convection term, $\nabla \cdot \Gamma \nabla \boldsymbol{\psi}$ is the diffusion term, and $S(\boldsymbol{\psi})$ is the source term. The non-linearity embodied in such transport equations is the source of hydrodynamic instability in physically complex flows such as the Rayleigh-Taylor and Kelvin-Helmholtz instabilities in free surface flow [105]. Due to this non-linearity, appropriate solution techniques are necessary to solve the transport equation. In the finite volume solution strategy outlined in this chapter, the resulting algebraic equations is linearised by Rhie-Chow interpolation scheme, which fixes the flux of the velocity across the cell faces. An iterative solution technique is applied by updating the fluxes after each iteration until convergence is reached. The system of coupled non-linear equations is solved sequentially for each field variable in a segregated approach, which imitates the staggered grid arrangement to remove velocity-stress-pressure decoupling [106].

4.2 Finite Volume Formulation for Spatial Discretisation

Finite volume methods are attractive for viscoelastic flow problems due to the reduced computational cost and greater numerical stability they offer compared with finite element methods. In the collocated grid arrangement, all dependent variables are stored in the centre of control volume, P. The finite volume discretisation of each term in the

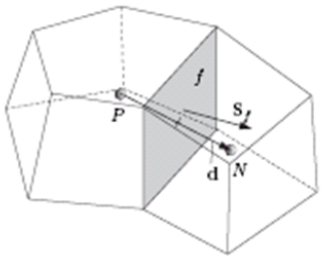

Figure 4.1: Computational cell for finite volume method from [5]

transport equations is formulated by first integrating the term over a control volume, V, which ensures the conservation of the physical quantities. Gauss's theorem is applied to convert the volume integrals to surface integrals over the cell surface, S, bounding the volume. The resulting expressions are discretised using appropriate differencing schemes. In the present implementation, with the exception of the convection terms, the central differencing scheme (CDS) is used for the rest of the terms in the transport equations. The convection term requires special interpolation techniques in order to ensure numerical accuracy and stability, which will be described in Section 4.3. The discretisation of the momentum and constitutive equations in the present implementation is described below.

The momentum and continuity equations are discretised on a term-by-term basis using the finite volume method and by applying Gauss's theorem. The various terms in the constitutive equation are discretised in a similar manner as described for the momentum equation. It is only required that the velocity component is replaced by the elastic stress tensor to obtain the equivalent expressions for the stress. After discretisation, the resulting linearised expressions relate the cell centre values of the unknown variables to their values at the neighbouring cells, which can be solved by one of a range of iterative matrix solvers

including the conjugate and biconjugate gradient methods available in OpenFOAM. The conjugate gradient method is suited for solving symmetric coefficient matrices such as those arising from the pressure-correction equation, and the biconjugate gradient method solves non-symmetric matrices such as those resulting from the discretised momentum equation and the constitutive equation for the velocity and stress fields, respectively.

Diffusion Term

The diffusion or Laplacian term is discretised as follows

$$\int_V \nabla \cdot (\nu \nabla \boldsymbol{v}) dV = \int_S (\nu \nabla \boldsymbol{v})_f \cdot \hat{\boldsymbol{n}} dS = \sum_i \nu_i \nabla \boldsymbol{v}_{f,i} \cdot \boldsymbol{S}_i \tag{4.2}$$

where $\boldsymbol{v}$ is the velocity field, ν is the kinematic viscosity, $\boldsymbol{S}$ is the surface area vector and the subscript f indicates that the term should be evaluated on the cell faces, and i denotes the cell. In one-dimension the face gradient term $(\nabla \boldsymbol{v})_f \cdot \boldsymbol{S}$ can be evaluated between the centre of the cell of interest P and centre of a neighbouring cell N using

$$(\nabla \boldsymbol{v})_f \cdot \boldsymbol{S} \approx \frac{v_N - v_P}{|\boldsymbol{d}|} |\boldsymbol{S}| \tag{4.3}$$

in which $\boldsymbol{d}$ is the length vector between the cell centres P and N.

Convection Term

The discretisation of the convection term may be written as

$$\int_V \nabla \cdot (\rho \boldsymbol{v} \boldsymbol{U}) dV = \int_S (\rho \boldsymbol{v} \boldsymbol{U})_f \cdot \hat{\boldsymbol{n}} dS = \sum_i \rho_i \boldsymbol{v}_{f,i} \boldsymbol{U}_{f,i} \cdot \boldsymbol{S}_i = \sum_i F \boldsymbol{v}_{f,i} \tag{4.4}$$

in which $F = \rho\phi$ where ρ is the fluid density, and $\phi = \boldsymbol{U}_f \cdot \boldsymbol{S}$ is the velocity flux across the face f defined as the scalar product of the cell face velocity and the cell face normal. If the velocity field, $\boldsymbol{v}_f$, is interpolated using central differencing in OpenFOAM, which is second-order accurate but unbounded, it is given by the expression

$$\boldsymbol{v}_f = f_x v_P + (1 - f_x) v_N \tag{4.5}$$

in which $f_x \equiv |fN|/|PN|$. $|fN|$ is the distance between f and cell centre N, and $|PN|$ is the distance between cell centres P and N. Since this differencing scheme is not suitable

for discretising hyperbolic transport equations, the convection term is often discretised using the first-order accurate upwind differencing scheme (UDS),

$$\boldsymbol{v}_f = \begin{cases} v_P & \text{if } F > 0 \\ v_N & \text{if } F < 0 \end{cases} \tag{4.6}$$

The upwind differencing scheme satisfies the boundedness criterion because it leads to a diagonally dominant system of algebraic equations, which makes it is highly stable. However, the UDS scheme is only first-order accurate and achieves stability at the expense of accuracy. More appropriate higher order schemes will be described later.

Gradient Term

The pressure gradient term is discretised as follows

$$\int_V \nabla p dV = \int_S p_f dS = \sum_i p_{f,i} \boldsymbol{S}_i \tag{4.7}$$

where the face pressure field p_f can be evaluated by central differencing as described in Eq. 4.5.

Divergent Term

In the present implementation, the stress gradient term in the momentum equation is treated as a source term and it is discretised as follows

$$\int_V \nabla \cdot \boldsymbol{\sigma} dV = \int_S \boldsymbol{\sigma}_f \cdot \hat{\boldsymbol{n}} dS = \sum_i \boldsymbol{\sigma}_{f,i} \cdot \boldsymbol{S}_i \tag{4.8}$$

in which $\boldsymbol{\sigma}_f \cdot \boldsymbol{S}$ is the stress flux across the face f. The cell-face stress, $\boldsymbol{\sigma}_f$, is evaluated by central differencing as described in Eq. 4.5.

Temporal Term

The temporal term is integrated over a control volume and evaluated using a suitable time marching scheme. Explicit discretisation schemes such as the explicit Euler are not suitable for hyperbolic transport problems as they may cause spatial oscillations whenever a high-order scheme is used for the spatial discretisation. The first-order accurate implicit

Euler scheme gives a well-behaved numerical solution,

$$\frac{d}{dt}\int_V \boldsymbol{v} dV \approx \frac{(v_P V)^{n+1} - (v_P V)^n}{\triangle t} \tag{4.9}$$

The exponent n represent values that are stored from the previous time step, t, and $n+1$ are values that are computed at the present time step, $t+\triangle t$. The drawback of such first-order temporal schemes is that they introduce numerical diffusion in the solution. This could lead to attenuation in the amplitude of travelling waves arising, for instance, from a transient convection process. Using second-order accurate schemes such as the backward differencing scheme yields a better numerical accuracy. The backward differencing scheme is given by

$$\frac{d}{dt}\int_V \boldsymbol{v} dV \approx \frac{3(v_P V)^{n+1} - 4(v_P V)^n + (v_P V)^{n-1}}{2\triangle t} \tag{4.10}$$

In this expression, the exponent $n-1$ depicts values that are stored from the previous time step, $t - \triangle t$.

4.3 Differencing Schemes for the Convection Term

Although the upwind differencing scheme is highly stable, it is only first-order accurate. It is highly diffusive and can cause severe numerical diffusion particularly when the flow direction is skewed relative to the grid lines. For better numerical accuracy high-order upwind differencing schemes such as LUDS (Linear Upwinding Differencing scheme) or QUICK (Quadratic Upwind Interpolation for Convection Kinematics) are often used for the convective fluxes. However, these schemes are only conditionally stable and may suffer from unboundedness and unphysical oscillations, which causes convergence difficulties at moderate levels of Weissenberg number. The stability and accuracy issues may be remedied by using a composite high-order scheme with a boundedness criterion in the so-called high-resolution schemes. This is achieved by the Normalised Variable Approach (NVA) [107] and the Convection Boundedness Criterion (CBC) [108] described below.

Using Fig. 4.2, for the variation of a convected variable ϕ across the face f the normalised variable is defined as,

$$\widetilde{\phi} = \frac{\phi - \phi_U}{\phi_D - \phi_U} \tag{4.11}$$

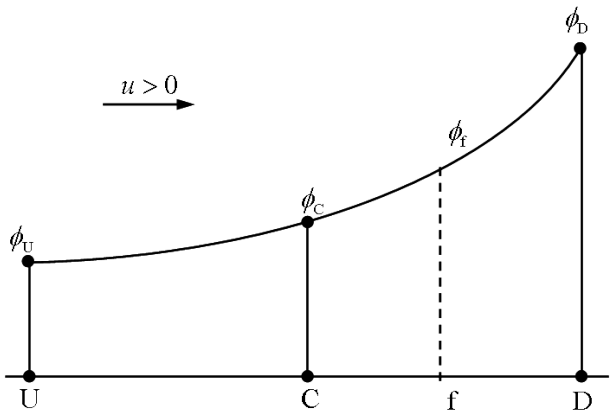

Figure 4.2: Nodal variation of ϕ in the vicinity of f on a uniform grid

where the subscripts U and D are, relatively to cell C, the upstream and downstream cells. Any differencing scheme can be written in the form,

$$\widetilde{\phi}_f = f(\widetilde{\phi}_C) \tag{4.12}$$

Following Eq. 4.11 we can define the normalised variables, $\widetilde{\phi}_C$ and $\widetilde{\phi}_f$, as follows,

$$\widetilde{\phi}_C = \frac{\phi_C - \phi_U}{\phi_D - \phi_U} \tag{4.13}$$

and

$$\widetilde{\phi}_f = \frac{\phi_f - \phi_U}{\phi_D - \phi_U} \tag{4.14}$$

The Convective Boundedness Criterion is imposed in order to avoid unphysical oscillations in the solution. The criterion requires that ϕ_C is bounded between ϕ_U and ϕ_D, i.e. $\phi_U \leq \phi_C \leq \phi_D$ (or $\phi_U \geq \phi_C \geq \phi_D$). In terms of normalised variables, the Convective Boundedness Criterion is equivalently written as $0 \leq \widetilde{\phi}_C \leq 1$, since $\widetilde{\phi}_C = 0 \Rightarrow \phi_C = \phi_U$ and $\widetilde{\phi}_C = 1 \Rightarrow \phi_C = \phi_D$. The Convective Boundedness Criterion can be presented in a Normalised Variable Diagram (NVD) [108] shown in Fig. 4.3 for various differencing schemes. From the diagram, it can shown that for a uniform grid the various schemes can be written in terms of the normalised variables as follows

$$\text{UDS} \qquad \widetilde{\phi}_f = \widetilde{\phi}_C \tag{4.15}$$

$$\text{CDS} \qquad \widetilde{\phi}_f = \frac{1}{2} + \frac{1}{2}\widetilde{\phi}_C \tag{4.16}$$

$$\text{DDS} \qquad \widetilde{\phi}_f = \widetilde{\phi}_D \tag{4.17}$$

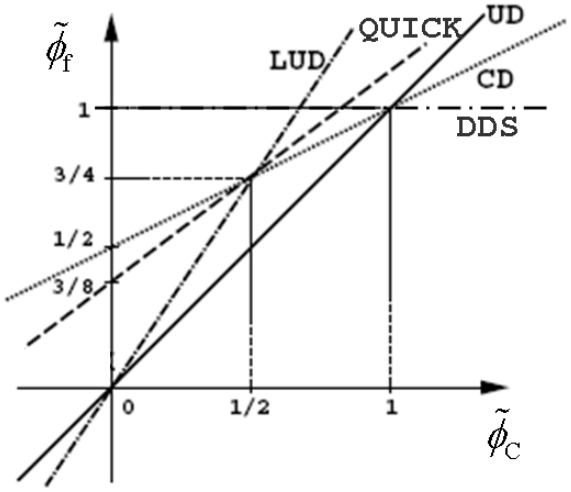

Figure 4.3: Normalised Variable Diagram

$$\text{LUDS} \qquad \widetilde{\phi}_f = \frac{3}{2}\widetilde{\phi}_C \tag{4.18}$$

$$\text{QUICK} \qquad \widetilde{\phi}_f = \frac{3}{8} + \frac{3}{4}\widetilde{\phi}_C \tag{4.19}$$

High-resolution schemes can been formulated from the NVD diagram. The MINMOD scheme of Harten [109], the SMART scheme of Gaskell and Lau [108], and the CUBISTA (convergent and universally bounded interpolation scheme for the treatment of advection) scheme of Alves et al. [43] are expressed as follows,

$$\text{MINMOD:} \qquad \widetilde{\phi}_f = \begin{cases} \frac{3}{2}\widetilde{\phi}_C & 0 < \phi_C < \frac{1}{2} \quad \text{LUDS} \\ \frac{1}{2} + \frac{1}{2}\widetilde{\phi}_C & \frac{1}{2} < \phi_C < 1 \quad \text{CDS} \\ \widetilde{\phi}_C & \text{elsewhere} \quad \text{UDS} \end{cases} \tag{4.20}$$

$$\text{SMART:} \qquad \widetilde{\phi}_f = \begin{cases} 3\widetilde{\phi}_C & 0 < \phi_C < \frac{1}{6} \\ \frac{3}{8} + \frac{3}{4}\widetilde{\phi}_C & \frac{1}{6} < \phi_C < \frac{5}{6} \quad \text{QUICK} \\ 1 & \frac{5}{6} < \phi_C < 1 \quad \text{DDS} \\ \widetilde{\phi}_C & \text{elsewhere} \quad \text{UDS} \end{cases} \tag{4.21}$$

$$\text{CUBISTA:} \qquad \widetilde{\phi}_f = \begin{cases} \frac{7}{4}\widetilde{\phi}_C & 0 < \phi_C < \frac{3}{8} \\ \frac{3}{8} + \frac{3}{4}\widetilde{\phi}_C & \frac{3}{8} \leq \phi_C \leq \frac{3}{4} \quad \text{QUICK} \\ \frac{3}{4} + \frac{1}{4}\widetilde{\phi}_C & \frac{3}{4} < \phi_C < 1 \\ \widetilde{\phi}_C & \text{elsewhere} \quad \text{UDS} \end{cases} \tag{4.22}$$

The MINMOD scheme combines the second-order accuracy of LUDS with the stability of UDS whereas the SMART scheme is at most third-order accurate owing to the QUICK scheme. The CUBISTA was proposed by Alves et al. [43] by combining the CBC with the total variable diminishing (TVD) constraint required for explicit transient calculations to achieve better iterative convergence properties. In the present work, the MINMOD scheme will be used. The accuracy, boundedness, and stability of this scheme for solving hyperbolic PDEs in convection-dominated problems have been demonstrated both in viscoelastic steady-state flows [110] and turbulent flows [111, 112].

4.4 Stabilization Technique

Further numerical stability of the hyperbolic transport problem may be accomplished by one of the various stabilisation techniques adapted for convection-dominated convection/diffusion problems. The most robust of these methods, that exploits the elliptic behaviour of the momentum equation in various ways, is the Elastic-Viscous Split Stress (EVSS) method [113]. In the EVSS method introduced by Mendelson *et al.* [114] the extra-stress tensor in the momentum equation is separated into elastic and viscous components, and a purely viscous term is added to the elastic stress $\boldsymbol{\tau}_p$. For the Oldroyd-B fluid the EVSS scheme can be written as follows

$$\boldsymbol{\Sigma}_p = \boldsymbol{\tau}_p - 2\eta_p \boldsymbol{D} \tag{4.23}$$

$$\rho\left(\frac{\partial \boldsymbol{v}}{\partial t} + (\boldsymbol{v}\cdot\nabla)\boldsymbol{v}\right) = -\nabla p + \nabla\cdot\boldsymbol{\Sigma}_p + \eta_s\nabla^2\boldsymbol{v} \tag{4.24}$$

$$\boldsymbol{\Sigma}_p + \lambda\overset{\triangledown}{\boldsymbol{\Sigma}}_p = 2\lambda\eta_p\overset{\triangledown}{\boldsymbol{D}} \tag{4.25}$$

where $\boldsymbol{\Sigma}_p$ replaces the elastic stress tensor in the new formulation, $\boldsymbol{D} = \frac{1}{2}(\nabla\boldsymbol{v} + (\nabla\boldsymbol{v})^T)$ is the rate of deformation tensor, and η_s and η_p are the solvent and polymer viscosities. Eqs. 4.24 and 4.25 are the momentum and constitutive equations, respectively. The addition of the purely viscous term has a stabilizing effect on the solution by introducing an elliptic operator into the momentum equation, thus, effectively increasing the elliptic character of the governing equations. However, the application of EVSS is somewhat limited to relatively simple constitutive equations of the Oldroyd-type due to the requirement for

an explicit change of variable, which was the motivation for the introduction of the discrete EVSS (DEVSS) method by Guénette and Fortin [115]. This method requires no explicit change of variable and no derivative of the rate of deformation tensor to be calculated. This makes the DEVSS method more attractive for more complicated constitutive equations such as the integral constitutive equations.

The present implementation of the DEVSS technique is much more straightforward and it involves the addition of an elliptic contribution to the momentum equation, which is solved implicitly, and then explicitly subtracting its counterpart in a source term. For the Oldroyd-B fluid the method may be written as follows,

$$\boldsymbol{\tau}_p + \lambda \overset{\nabla}{\boldsymbol{\tau}}_p = 2\eta_p \boldsymbol{D} \tag{4.26}$$

$$\rho \left(\frac{\partial \boldsymbol{v}}{\partial t} + (\boldsymbol{v} \cdot \nabla)\boldsymbol{v} \right) = -\nabla p + \eta_n \nabla^2 \boldsymbol{v} + \nabla \cdot \boldsymbol{\Sigma}_p \tag{4.27}$$

where the numerical viscosity factor η_n is often taken equal to the zero shear rate viscosity. In Eq.4.27, the term $\nabla \cdot \boldsymbol{\Sigma}_p$ is given by $\nabla \cdot \boldsymbol{\tau}_p - \alpha \nabla^2 \boldsymbol{v}$ where α is the added artificial viscosity. This term is treated as a source term and hence it does not contribute to the coefficient matrix (to which the term $\alpha \nabla^2 \boldsymbol{v}$ has been added to improve numerical stability) resulting from the discretisation of the momentum equation. Noting that Eq.4.27 bears close resemblance to Eq. 4.25 in the EVSS method discussed earlier it can be seen that both techniques are equivalent except for the explicit reformation of the constitutive equation that is required in the EVSS method.

4.5 Iterative Solution Algorithm

The solution strategy involves a modification to the PISO (Pressure-Implicit with Splitting of Operators) algorithm [116] by explicitly introducing elastic stress unknowns in the momentum equation, which requires some additional steps. The elastic stresses are introduced by the constitutive equation, the specific choice of which depends on the fluid. In order to apply Rhie-Chow interpolation, the momentum equation is expressed as follows

$$\frac{\partial \boldsymbol{v}}{\partial t} + (\boldsymbol{v} \cdot \nabla)\boldsymbol{v} - \nabla \cdot (\nu \nabla \boldsymbol{v}) - \frac{1}{\rho} \nabla \cdot \boldsymbol{\Sigma}_p = -\frac{1}{\rho} \nabla p \tag{4.28}$$

where $\nu = \eta_n / \rho$, and the stress divergence term has been included in the momentum equation to provide the needed coupling with the constitutive equation. After discretisation

this equation may be written as,

$$A\boldsymbol{v}^{m^*} = \mathcal{H}^n - \nabla[\hat{p}]^n \tag{4.29}$$

in which the term $\mathcal{H}^n$ contains the convective and viscous terms as well as the elastic contribution from the stress components as a source term, and A is the matrix of coefficients. The $(\hat{\cdot})$ indicates a division by ρ, and $[\cdot]$ denotes numerical approximation of the corresponding variable. n and m represent the past and present times, respectively, and the asterisks (*) denotes the predicted value of the variable in the outer iteration [117]. Dividing Eq. 4.29 through by A yields

$$\boldsymbol{v}^{m^*} = \boldsymbol{U}^{m^*} - A^{-1}\nabla[\hat{p}]^n \tag{4.30}$$

where $\boldsymbol{U} = A^{-1}\mathcal{H}$. In the first step of the iterative procedure the discretised constitutive equation is solved to provide estimates for the stress field, $\boldsymbol{\tau}_p^m$, for a given initial velocity field. Using the computed stress field the velocity field is estimated from Eq. 4.30, initially without the contribution of the pressure gradient term on the right hand side. The predicted velocity field $\boldsymbol{v}^{m^*}$ is not divergence-free as it does not satisfy the continuity equation. To proceed, the velocity field is corrected by taking the divergence of Eq. 4.30 and enforcing continuity ($\nabla\cdot\boldsymbol{v} = 0$) to yield a Poisson equation for the pressure-correction step,

$$\nabla\cdot\boldsymbol{U}^{m*} = \nabla\cdot(A^{-1}\nabla[\hat{p}]^m) \tag{4.31}$$

After solving this equation for p^m the divergence-free corrected velocity, $\boldsymbol{v}^m$, is computed from Eq. 4.30, and the stress field can now be corrected by solving the constitutive equations again using the divergence-free velocity. The predictor-corrector procedure is repeated until all equations are satisfied. This completes the solution algorithm. The iteration process consists of a six-step procedure summarised as follows:

1. For a given velocity field velocity field, $\boldsymbol{v}_i^n$, solve the constitutive equation implicitly for the elastic stress components, $\tau_{p,i}^m$ and compute $\boldsymbol{\Sigma}_{p,i}^m$.

2. Using the stress field, $\boldsymbol{\Sigma}_{p,i}^m$, solve the discretised momentum equation without the contribution of the pressure gradient term to obtain the velocity components v_i^{m*}. This represents the predictor step for velocity.

3. Using the predicted velocity $\boldsymbol{U}_i^{m*}$, solve the pressure-correction equation (4.31) for the pressure field, p^m, which is the predictor step for the pressure.

4. Correct (first corrector step for velocity) the velocity field $\boldsymbol{v}_i^m$, by solving for the velocity field (Eq. 4.30) using the estimated pressure field, p^m.

5. Using the corrected velocities, $\boldsymbol{v}_i^m$, solve the discretised constitutive equation again to obtain the corrected stress field.

6. Return to step 1 and repeat the steps 1-5 using $\boldsymbol{v}_i^m$, p^m, and $\boldsymbol{\tau}_p^m$ as improved estimates for the solutions at the new time step values $\boldsymbol{v}_i^{n+1}$, p^{n+1}, and $\boldsymbol{\tau}_{p,i}^{n+1}$, until all corrections are negligibly small.

7. March to the next time step.

Thus the numerical scheme is implemented as time-dependent from the onset, which has a favourable impact on the stability of the numerical scheme. The linearised system of algebraic equations is described in the next section.

4.5.1 The Linear Algebraic System of Equations

The linearised system of equations resulting from the discretisation of the transport equations may be generally written as

$$A_P\phi_P + \sum_N A_l\phi_l^n = Q_P \tag{4.32}$$

where P denotes the cell centre node and l denotes the node of the neighbouring cells involved in the finite difference approximations. In matrix form, the summation and indices can be dropped and the system of linear algebraic equations may be written as follows

$$A\boldsymbol{\phi} = \boldsymbol{Q} \tag{4.33}$$

where $\boldsymbol{\phi}$ is the column vector of the dependent variable, $\boldsymbol{Q}$ is the source vector, and A is a sparse block matrix with diagonally-dominant elements, which can readily be inverted by any of the iterative decomposition techniques to solve the equation. The iterative solvers exploit the sparse structure of this matrix, and thus significantly reducing the requirement

for CPU memory. Depending on the discretisation scheme in Eq. 4.33, the equation may be written explicitly in terms of the nodes as follows

$$A_W\phi_W + A_S\phi_S + A_P\phi_P + A_N\phi_N + A_E\phi_E = Q_P \tag{4.34}$$

in which W, S, N, E represent the compass notations: west, south, north, east, respectively.

$$\begin{bmatrix} * & * & * & \cdot & * & \cdot & \cdot & \cdot & \cdot & \cdot & \cdot \\ \cdot & * & * & * & \cdot & * & \cdot & \cdot & \cdot & \cdot & \cdot \\ * & \cdot & * & * & * & \cdot & * & \cdot & \cdot & \cdot & \cdot \\ \cdot & * & \cdot & * & * & * & \cdot & * & \cdot & \cdot & \cdot \\ & & A_W & & A_S & A_P & A_N & & A_E & & \\ \cdot & \cdot & \cdot & * & \cdot & * & * & * & \cdot & * & \cdot \\ \cdot & \cdot & \cdot & \cdot & * & \cdot & * & * & * & \cdot & * \\ \cdot & \cdot & \cdot & \cdot & \cdot & * & \cdot & * & * & * & \cdot \\ \cdot & \cdot & \cdot & \cdot & \cdot & \cdot & * & \cdot & * & * & * \end{bmatrix} \times \begin{bmatrix} \cdot \\ \phi_W \\ \cdot \\ \phi_S \\ \phi_P \\ \phi_N \\ \cdot \\ \phi_E \\ \cdot \end{bmatrix} = \begin{bmatrix} \cdot \\ \cdot \\ \cdot \\ \cdot \\ Q_P \\ \cdot \\ \cdot \\ \cdot \\ \cdot \end{bmatrix} \tag{4.35}$$

This sparse structure of the matrix makes the use of iterative solvers very attractive because the diagonal dominance guarantees solution convergence. Increased solution convergence rate can be achieved through matrix preconditioning, and the rate of the convergence depends on the dispersion of the eigenvalues of the matrix. The conjugate gradient matrix solver can be used with the incomplete Cholesky decomposition as the preconditioner for solving the linearised system of equations if the resulting matrix is symmetric, otherwise a biconjugate gradient method is used.

4.6 Finite Element Method

The finite element method is based on an equivalent weak formulation of the transport equations. The weak formulation allows the continuity restrictions on the approximation subspaces to be relaxed using some trial function space V. The problem statement is to

find the solution $u \in V$ of the equation $F(u) \equiv Au - f$ such that

$$F(u) \leq F(v), \qquad \forall v \in V, \tag{4.36}$$

where $F : V \rightarrow \mathbb{R}$ and v is a basis function. The equivalent weak formulation of the problem can be written as: Find $u \in V$ such that,

$$a(u, v) = f(v) \qquad \forall v \in W, \tag{4.37}$$

where W is the test space. The basis function for W may be chosen from the trial space V, i.e. $W \subset V$. By choosing an appropriate approximation space $V^h \subset V$, Eq. (4.37) becomes

$$a(u^h, v^h) = f(v^h) \qquad \forall v^h \in V^h \tag{4.38}$$

Finite element discretisations may be created using the Galerkin method. This method is well-suited for solving elliptic problems but not for the equations governing the flow of viscoelastic fluids because of their mixed elliptic-hyperbolic character. Using this method for discretising the convection term of the constitutive equation often leads to spurious oscillations. Hence, more appropriate techniques such as the streamline upwind (SU) and the streamline-upwind Petrov-Galerkin (SUPG) [118] methods are required. These techniques are based on the modification of the test function in the constitutive equation by adding anisotropic diffusion along the streamlines, which increases the elliptic character of the governing equations, thus improving the stability of the problem.

In POLYFLOW, further stability of the numerical scheme may also be achieved by using the EVSS/DEVSS scheme described previously. The implementation of the discretisation using a combination of DEVSS and streamline upwinding (SU) method for the equations governing the flow of an exponential Phan-Thien-Tanner fluid is described as follows. Let Ω denote the flow domain and T_p, V, P, and Λ the solution spaces of the elastic stress tensor, velocity field, pressure, and the rate of deformation tensor, with their corresponding approximating subspaces T_p^h, V^h, P^h, and Λ^h, respectively, the finite element discretisation of the governing equations is represented by stating the problem as follows. Find $\boldsymbol{v} \in V^h$, $p \in P^h$, $\boldsymbol{\tau}_p \in T^h$, $\dot{\boldsymbol{\gamma}} \in \Lambda^h$, such that

$$\int_{\Omega^h} \psi^{\boldsymbol{\tau}_p} \left\{ \boldsymbol{\tau}_{p,i} + \lambda_i \overset{\triangledown}{\boldsymbol{\tau}}_{p,i} + \exp\left[\frac{\epsilon\lambda_i}{\eta_{p,i}} tr(\boldsymbol{\tau}_{p,i}) - 1\right] + \xi_i\lambda_i \left(\overset{\triangle}{\boldsymbol{\tau}}_{p,i} - \overset{\triangledown}{\boldsymbol{\tau}}_{p,i} \right) - \eta_{p,i}(\nabla\boldsymbol{v} + \nabla\boldsymbol{v}^T) \right\} d\Omega^h + \int_{\Omega^h} (k\boldsymbol{v}\cdot\nabla\psi^{\boldsymbol{\tau}_p})(\boldsymbol{v}\cdot\nabla\boldsymbol{\tau}_{p,i}) d\Omega^h = 0, \quad \forall\psi^{\tau_p} \in T_p^h \tag{4.39}$$

$$\int_{\Omega^h} \left\{ \nabla\psi^{\boldsymbol{v}} \cdot \left(-p\boldsymbol{I} + \sum_i \tau_{p,i} + \eta_n(\nabla\boldsymbol{v} + \nabla\boldsymbol{v}^T) - \eta_n\dot{\boldsymbol{\gamma}} \right) - \rho\frac{D\boldsymbol{v}}{Dt} \right\} d\Omega^h = 0, \quad \forall\psi^{\boldsymbol{v}} \in V^h \tag{4.40}$$

$$\int_{\Omega^h} \psi^p(\nabla\cdot\boldsymbol{v}) d\Omega^h = 0, \quad \forall\psi^p \in P^h \tag{4.41}$$

$$\int_{\Omega^h} \psi^{\dot{\boldsymbol{\gamma}}}((\boldsymbol{\nabla}v + \nabla\boldsymbol{v}^T) - \dot{\boldsymbol{\gamma}}) d\Omega^h = 0, \quad \forall\psi^{\dot{\boldsymbol{\gamma}}} \in \Lambda^h \tag{4.42}$$

where η_n is a numerical viscosity parameter usually taken equal to the zero-shear-rate viscosity, and the coefficient k is a parameter associated with directional Péclet numbers [119]. The linear or quadratic shape functions may be used for interpolating the set of variables $\boldsymbol{v}$, p, $\boldsymbol{\tau}_p$, and the unknown rate of deformation tensor, $\dot{\boldsymbol{\gamma}}$. The resulting system of non-linear algebraic equations is solved by the Newton's method using either a direct solver or a hybrid direct/iterative solver.

4.7 Conclusions

A numerical technique has been implemented within the openFOAM library, which uses the collocated finite volume method to discretise the transport equations. The treatment of the convection term of the governing equation using a high resolution scheme based on the Normalised Variable Approach (NVA) and the Convection Boundedness Criterion (CBC), which provide better numerical stability and accuracy for hyperbolic PDE problems has been described. Further stability can be achieved through stress-splitting techniques such as the EVSS/DEVSS method, which enhances the elliptic character of the governing equations. The iterative solution strategy is based on the PISO predictor-corrector algorithm and Rhie-Chow interpolation scheme, which has been modified in the

present work for viscoelastic flow calculations. The finite element discretisation scheme employed in the POLYFLOW solver has also been described.

Chapter 5

Evaluation of Numerical Technique in Benchmark Flow

5.1 Introduction

The 4:1 contraction geometry is one of the most studied benchmark problems for viscoelastic flows [6, 46, 110, 120, 121]. In the literature, particular attention has been paid to the prediction of viscoelastic phenomena, accuracy, and stability of numerical codes using this geometry. Numerical stability is tested through progressive mesh refinement and convergence of the numerical results. Due to the high stress gradients arising at the re-entrant corners, a well-refined mesh is required in this region to ensure the numerical solution is accurate. Unfortunately, most calculations in the 4:1 contraction have used relatively small computational meshes. Probably, the only exception to this is the simulation of Alves et al. [6]. The paper was motivated by the need to provide accurate quantitative data for the 4:1 contraction benchmark flow using a finite volume method and their CUBISTA differencing scheme.

In this chapter, the present numerical technique will be evaluated by detailed comparison with the results of Alves et al. using the Oldroyd-B model and the linear Phan-Thien-Tanner model. The Oldroyd-B model is well-known for its convergence difficulties which causes early breakdown of numerical algorithms. The meshes used in the present simulations are of similar order of refinement as those reported by Alves et al. [6].

5.2 Geometry and Computational Meshes

A schematic diagram of the computational geometry is provided in Fig. 5.1 showing one-half of the full 2-D geometry with a symmetry axis along the centreline, $y = 0$, and other relevant features. The contraction ratio is given by the ratio of the width of the upstream channel to that of the downstream channel, w_u/w_c. The parameter χ_L is the length of the corner vortex measured downstream from the re-entrant corner nomalised by the characteristic length, w_c, of the channel. In order to allow for complete flow development along the channels, the length of the upstream channel is made equal to $80w_c$ while that of the downstream is $100w_c$.

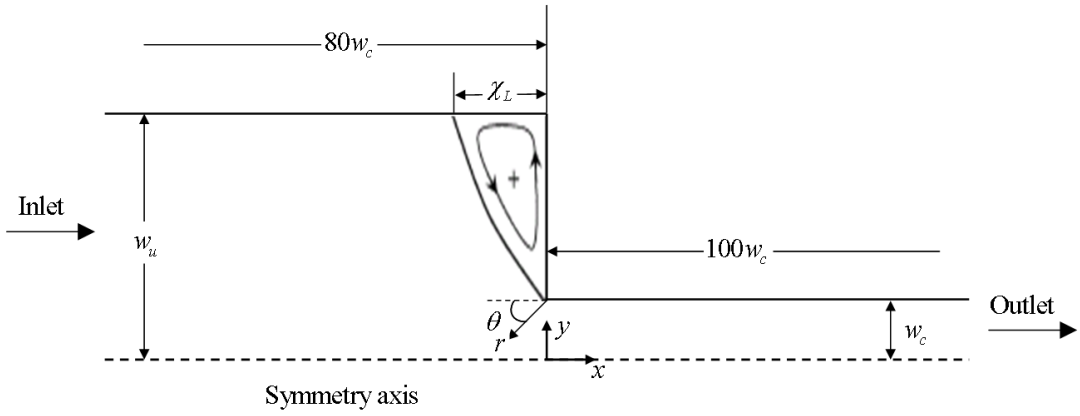

Figure 5.1: A schematic diagram of a 4:1 planar contraction geometry

Four progressively refined orthogonal meshes, shown in Fig. 5.2, have been designed for the present study. The meshes are graded along the channel and well-refined in the vicinity of the re-entrant corner in order to resolve the high stress gradients that occur in the region. Finer details of the refinement around the re-entrant corner are revealed by the zoomed view shown in the figure. The characteristics of the meshes are provided in Table 5.1.

In the simulations, the creeping flow condition ($Re = 0$) will be assumed by setting the inertial term in the momentum equation to zero in order to facilitate comparison with the literature results. The ratio of the solvent viscosity to the total viscosity is set to the commonly used value of $\eta_s/\eta = 1/9$. The Weissenberg number, Wi, is defined in terms of the fluid properties and the parameters of the downstream channel as follows, $Wi =$

Mesh	NC	$\triangle x_{min}/w_c$
M1	7200	0.02
M2	14230	0.014
M3	27800	0.01
M4	55475	0.007

Table 5.1: Mesh information. NC: number of cells; $\triangle x_{min} = \triangle y_{min}$: cell spacing

$\lambda U/w_c$, where U is the mean velocity in the downstream channel, and λ the relaxation time of the fluid. The Couette correction coefficient is given by $C = \triangle p_{ext}/2\tau_w$, in which $\triangle p_{ext}$ is the excess pressure drop, which is given by $\triangle p_{ext} = \triangle p - \triangle p_{FD}$, where $\triangle p$ is the total pressure drop, and $\triangle p_{FD} = \triangle p_{upstream} + \triangle p_{downstream}$ is the sum of the pressure drop calculated for fully developed flow in the upstream and downstream channels. The total pressure drop, $\triangle p$, is measured between the inlet of the upstream channel and the exit of the downstream channel. For the finite volume calculations, the boundary conditions are described as follows. At the inlet boundary a Dirichlet condition is applied for the velocities, the stress is set to zero, and a homogeneous Neumann condition is applied for the pressure field. A homogeneous Neumann condition is prescribed for the velocity and stress fields at the outlet boundary, while a vanishing pressure is prescribed at the outlet boundary. A no-slip condition is prescribed along the walls and a symmetry conditions is specified along the symmetry axis.

5.3 The Oldroyd-B Fluid

To illustrate the influence of the differencing scheme on numerical accuracy the results of the first-order accurate UDS scheme is compared with the MINMOD scheme in Fig. 5.3. The simulations show marked qualitative differences in the results obtained using the different schemes. In the flow patterns obtained by the MINMOD scheme, the corner and lip vortices are small and distinct, whereas the UDS results are less accurate and very diffusive leading to the prediction of larger vortices even in the well-refined mesh, M4. However, the accuracy of the numerical scheme is significantly enhanced particularly in mesh M4, in which the lip and corner vortices are almost distinct. The flow patterns

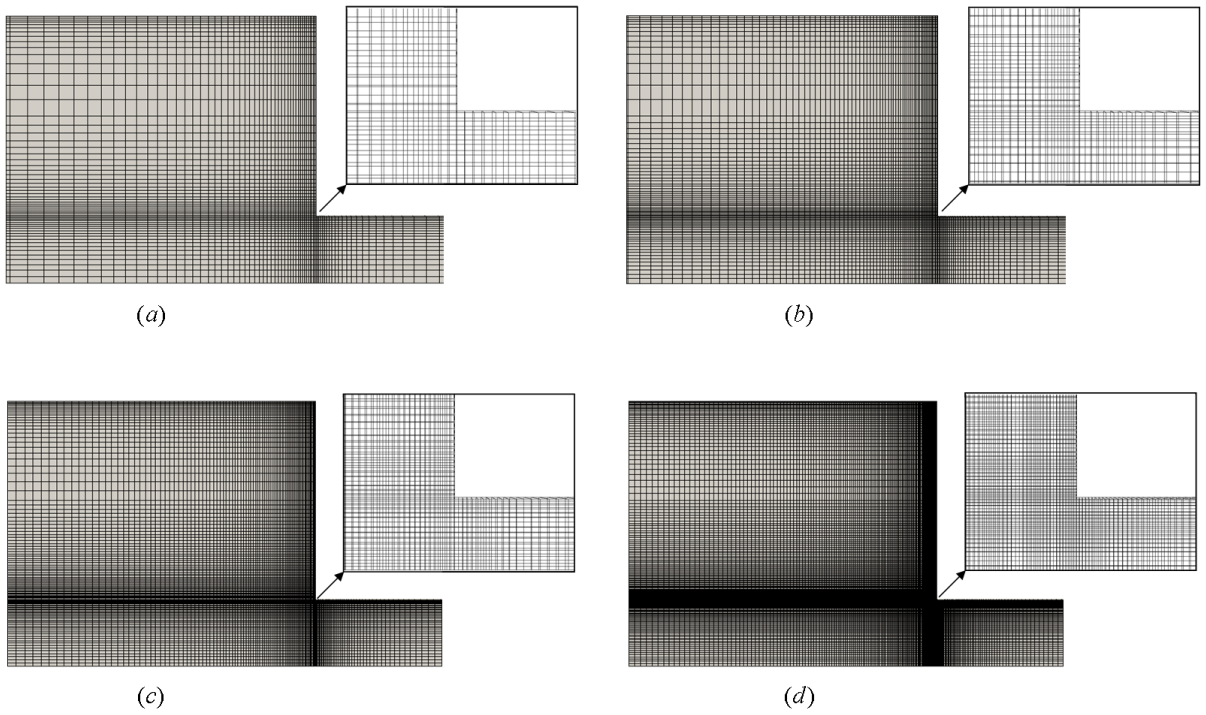

Figure 5.2: Computational meshes showing closer view of the re-entrant corner (a) M1 (b) M2 (c) M3 (c) M4

predicted by the MINMOD scheme show a better convergence of the vortex size with mesh refinement. These results demonstrate the better numerical accuracy of the higher-order MINMOD schemes. In the rest of the chapter, the accuracy of numerical solutions using the MINMOD scheme will be demonstrated by comparison with the results of Alves et al. [6], which were carried out using their high-resolution CUBISTA differencing scheme.

In Fig. 5.4 the effects of increasing Wi on the flow patterns for the Oldroyd-B fluid is presented. The results show a diminishing corner vortex and the appearance and enhancement of a tiny lip vortex as Wi is increased. A magnified view of the lip vortices is provided in Fig. 5.5. A minute lip vortex is barely visible at $Wi = 1.0$ very close to the re-entrant corner and it grows in size as Wi is increased. This behaviour is in agreement with the results of Alves et al. [6], which clearly predicts the shrinking of the corner vortex up to $Wi \approx 3$ and the appearance of a lip vortex at $Wi \approx 1.0$.

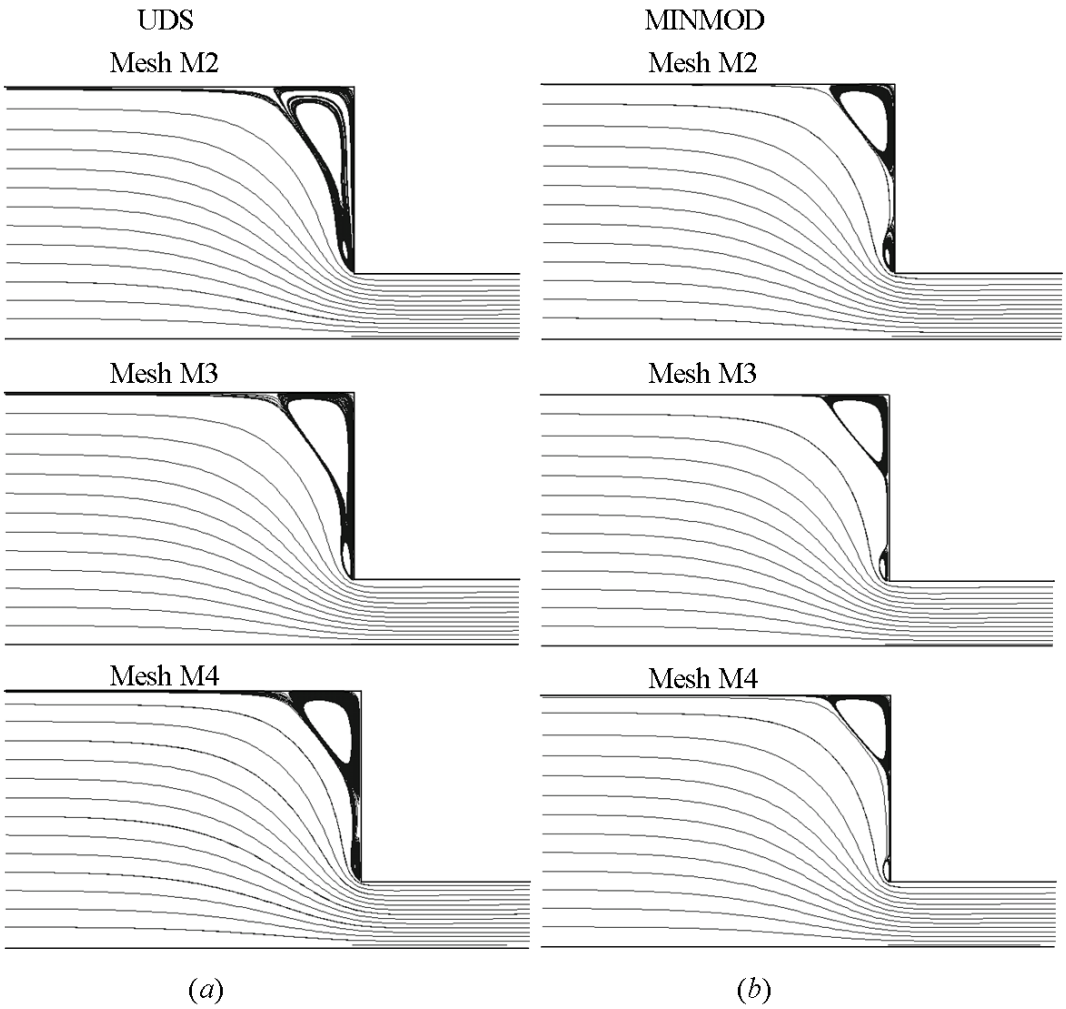

Figure 5.3: Streamlines for the Oldroyd-B fluid showing both effects of mesh refinement and differencing scheme for $Wi = 3$. (a) UDS scheme (b) MINMOD scheme

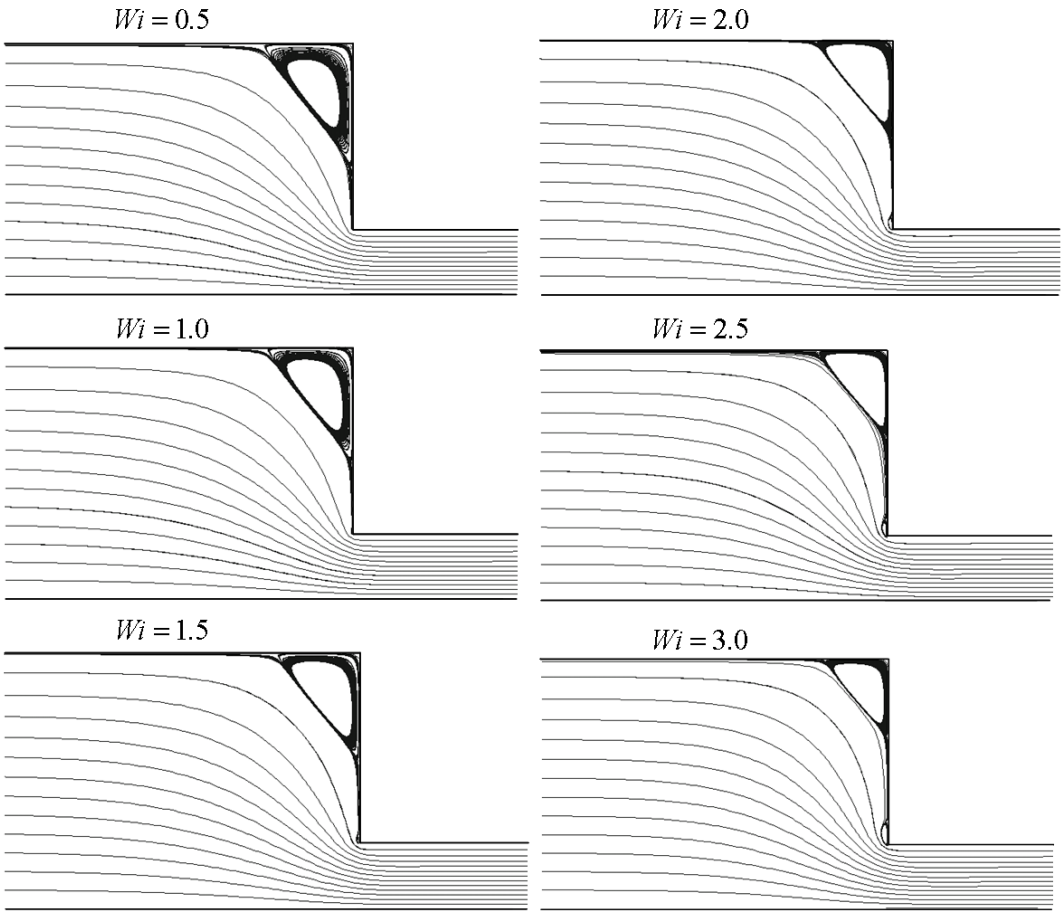

Figure 5.4: Streamlines for the Oldroyd-B fluid showing the effect of increasing Weissenberg number on flow pattern (Mesh M4)

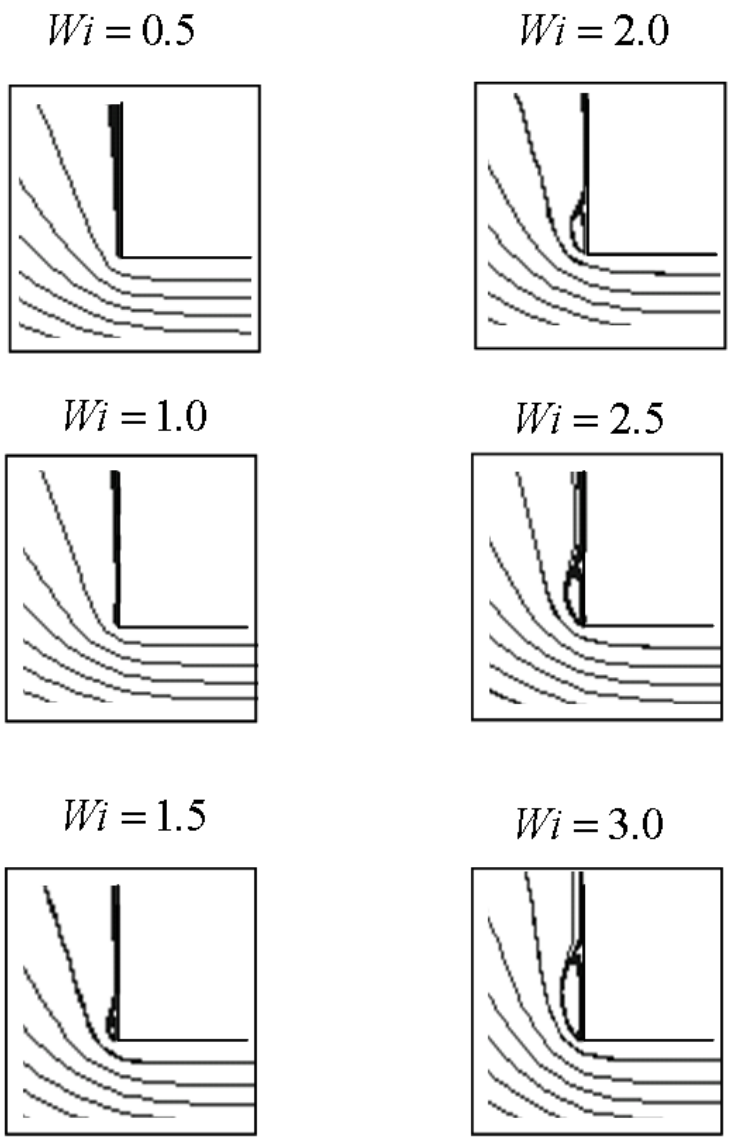

Figure 5.5: Flow patterns near the entrant corner showing lip vortices for the Oldroyd-B fluid (Mesh M4)

Quantitative comparison with the benchmark data provided by Alves et al. is presented in Table 5.2, comparing the following results: the dimensionless vortex size, χ_L , Couette correction coefficient, C, maximum value of the normal stress component along the centreline of the channel, $\tau_{xx,max}$, nomalised by $3U\eta/w_c$, and maximum value of axial velocity along the centreline of the channel, u_{max}, nomalised by U. It may be seen from the table that the present simulations show good agreement with those of Alves et al.

Corresponding plots of χ_L and C are provided in Fig. 5.6 and 5.7 for the three finer

meshes M2, M3, and M4, together with the results for mesh M6 of Alves et al. for comparison. As shown in Fig. 5.6, majority of the points are within very close range

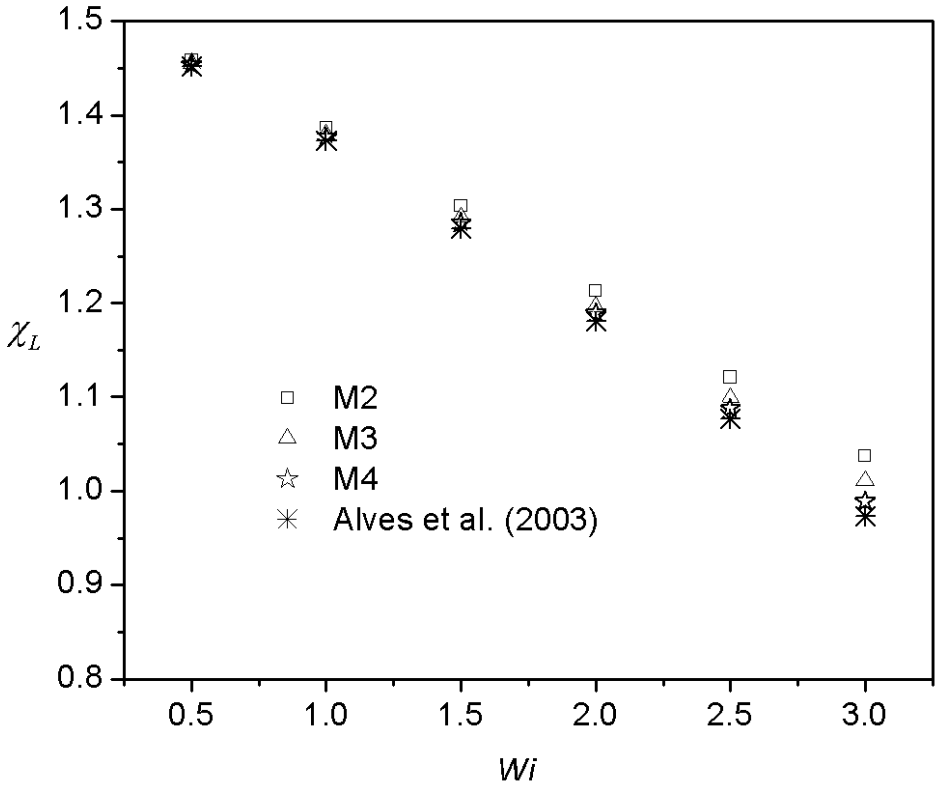

Figure 5.6: Effect of Weissenberg number on dimensionless vortex size, χ_L, for the Oldroyd-B fluid

with those of Alves et al., especially for mesh M4 except for higher values of Wi where slight deviations are noticeable. This is due to the better accuracy achieved by their mesh M6 ($NC = 169392$), which is much finer than mesh M4 ($NC = 55475$) in the present work.

The results of the Couette correction, C, in Fig. 5.7 show better agreement with those of Alves et al. for all three meshes (M2, M3, M4) and for the range of Wi examined. This result is indicative of a lesser sensitivity to mesh refinement for the Couette correction compared with the vortex size, χ_L. The straight line plot passing through the points is calculated from the correlation $C = 0.4281 - 0.9665Wi$ obtained by linear regression for $Wi \geq 1$ [6]. At low Wi, this value slightly deviates from a straight line. Negative values and linear variation of the Couette correction with Weissenberg number in the 4:1 planar

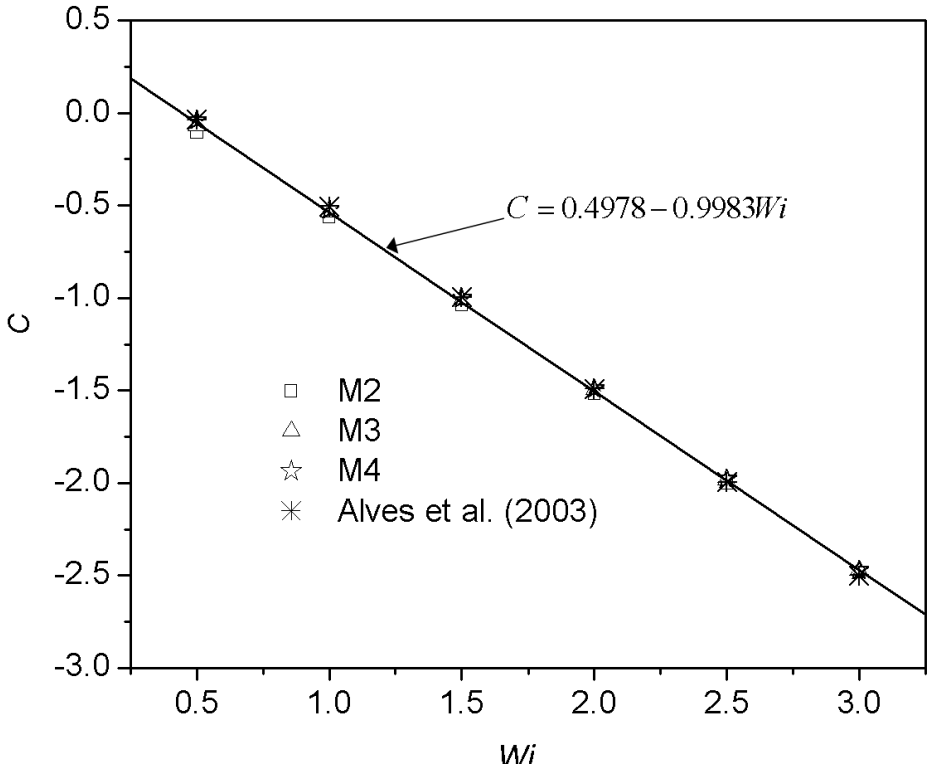

Figure 5.7: Effect of Weissenberg number on Couette correction, C, for the Oldroyd-B fluid

contraction is commonly observed for the upper convected Maxwell (UCM) and Oldroyd-B models in the literature [46, 121]. This is, however, in contrast to the values reported in experiments using Boger fluids, which have been largely been positive or at least barely distinguishable from that of corresponding Newtonian liquids with similar viscosity [122]. Therefore, the negative Couette correction predicted by this model suggests that the model cannot mimic some important rheological behaviours of Boger fluids in the non-linear flow regime.

The convergence of the predicted corner vortex size with mesh refinement is further demonstrated in Fig. 5.8. The plots show the vortex predicted by the meshes, M2-M4, as symbols and the line of best fit of Alves et al. obtained by curve-fitting through the minimum mesh spacing, $\triangle x_{min}$, for their finest meshes at $Wi = 2.5$. The quadratic convergence indicated by the exponent of $\triangle x_{min}$ in the expression validates the second-order accuracy of the numerical scheme used in this present work and the asymptotic behaviour of the dimensionless corner vortex as $\triangle x_{min} \rightarrow 0$.

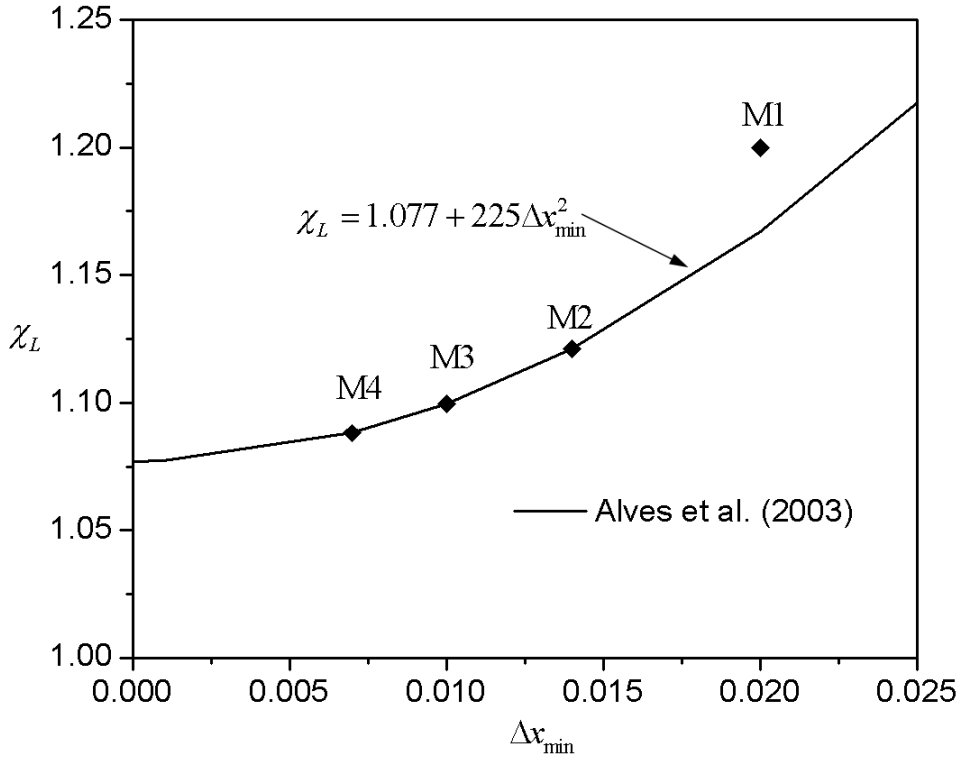

Figure 5.8: Convergence of dimensionless vortex size with mesh refinement for the Oldroyd-B fluid at $Wi = 2.5$

The asymptotic behaviour of the stress and velocity fields in the vicinity of the re-entrant corner are plotted in Figs. 5.9 and 5.10. Theoretical analysis [123] and numerical studies [46, 121, 6] have shown that near the re-entrant corner, for the Oldroyd-B fluid, the velocity component vanishes according to $u \propto r^{5/9}$ and $v \propto r^{3/4}$, and all the stress components go to infinity according to $\tau_{i,j} \propto r^{-2/3}$ for $\theta = 90^o$, i.e when r is measured cross-stream from the corner. The polar co-ordinate (r, θ) is centered at the corner as defined in Fig. 5.1. The figures show the log-log plots of nomalised values evaluated at a relatively low Weissenberg number, $Wi = 1.0$, in order to avoid significant lip vortex activity which may violate the assumptions of the asymptotic behaviour proposed by Hinch [123]. The plots validate the slopes 5/9 and 3/4 for the velocities, and -2/3 for stresses as the corner is approached. Away from the corner, i.e. as the wall is approached, the agreement is poor, as expected, since Hinch's theory is only valid in the re-entrant corner region.

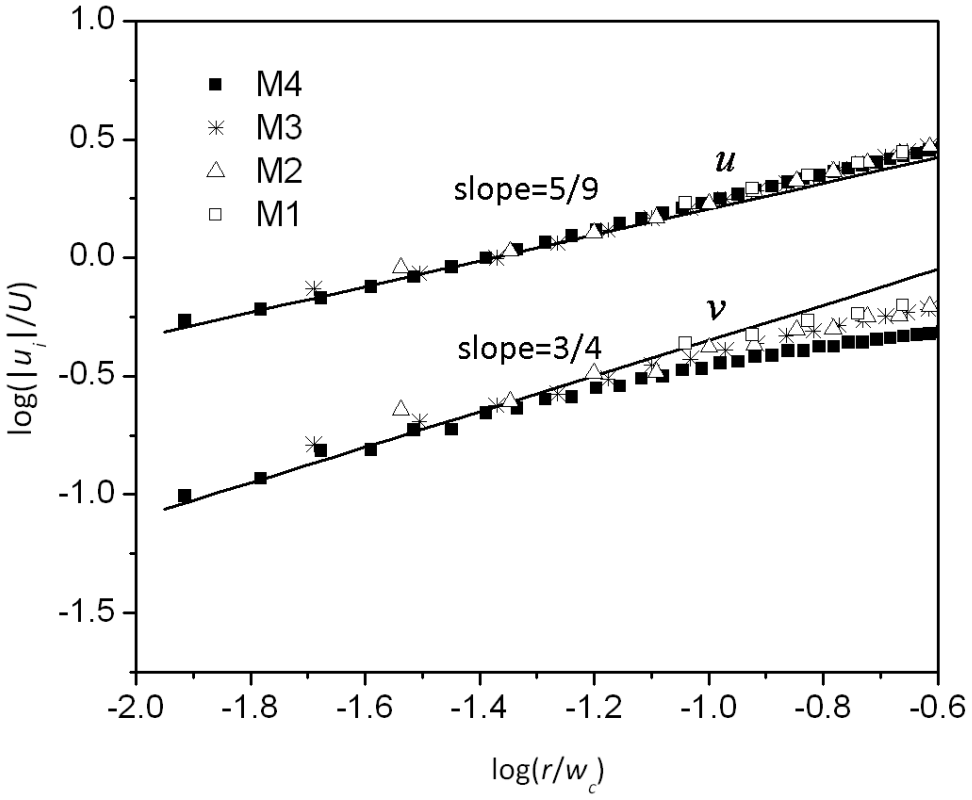

Figure 5.9: Asymptotic behaviour of the velocity fields near the re-entrant corner for the Oldroyd-B fluid at $Wi = 1$, plotted along the line $\theta = 90^o$. u and v are the horizontal and vertical velocity components respectively.

Wi	χ_L	χ_L^a	C	C^a	$\frac{\tau_{xx,max}}{(3U\eta/w_c)}$	$\frac{\tau^a_{xx,max}}{(3U\eta/w_c)}$	u_{max}/U	u^a_{max}/U
0.5	1.454	1.452	-0.039	-0.036	0.461	0.461	1.510	1.511
1.0	1.377	1.373	-0.522	-0.505	0.545	0.544	1.526	1.525
1.5	1.285	1.279	-1.00	-0.995	0.597	0.589	1.542	1.537
2.0	1.189	1.181	-1.490	-1.492	0.624	0.612	1.557	1.546
2.5	1.088	1.077	-1.980	-1.996	0.643	0.623	1.572	1.554
3.0	0.989	0.973	-2.473	-2.501	0.654	0.638	1.587	1.562

Table 5.2: Results for the Oldroyd-B fluid based on Mesh M4. [a]Alves et al. [6]

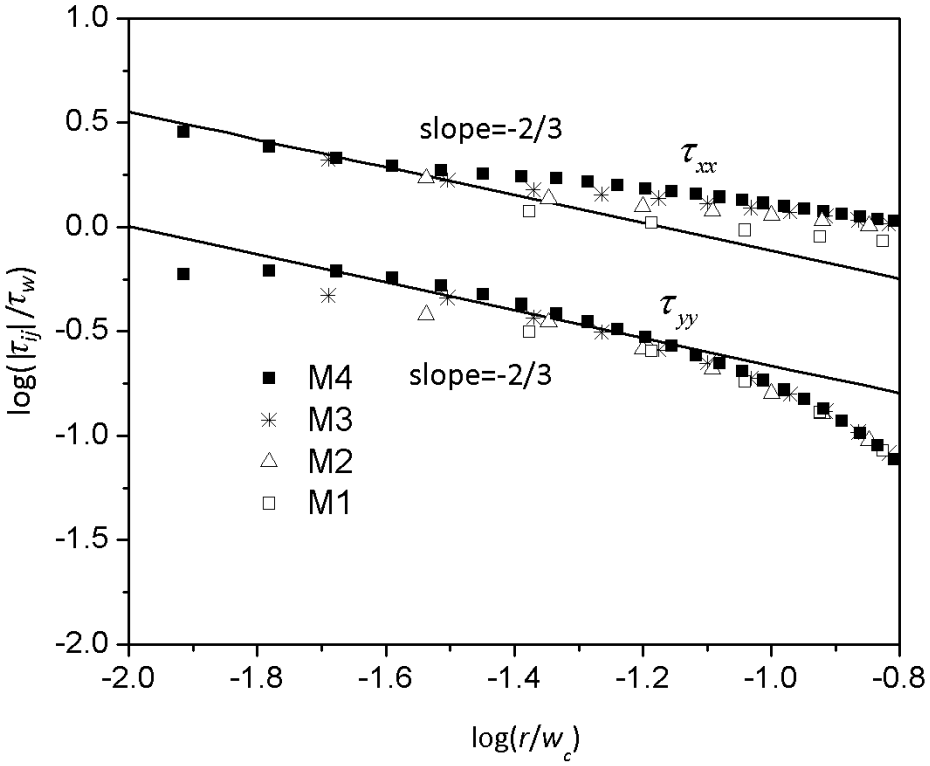

Figure 5.10: Asymptotic behaviour of the stress fields near the re-entrant corner for the Oldroyd-B fluid at $Wi = 1$, plotted along the line $\theta = 90^o$. τ_{xx} and τ_{yy} are the horizontal and vertical normal stress components respectively.

5.4 The Linear Phan-Thien-Tanner Fluid

Results are now presented for the L-PTT model using the parameters $\epsilon = 0.25$ and $\xi = 0$, which are standard values in the literature for the study of the contraction benchmark flow [46, 121, 6]. With these parameters the model predicts a shear-thinning behaviour for both the shear viscosity and first normal stress difference coefficient. For the purpose of comparison with benchmark data a number of calculations have been performed in the Weissenberg number range, $0.1 - 100$. The full set of data is provided in Table 5.3

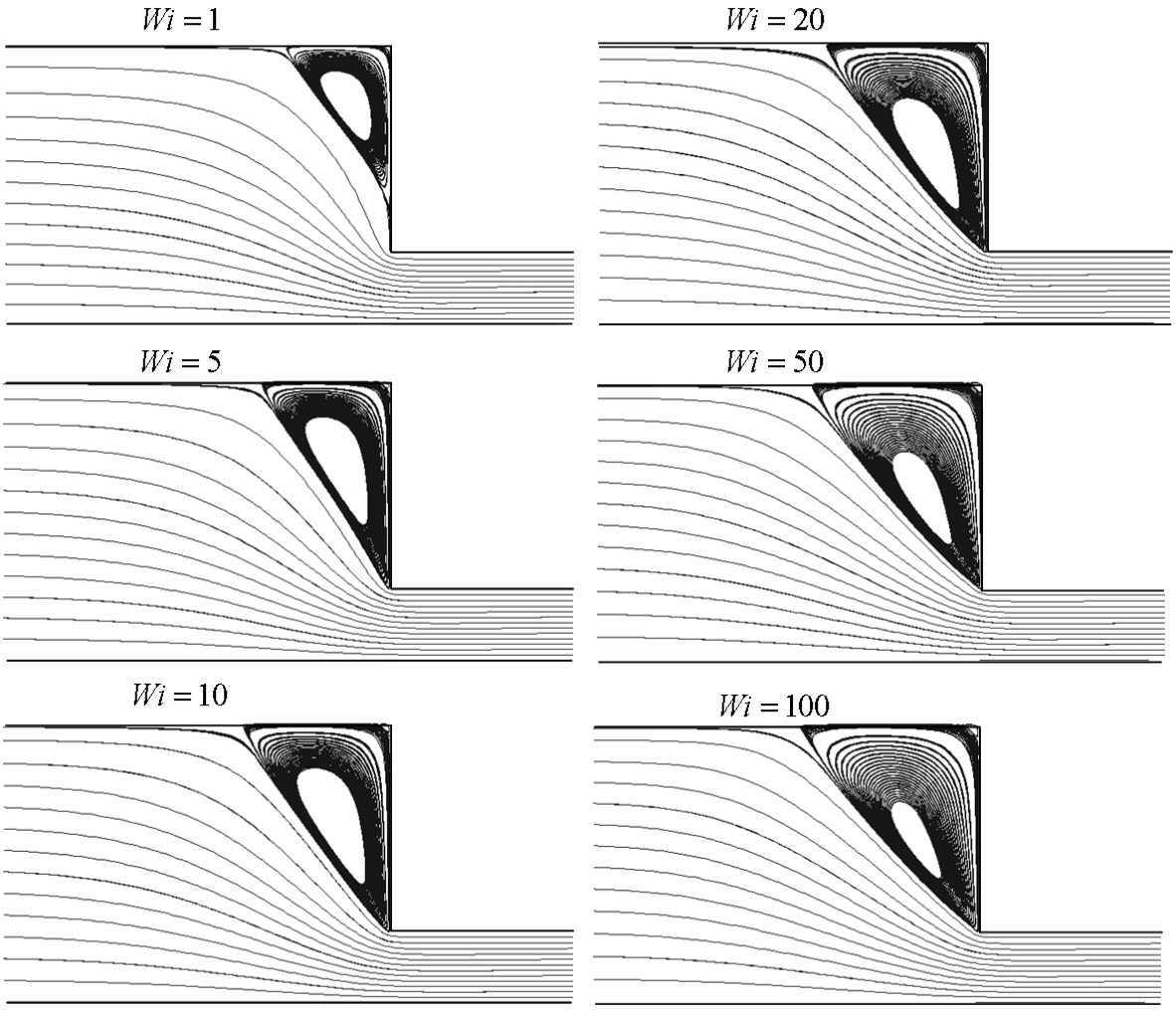

Figure 5.11: Streamlines for the L-PTT fluid showing the effect of increasing Weissenberg number on flow pattern (Mesh M4)

against corresponding benchmark results [6]. The flow patterns are presented in Fig. 5.11. This trend in vortex growth is remarkably different from those of the Oldroyd-B fluid. In

contrast to the result of the Oldroyd-B fluid, no lip vortex is predicted near the re-entrant corner and instead of shrinking, the vortex size is significantly enhanced with Wi. This is in good agreement with the results of Alves et al. [6]. In Fig. 5.12, the size of the dimensionless vortex is plotted against Wi. This plot replicates quantitatively and shows more clearly the trend depicted by the flow patterns in Fig. 5.11. An initial steep rise in the vortex size is seen at $Wi = 1$, which becomes saturated asymptotically afterwards at higher Wi.

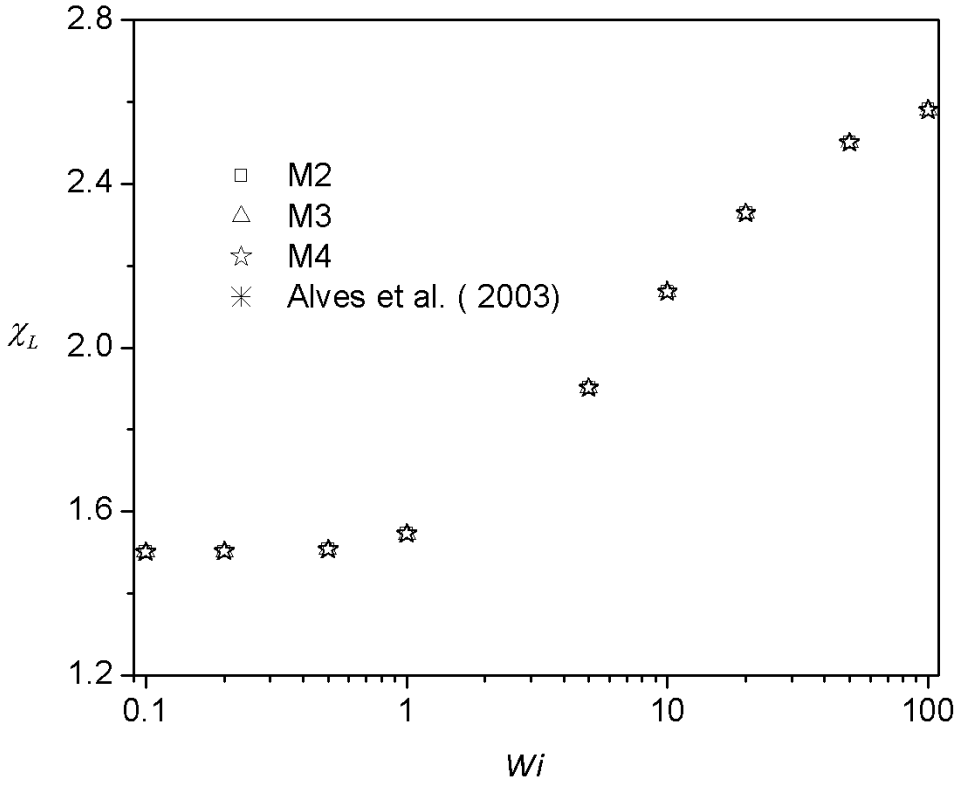

Figure 5.12: Effect of Weissenberg number on dimensionless vortex size, χ_L, for the L-PTT fluid

The plots of dimensionless pressure drop for the three finer meshes (M2-M4) provided in Fig. 5.13 also show good agreement with the results of Alves et al. computed by their finest mesh (M6). Contrary to the results of the Oldroyd-B fluid, the Couette correction for the L-PTT fluid shows a non-linear decline initially with Weissenberg number, then goes through a minimum into negative values, and eventually tends towards positive values at higher Wi. The positiveness of C indicates that the L-PTT model is at least capable of predicting some of the behaviour of polymer solutions in complex flows better

than the Oldroyd-B model. This is not unexpected as the Oldroyd-B model is known to posses an unrealistic elongational viscosity at $Wi \geq 0.5$, which might be responsible for its poor prediction of the Couette correction. The L-PTT model, on the other hand, possesses an elongational viscosity that remains bounded at high Wi.

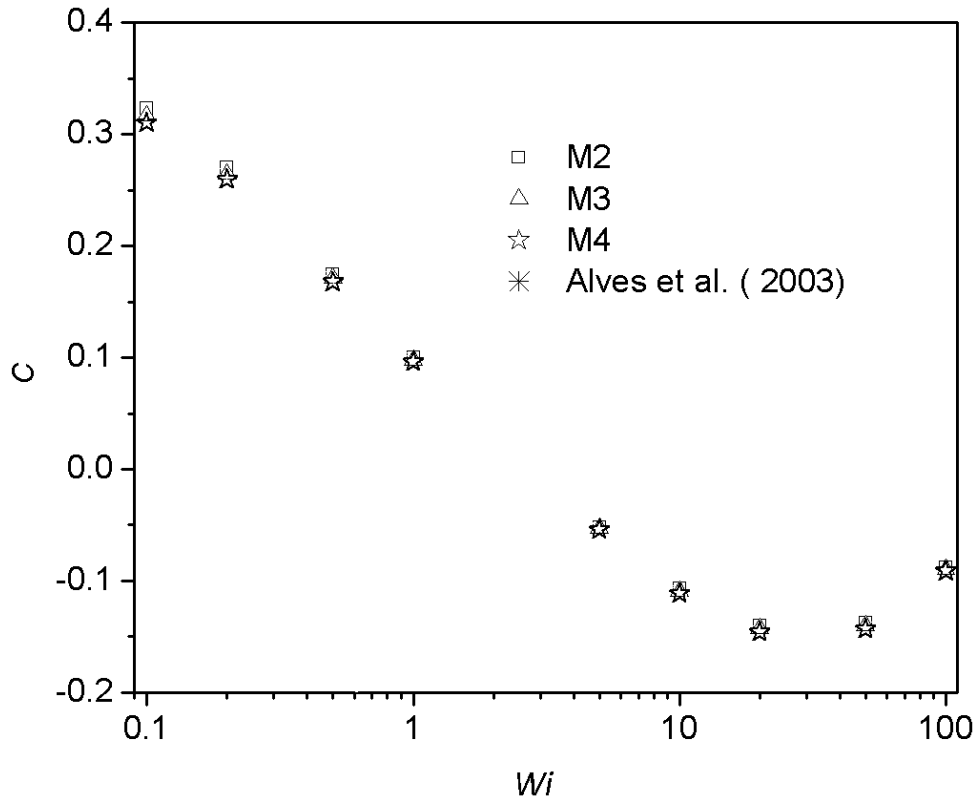

Figure 5.13: Effect of Weissenberg number on Couette correction, C, for the L-PTT fluid

In Figs. 5.14 and 5.15, profiles of normalised axial velocity and stress components along the centreline, $y = 0$, are presented to show the effect of increasing Wi. In Fig. 5.14, the inset shows the plot in closer range near the re-entrant corner to accentuate the behaviour of the velocities in that region. The trend shows an increasing streamwise velocity with elasticity. The plots also show identical characteristics with similar plots obtained by Alves et al. [6]. The maximum velocities are predicted just inside the downstream channel, which indicates the position of highest strain along the centreline. Immediately downstream, this maximum strain is not sustainable by the shear-dominated flow and the polymer relaxes relatively quickly after a distance of about 6 widths of the downstream channel. The length of channel required for the relaxation process after the stretching of the polymer increases with Weissenberg number, which may be determined

by evaluating the axial velocity gradient, du/dx, along the centreline of the downstream channel. The profile of normal stress component in Fig. 5.15 also resembles similar

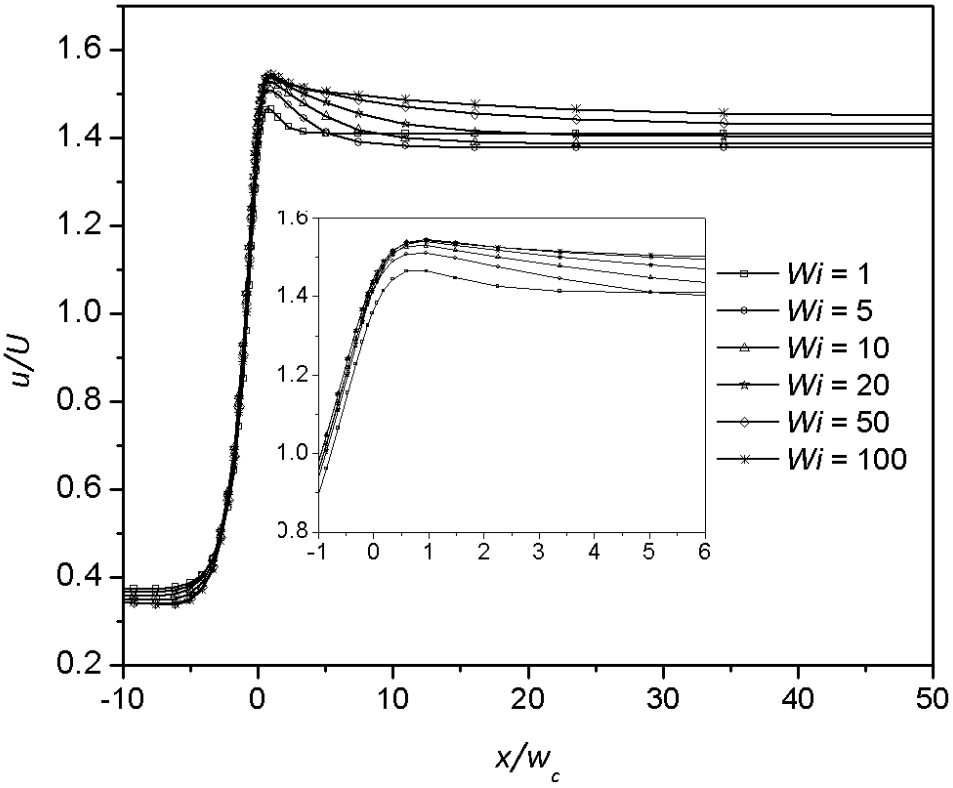

Figure 5.14: Profile of axial velocity component along centreline ($y = 0$) for the L-PTT ($\epsilon = 0.25, \xi = 0$) fluid

plots in the results reported in the literature [6]. In these plots, it might seem contrary to expectations that the maximum stress decreases with increasing Wi. As noted in the literature [6], this behaviour is due to the effect of shear-thinning at high Wi not accounted for by the constant scaling factor $\tau_{w0} = 3U\eta_0/w_c$. It is also noticeable that the position of the maximum stress is shifted downstream as Wi is increased.

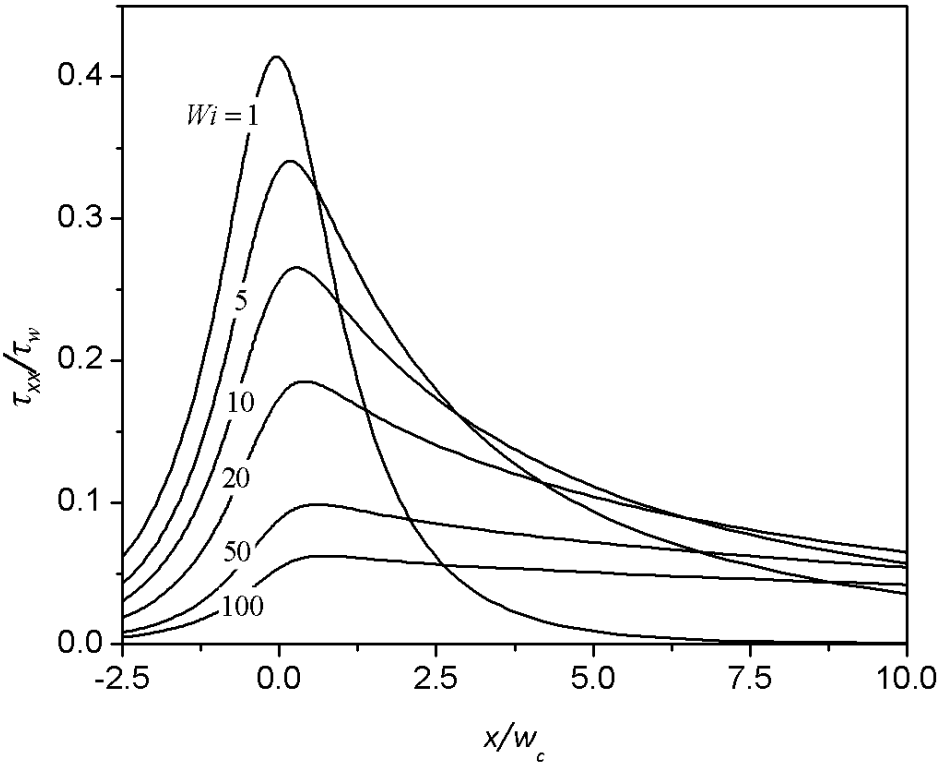

Figure 5.15: Profile of normal stress component, τ_{xx}, along centreline ($y = 0$) for the L-PTT ($\epsilon = 0.25, \xi = 0$) fluid

Wi	χ_L	χ_L^a	C	C^a	$\frac{\tau_{xx,max}}{(3U\eta/w_c)}$	$\frac{\tau^a_{xx,max}}{(3U\eta/w_c)}$	u_{max}/U	u^a_{max}/U
0.1	1.500	1.500	0.317	0.3092	0.354	0.349	1.495	1.495
0.2	1.502	1.501	0.265	0.2581	0.374	0.368	1.484	1.484
0.5	1.508	1.506	0.171	0.1672	0.399	0.399	1.464	1.465
1.0	1.545	1.542	0.098	0.0951	0.414	0.415	1.467	1.468
5.0	1.902	1.898	-0.060	-0.0551	0.341	0.340	1.511	1.512
10.0	2.137	2131	-0.111	-0.1113	0.266	0.264	1.530	1.531
20.0	2.328	2.321	-0.146	-0.1460	0.185	0.183	1.542	1.542
50.0	2.501	2.493	-0.143	-0.1444	0.099	0.092	1.545	1.544
100.0	2.581	2.570	-0.091	-0.0917	0.051	0.048	1.543	1.540

Table 5.3: Results for the L-PTT fluid based on Mesh M4. [a]Alves et al. [6]

5.5 Conclusions

In this chapter, the present numerical technique has been evaluated by performing finite volume calculations for the flow of the Oldroyd-B and L-PTT fluids in the 4:1 contraction flow. The simulations were validated against reliable benchmark data of Alves et al. [6] obtained using well-refined meshes based on a very stable numerical technique. The results have shown that the second-order accurate MINMOD differencing scheme used in this work is in fair agreement with the third-order accurate CUBISTA scheme used in the work of Alves et al. For both models, quantitative comparisons were made for dimensionless vortex size, χ_L , Couette correction coefficient, C, maximum value of the normal stress component along the centreline of the channel, $\tau_{xx,max}$, and maximum value of axial velocity along the centreline of the channel, u_{max}. The second-order accuracy of the present numerical scheme was validated by the quadratic convergence of the dimensionless vortex size with mesh refinement. The asymptotic behaviour of the stress and velocity fields in the vicinity of the re-entrant corner were also quantified and compared with numerical and theoretical predictions. The stability of the present numerical scheme is also demonstrated by the high values of Wi attained with the level of mesh refinement used in this work.

Part III

Elastic Dynamics in Complex Flows

Chapter 6

Elastic Instability of Extensional Flow in Cross-slots

6.1 Introduction

The cross-slot geometry is very useful for rigorous validation of constitutive equations because the strains generated in it can reach much higher values in comparison to the contraction geometry. The defining feature of this device is the presence of an interior stagnation point, and fluid elements entering this region may become fully stretched by prolonged exposure to a well-defined extensional strain. The cross-slot geometry was designed with the aim of stretching polymer chains to the limit by extensional flows. de Gennes and a group of researchers at the H.H. Wills Physics Laboratory, Bristol pioneered many of the works on polymer chain stretching in the cross-slot [124]. This geometry originated from the four roll mill device, which was later modified to the six roll mill and the opposed jet apparatus in order to achieve higher strain rates. The devices are characterised by inhomogeneous extensional deformation along the outflow symmetry axis close to the stagnation point, which significantly stretches the polymer molecules in this region.

Experimental studies in such extensional flow devices have shown that the stretching of dilute polymer solutions can generate very large stresses [125, 126]. This so-called extra dissipative stress could not be predicted by simple FENE dumbbell models [126]. The physical mechanism by which it occurs has long been of interest to experimentalists be-

cause of the hysteretic behaviour of dilute polymer solutions during relaxation following an extensional flow. Theoretical and numerical evidences have associated this phenomenon with the non-linear hydrodynamic coupling between the evolution of the dumbbell and the applied macroscopic flow field [97, 127, 100].

Elastic flow instability is of interest in rheometric flow devices because of the destabilising effect they have on them [125]. The study of this phenomenon in microfluidic cross-slot flows is only a recent research activity [19, 128] and very little is known about its origin and nature. Arratia et al. [19] reported two instability modes for the flow of a dilute polymer solution in a cross-slot microchannel. In the first instability, the flow becomes asymmetric but remains steady above a critical Wi. This was followed by a supercritical transition into a time-dependent bistable flow characterised by velocity fluctuations.

The flow regimes described above have been predicted recently by numerical simulations using constant drag models [129, 130]. In this chapter, simulations will be presented for the Phan-Thien-Tanner model as well as the constant drag and the non-linear drag FENE dumbbell models. For the non-linear drag, the FENE-CD-JS model described in this thesis (see Chapter 3) will be used with the Larson's friction law [1]. The model parameters, the geometry and boundary conditions as well as the results of the mesh validation will be presented in Section 6.2. In Section 6.3, the models will be compared by their predictions in symmetric flow, and in Section 6.4, the time-dependent behaviour of the models will be discussed using stability diagrams.

6.2 Model Prediction and Geometry

Fig. 6.1 shows the prediction of the models, L-PTT($\xi = 0$), FENE-CR ($\xi = \kappa = 0$), and FENE-CD-JS ($\xi > 0, \kappa = 0.002$) for selected parameter space in homogeneous shear and planar extension. The FENE-CD-JS model is used with Larson's friction law, $\kappa = 0.02$. For FENE-CD-JS and L-PTT, the value of ξ is chosen in order to eliminate the effect of shear-thinning (or shear-thickening) and allow for comparison of results between models. The selected material functions will also enable comparison with the literature results [130], which are also based on these values. As may be seen from the figure, the L-PTT

model predicts some shear-thinning even for a value of $\xi = 0$ because the shear-thinning behaviour of the model is loosely coupled with its extensional component through ϵ. The elongational viscosity of the models is controlled by the non-linear parameter, ϵ, for the L-PTT model, and L for the FENE dumbbell models. In the FENE-CD-JS model there is also a contribution from κ, which is only noticeable in the plot for the higher extensibility parameter, $L^2 = 100$. The prediction of the extensional viscosity by the three models are very similar, which is more important than their shear rheology in the present study. Elastic instability in the cross-slot is usually predicted at very low Wi [129], and hence the stabilising effect of shear-thinning is not of significant importance. However, in the FENE-CD-JS model, this parameter is necessary to eliminate the unwanted shear-thickening behaviour of the original model and to predict realistic first and second normal stress differences as discussed in Chapter 3. In the contraction flow, the stabilising effect of ξ on the FENE-CD-JS model is extremely important in order to enable calculations up to high Wi because of the comparably low deformation rates achievable in such a geometry (see Chapter 7).

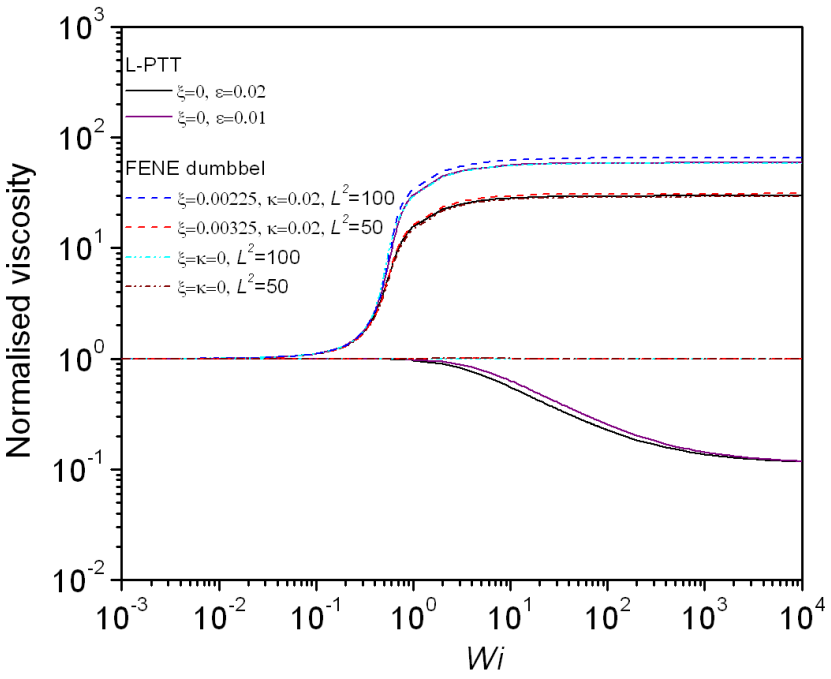

Figure 6.1: Normalised shear and elongational viscosities for the L-PTT (___), FENE-CR (_ . . . _), and FENE-CD-JS (_ _ _) models. All values have been normalised by the corresponding values at limiting zero-deformation rate.

The two corresponding sets of the extensibility parameters represented in the plots will be used for this study. As shown by the plots of the elongational viscosities the set of corresponding parameters are ($\epsilon = 0.02, L^2 = 50$) and ($\epsilon = 0.01, L^2 = 100$) for the L-PTT and FENE dumbbell models. For the purpose of this study, these sets of parameters will be referred to as $E1$ and $E2$, respectively.

The geometry of the cross-slot device is shown in Fig. 6.2. It consists of two inlet and two outlet channels. The channel lengths are chosen to be 10 channel widths (i.e. $10d$) to allow for complete flow development in the inlet arms and its re-development in the outlets. To quantify elasticity the Weissenberg number is defined as $Wi = \lambda U/d$,

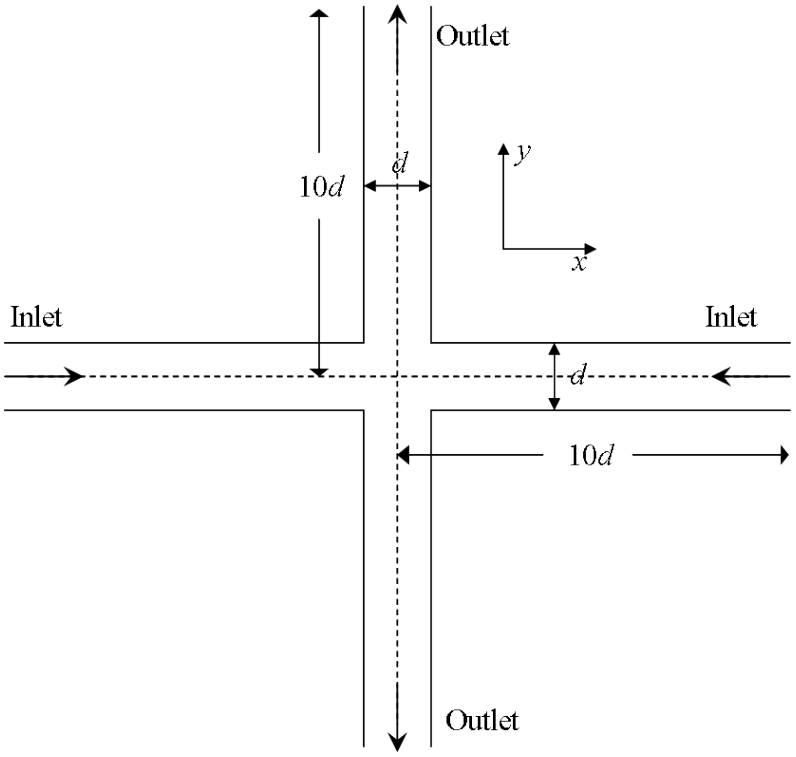

Figure 6.2: The schematics of the cross-slot geometry showing the inflow and outflow lines of symmetry represented by the horizontal and vertical centrelines.

where U is the mean velocity in the flow. The simulations are implemented using pressure driven boundary condition. The same pressure gradient is applied across one inlet and one outlet boundary by specifying the pressure at the inlet and zero pressure at the outlet. A homogeneous Neumann condition is prescribed for the velocity and stress fields at both the inlet and outlet boundaries. A no-slip condition is prescribed along the walls. In

all the simulations inertia is neglected and the ratio of the solvent viscosity to the total viscosity is set to $\eta_s/\eta = 1/9$.

The results of the stress fields are reported through the flow induced birefringence (FIB), which is related to the stress tensor by the stress-optical rule given by $\triangle n = C_o\sqrt{N_1^2 + 4\tau_{xy}^2}$, where the expression, PSD $= \sqrt{N_1^2 + 4\tau_{xy}^2}$, is the principal stress difference, and C_o, the stress optical coefficient, is a function of the solvent. FIB gives information about the deformation of the polymer providing the stress-optical rule holds. For the strong extensional flow region along the symmetry line the PSD is given by the first normal stress difference, N_1, in the pure shear flow region near the wall, it is given by the twice the wall shear stress, $2\tau_{xy}$, and elsewhere by a contribution from both N_1 and $2\tau_{xy}$.

The mesh density dependence of the solution is investigated using meshes M1 and M2 shown in Figs. 6.3 and 6.4. The number of cells for M1 and M2 are 17,500 and 43,125, and their minimum dimensions are given by $\triangle x_{min}/d = \triangle y_{min}/d = 0.02$ and 0.0133, respectively. The meshes are more refined in the region of the stagnation point and around the corners as shown in the magnified view. Figs. 6.5 and 6.6 show the profiles of normalised velocity magnitude and PSD along the outflow symmetry axis of the channel for L-PTT at $Wi = 1$. The distance along the channel is normalised by the channel width, d, the velocity is normalised by the mean value, U, and the PSD by the viscous stress component, $2U\eta/d$. The results show that the profiles of the velocity and stress fields for the two meshes are in close match. The numerical results presented in the remainder of this chapter have been computed using Mesh M1.

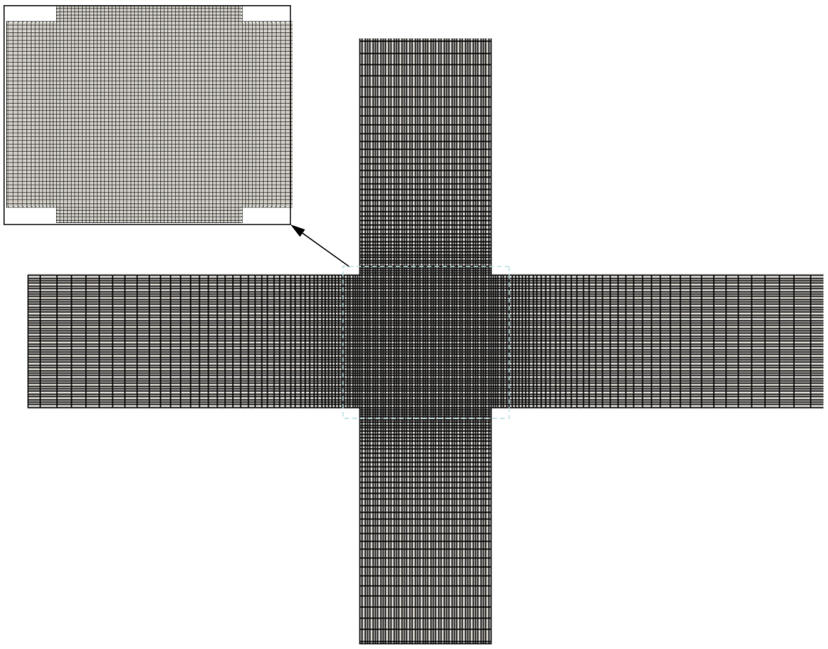

Figure 6.3: 2-D mesh for the cross-slot geometry, Mesh M1

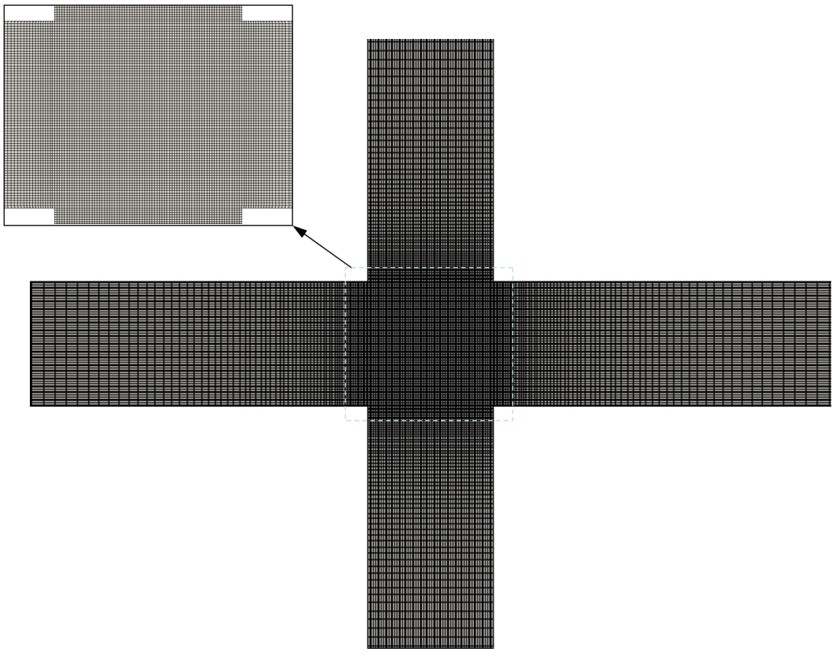

Figure 6.4: 2-D mesh for the cross-slot geometry, Mesh M2

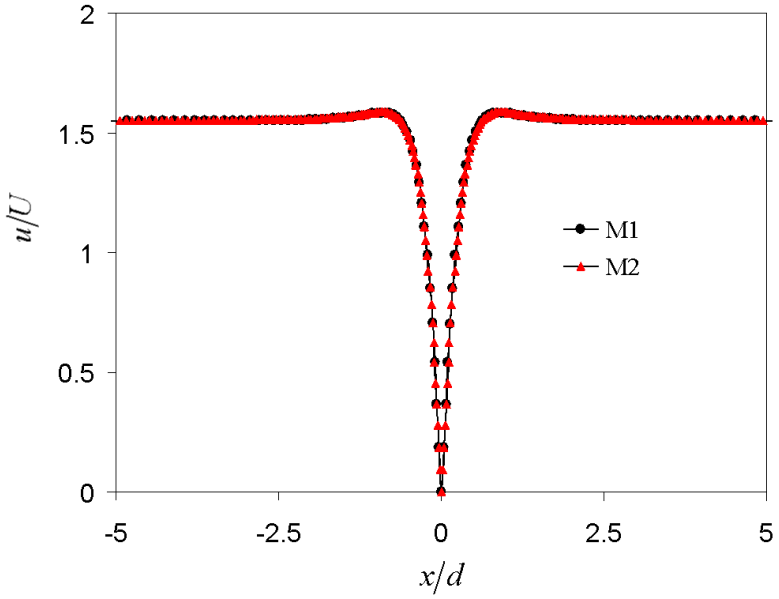

Figure 6.5: Profiles of normalised velocity magnitude along the symmetry line of outlet channel (x=0) for L-PTT, $Wi = 1$

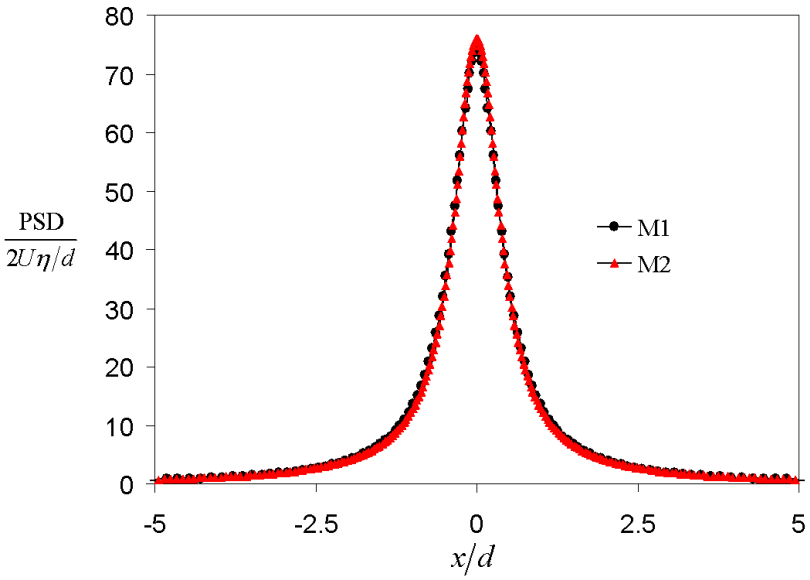

Figure 6.6: Profiles of normalised PSD along the symmetry line of outlet channel (x=0) for L-PTT, $Wi = 1$

6.3 Symmetric Flow

Firstly, the prediction of the models in the symmetric flow regime will be studied. Due to the effect of non-linear drag, the FENE-CD-JS model behaves very differently from the L-PTT and FENE-CR models in this regime. In order to make comparison between the models in the symmetric flow regime, a value of $Wi = 0.2$ has been selected at which a symmetric flow pattern may be obtained for all three models (see stability diagrams in Section 6.4).

In Figs. 6.7 and 6.8, the contour plots of the PSD at $Wi = 0.2$ for the three models are compared for matching peak elongational viscosities in the homogeneous flow. The extensional viscosity of the models can be approximately correlated with the molecular weight, M_w, of the polymer by a simple scaling, $M_w^{1/2}$. In Fig. 6.7, the results show that the FENE-CD-JS model predicts a much more extended PSD than the other models for the extensibility parameter, $E1$, due to the effect of the non-linear drag on the model. This behaviour is typical of the conformation-depended drag model and it is said to be responsible for the long birefringent strands that has been observed for dilute polymer solutions in the cross-slot [131].

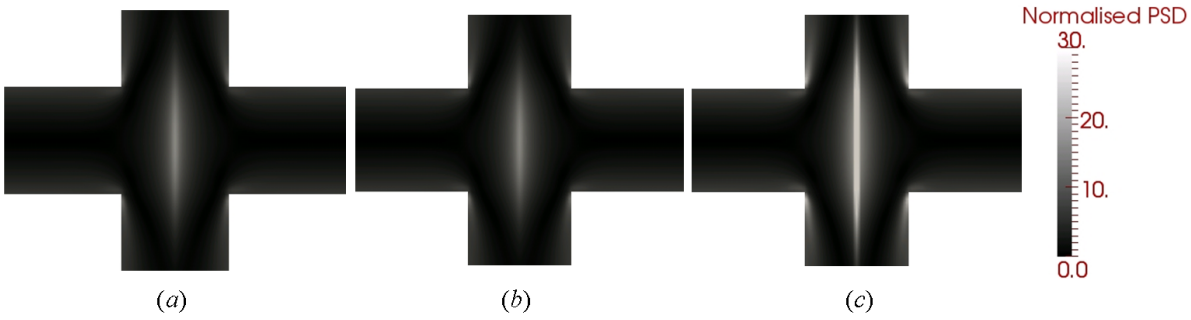

Figure 6.7: Contour plot of PSD, normalised by the viscous stress component, $2U\eta/d$, at $Wi = 0.2$ for the extensibility parameter $E1$, (a) L-PTT ($\epsilon = 0.02$), (b) FENE-CR ($L^2 = 50$), and (c) FENE-CD-JS ($L^2 = 50$).

In the non-linear drag model, the dumbbell spring is rapidly stretched by the flow due to the increased drag force generating a longer birefringent strand compared with the constant drag models. By contrast, the constant drag models are only extended by a

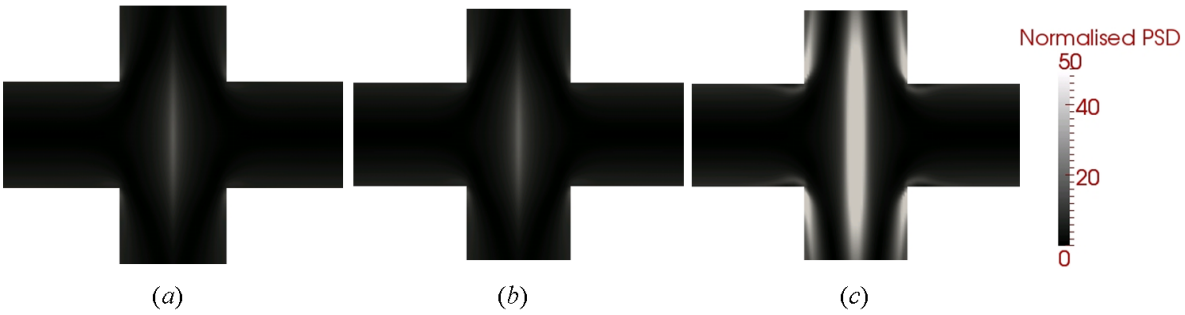

Figure 6.8: Contour plot of PSD, normalised by the viscous stress component, $2U\eta/d$, at $Wi = 0.2$ for the extensibility parameter $E2$ (a) L-PTT ($\epsilon = 0.01$), (b) FENE-CR ($L^2 = 100$), and (c) FENE-CD-JS ($L^2 = 100$).

relatively small amount by the velocity gradients along the centreline. The effect of drag on ultradilute polymer solutions have been demonstrated by the buckling of birefringent strands in a microfluidic cross-slot [128], which was due to the strands being highly elastic in nature, were slow to relax following a rapid extension. This slow relaxation process may be explained as the effect of the friction grip on the polymer molecules due to the large size that the flow can grasp in the stretched molecules. The stretching of the dumbbell in the FENE-CD-JS model is governed by both the extensibility parameter, L, and the drag coefficient, κ. In Fig. 6.8, the effect of a longer molecular chain on the PSD is illustrated by the extensibility parameter, $E2$. The result shows a larger extension for the models, which is significantly greater and broader for FENE-CD-JS. Thus, $E2$ effectively increases the length and width of the PSD strand.

These results are reflected in the profiles of the PSD and the velocity along the symmetry line of the outlet channel in Fig. 6.9-6.12. It is noticeable from the plots in Fig. 6.9 that the L-PTT and FENE-CR models predict a similar magnitude of PSD, while L-PTT is slightly greater closer to the stagnation point for $E1$. In the profiles for $E2$ shown in Fig.6.10, the FENE-CR model predicts more extension than the L-PTT model. This behaviour of the models is also depicted by the velocity profiles in Figs. 6.11 and 6.12. The FENE-CD-JS model exhibits a much broader velocity profile in comparison with the other models.

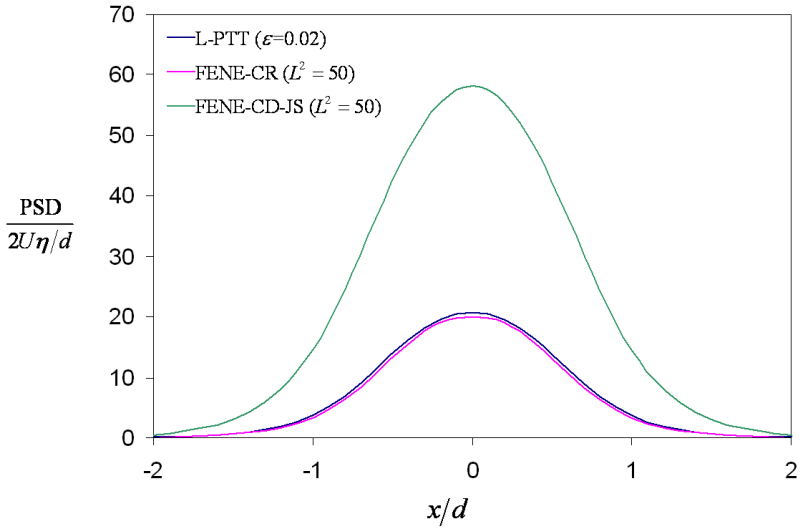

Figure 6.9: Profiles of normalised PSD along the symmetry line of the outlet channel for the extensibility parameter $E1$ ($Wi = 0.2$) (a) L-PTT ($\epsilon = 0.02$), (b) FENE-CR ($L^2 = 50$), and (c) FENE-CD-JS ($L^2 = 50$).

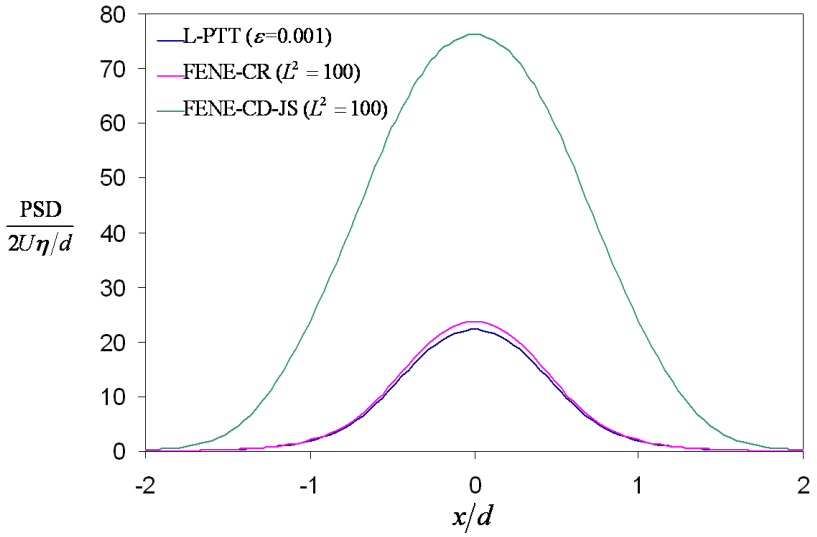

Figure 6.10: Profiles of normalised PSD along the symmetry line of the outlet channel for the extensibility parameter $E2$ ($Wi = 0.2$) (a) L-PTT ($\epsilon = 0.01$), (b) FENE-CR ($L^2 = 100$), and (c) FENE-CD-JS ($L^2 = 100$).

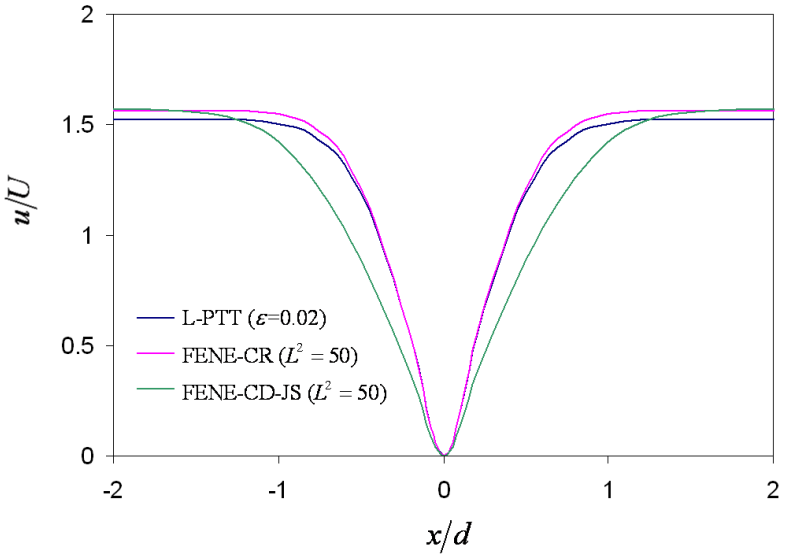

Figure 6.11: Profiles of normalised velocity magnitude along the symmetry line of the outlet channel for the extensibility parameter $E1$ ($Wi = 0.2$) (a) L-PTT ($\epsilon = 0.02$), (b) FENE-CR ($L^2 = 50$), and (c) FENE-CD-JS ($L^2 = 50$).

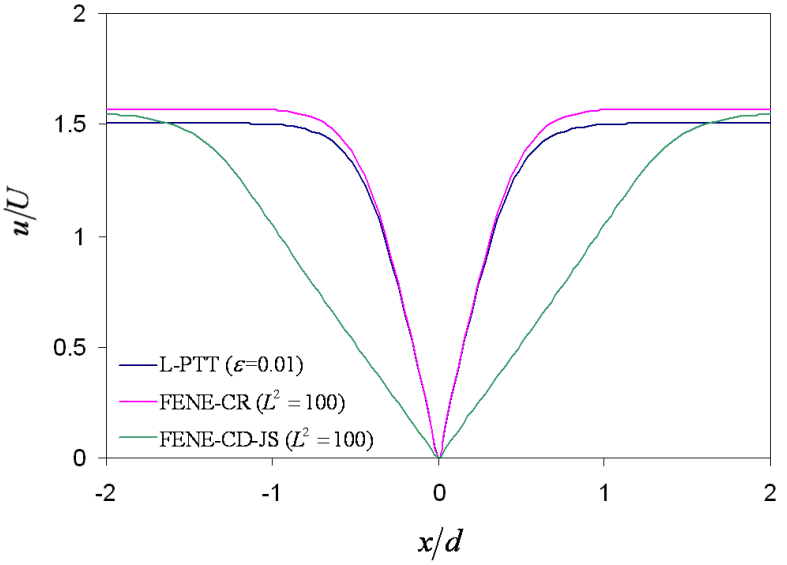

Figure 6.12: Profiles of velocity magnitude along the symmetry line of the outlet channel for the extensibility parameter $E2$ ($Wi = 0.2$) (a) L-PTT ($\epsilon = 0.01$), (b) FENE-CR ($L^2 = 100$), and (c) FENE-CD-JS ($L^2 = 100$).

These results are in agreement with experimental studies in the cross-slot [132, 128], which indicate that birefringent strands along the symmetry of the outflow channel could be stretched to approximately 10 channel widths downstream of the stagnation point. It has been shown numerically that the FENE-CD model predicts substantially more stretching than the FENE-CR model in closer agreement with experimental results [98]. Comparing the present results of L-PTT and FENE-CR shows that FENE-CR predicts relatively more extension for the long-chain polymer, i.e. for $E2$, which depicts the more realistic microstructural dynamics embedded in the model.

The behaviour of the FENE-CD-JS model is indicative of the large extensional stresses that can arise in the flow when polymer solutions are subject to highly stretching flows. Experimental studies in the cross-slot using ultradilute polymer solutions have reached extreme extensions of the birefringent strand and achieved a Trouton ratio, η_E/η, of up to 1000 in the high El flow regime [128]. Such a high Trouton ratios had not been previously reported in low El or high Re cross-slot flows of ultradilute polymer solutions, which suggests that the elasticity number plays a significant role in achieving such a high stretching. In high El flows, highly stretched polymer molecules may drive the flow unstable because of the build up of large stresses in the flow, which have to be dissipated by some means. The mechanism by which this occurs in the cross-slot is by symmetry-breaking, in which the flow assumes one or more asymmetric flow configurations. In this flow structure, more of the fluids elements coming from each of the inlet channels flows out through one of the exit channels. At this point, further increase in strain rate in order to stretched the polymer molecules more may cause a flow transition from a steady asymmetric flow to a time-dependent flow to minimise energy, and the flow may not settle down to a final steady-state [19, 129].

6.4 Stability Diagrams

The numerical simulation results are presented to study asymmetric instability regimes obtainable in the cross-slot. The two parameters controlling stretching of polymer chains are Wi and $\varepsilon = \dot{\varepsilon}t$ [95, 124], where ε and $\dot{\varepsilon}$ are the strain and strain rate respectively. In the cross-slot, these conditions for highly stretching of polymer molecules may only be

satisfied for molecules passing close to the symmetry line in the vicinity of the stagnation point. It had been previously suggested [129] that asymmetric instability originates from highly stretched molecules in the region of curved streamlines, which generates a secondary rotational flow by a similar mechanism as obtained in the elastic Taylor-Couette flow. Once the flow becomes asymmetric the stagnation point vanishes and the strain on the molecules are partly relaxed. In view of this, stability diagrams have been constructed using Wi and ε, where ε is evaluated as the product of the strain rate, du_y/dy, at the stagnation point and the simulation time t, i.e. a measure of the duration of the strain endured by the polymer molecule.

Stability diagrams for the L-PTT and FENE dumbbell fluids are provided in Figs. 6.13-6.17. Three flow regimes are captured in the simulations: a steady symmetric flow, a steady asymmetric flow, and an unsteady asymmetric flow. These flow patterns are illustrated by the PSD contour plots in Fig. 6.15.

Comparing Fig. 6.13 with 6.14 shows very little distinction between the stability behaviour of L-PTT ($\epsilon = 0.01$) and FENE-CR ($L^2 = 100$). The critical Wi for flow transition from steady symmetric to asymmetric flow for FENE-CR is approximately 0.45, but it is slightly higher for the L-PTT fluid. In the stability diagram, the lower boundary delineates the steady symmetric flow regime from the steady asymmetric flow regime. At values of Wi below Wi_{cr} the flow remains steady and symmetric for all values of ε. As Wi is increased, lesser strain is required for flow transition to occur due to the increased elasticity. The fluid cannot sustain the strain rate at the stagnation point for a long period of time and the flow becomes asymmetric by an energy reduction mechanism in order to reduce the strain. Further increase in Wi beyond the supercritical value ≈ 1 results in the development of a time-dependent flow structure to maintain a low strain in the strong flow regime. In this regime, the flow is unsteady and asymmetric.

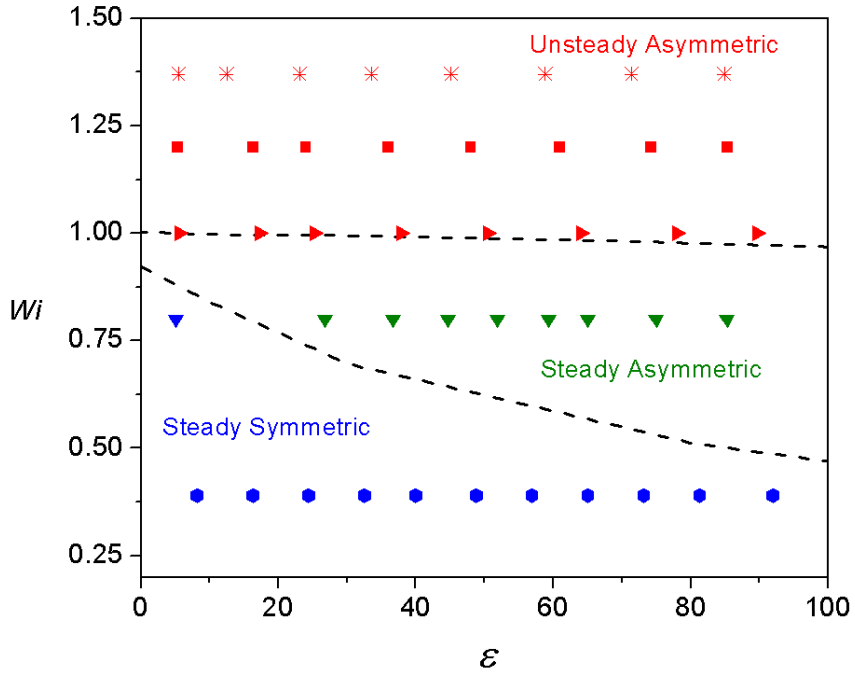

Figure 6.13: Stability diagram for the L-PTT model ($\epsilon = 0.01$)

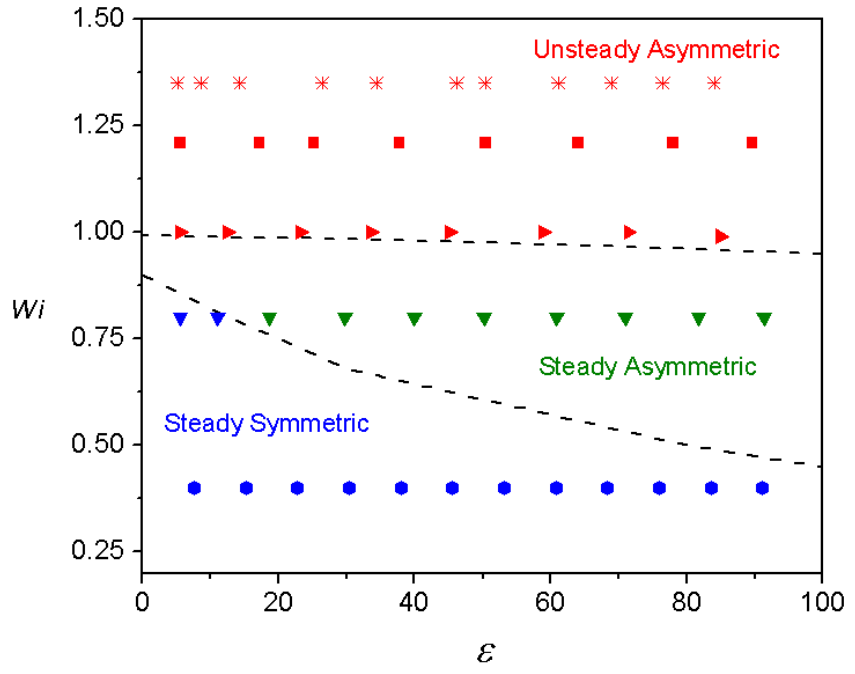

Figure 6.14: Stability diagram for the FENE-CR model ($L^2 = 100$)

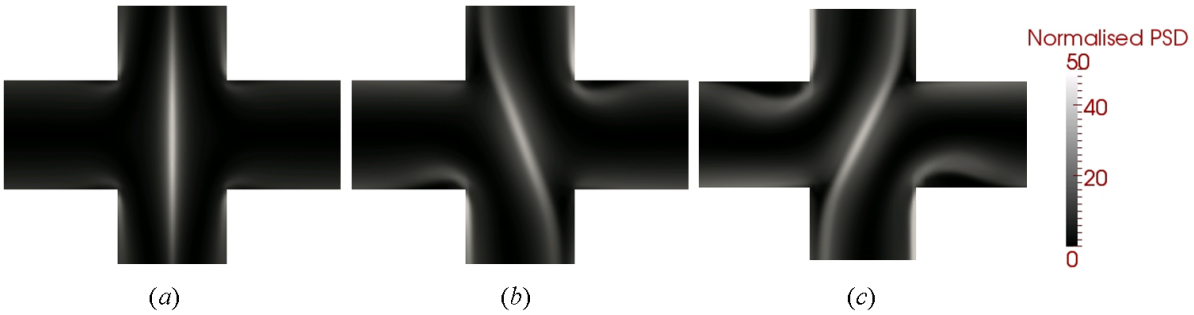

Figure 6.15: PSD for L-PTT ($\epsilon = 0.01$) normalised by the viscous stress component $2U\eta/d$ (a) steady symmetric, $Wi = 0.4$ (b) steady asymmetric, $Wi = 0.8$ (c) unsteady asymmetric, $Wi = 1.25$.

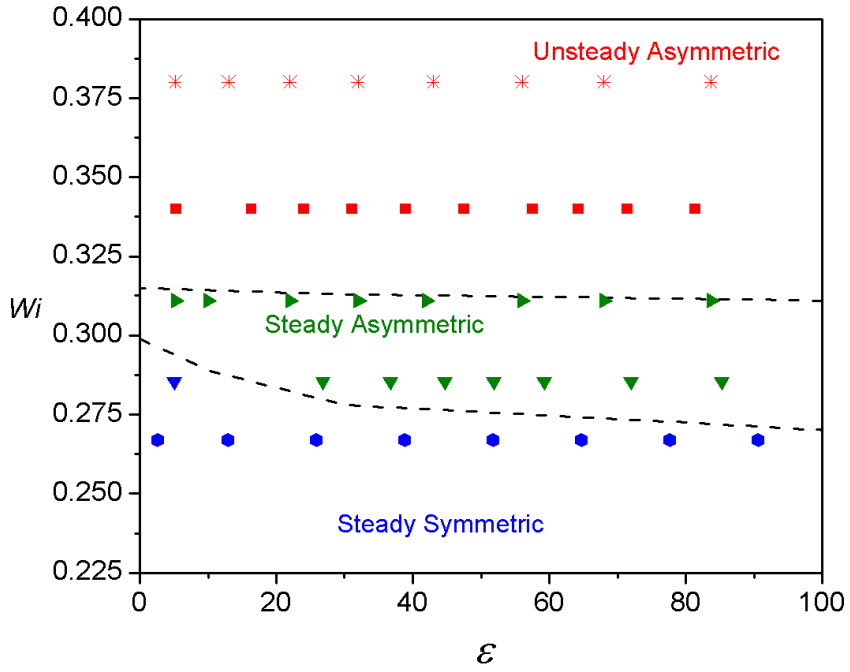

Figure 6.16: Stability diagram for the FENE-CD-JS model ($L^2 = 50$)

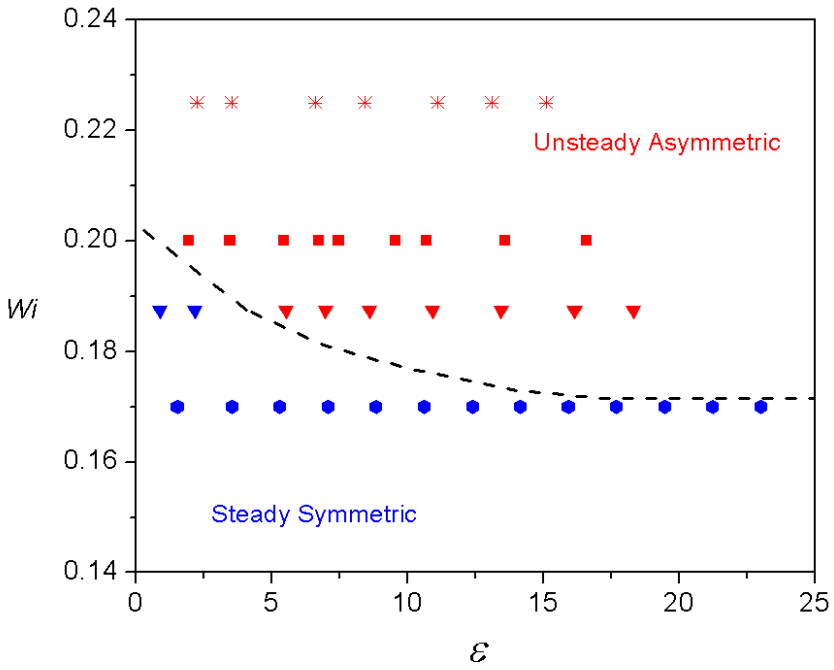

Figure 6.17: Stability diagram for the FENE-CD-JS model ($L^2 = 100$)

For the FENE-CD-JS fluid, stability diagrams are shown for the parameters $L^2 = 50$ (Fig. 6.16) and $L^2 = 100$ (Fig. 6.17). In these simulations, flow transition from steady symmetric to steady asymmetric occurs at $Wi_{cr} \approx 0.27$ and $Wi_{cr} \approx 0.17$, respectively. In comparison to the previous models, the steady asymmetric flow regime for FENE-CD-JS ($L^2 = 50$) spans a much smaller range of Wi, indicating greater tendency towards time-dependent behaviour. For this fluid, supercritical flow transition to time-dependent flow occurs at $Wi \approx 0.31$. For the FENE-CD-JS ($L^2 = 100$) fluid, the steady asymmetric flow regime vanishes completely and the flow goes directly from being steady symmetric to unsteady asymmetric without settling down in time in the asymmetric regime. This behaviour of the FENE-CD-JS model is due to the rapid increase in the strain experienced by the fluid because of the much greater stresses generated by the drastic increase in extension compared with the other models as seen in Section 6.3.

The results show that the FENE-CD-JS fluid is much more unstable compared with the other models. This behaviour is governed by the value of the set of parameters L and κ. The combination of these two parameters determines the maximum level of stretch of the dumbbells, which as we have noted before, is a critical process that drives the flow unstable. Comparing the results of the three models for the extensibility parameter,

$L^2 = 100$, illustrates the effect of non-linear drag on the FENE-CD-JS model. As depicted by Fig. 6.1, the steady state profiles of the extensional viscosities of these models are not significantly different in the simple homogeneous flow, yet the effect of the non-linear drag in the transient flow can be very much. It is obvious that the steady state properties of these models are not as important as their behaviour in time-dependent flows because the rheological behaviour of the dumbbell model is determined by the time-dependent evolution of their microstructure which is coupled with the macroscopic flow field.

6.5 Dumbbell Extension

Further understanding of the behaviour of the dumbbell model can be gained by studying the evolution of the dumbbell extension, $\mathrm{tr}(\boldsymbol{A})$, with time, t/λ, shown in Fig. 6.18. The figure compares the results for FENE-CR model and FENE-CD-JS for the same extensibility parameter $L^2 = 100$. The fluids exhibit similar degree of stretch but show very different time-dependent behaviour. In the FENE-CR model, the flow assumes one asymmetric configuration for the duration of time investigated. There are regions of localised stretching around the outflow symmetry axis and close to the channel walls. For this model, initially, the dumbbell extension is large around the outflow symmetry axis but reduces in magnitude after the flow becomes asymmetric, dropping to about the same magnitude as the wall stretching. In the FENE-CD-JS model, the direction of asymmetry tilts between the two outlet channels with time and the dumbbell extension is more localised around the outflow symmetry axis. As time increases, $\mathrm{tr}(\boldsymbol{A})$ increases in magnitude and becomes increasingly localised in this region, whereas its value along the wall in the inlet channels diminishes in contrast to the behaviour of the FENE-CR model.

Corresponding profiles of the first normal stress difference, $N_1 = \tau_{xx} - \tau_{yy}$, normalised by $2\eta U/d$, for the two models are plotted along the inlet line of symmetry in Figs. 6.19 and 6.20. The negative values of the first normal stress indicate the compressive nature of the stresses in the region. As depicted by the contour plot of $\mathrm{tr}(\boldsymbol{A})$ in Fig. 6.18, the first normal stress for FENE-CR decreases in magnitude in the region of the stagnation point and becomes broader with time, whereas for FENE-CD-JS, the first normal stress

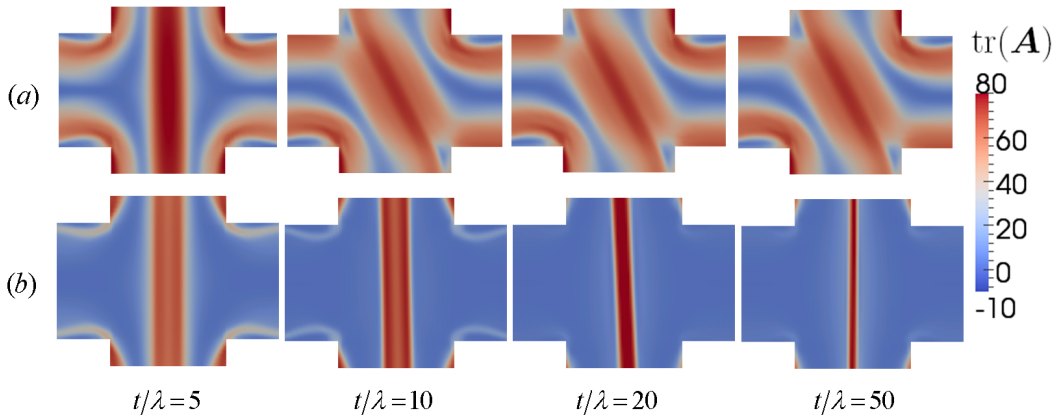

Figure 6.18: Comparing polymer extension tr($\boldsymbol{A}$) for (a) the FENE-CR model ($L^2 = 100$) at $Wi = 2.39$ and (b) the FENE-CD-JS model ($L^2 = 100$) at $Wi = 0.22$

increases in magnitude and become narrower in this region.

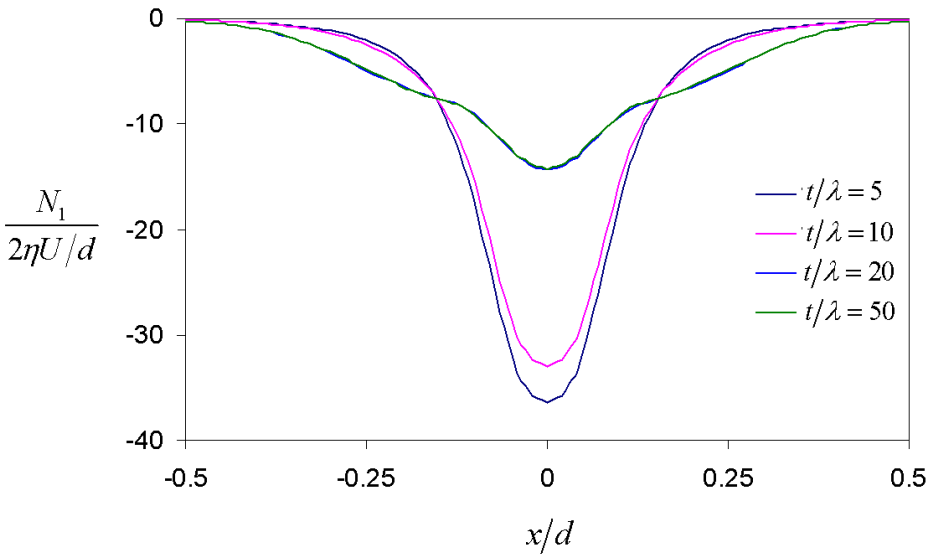

Figure 6.19: Profiles of the normalised first normal stress difference along the symmetry line of the inlet channel for the FENE-CR model ($L^2 = 100$) at $Wi = 2.39$

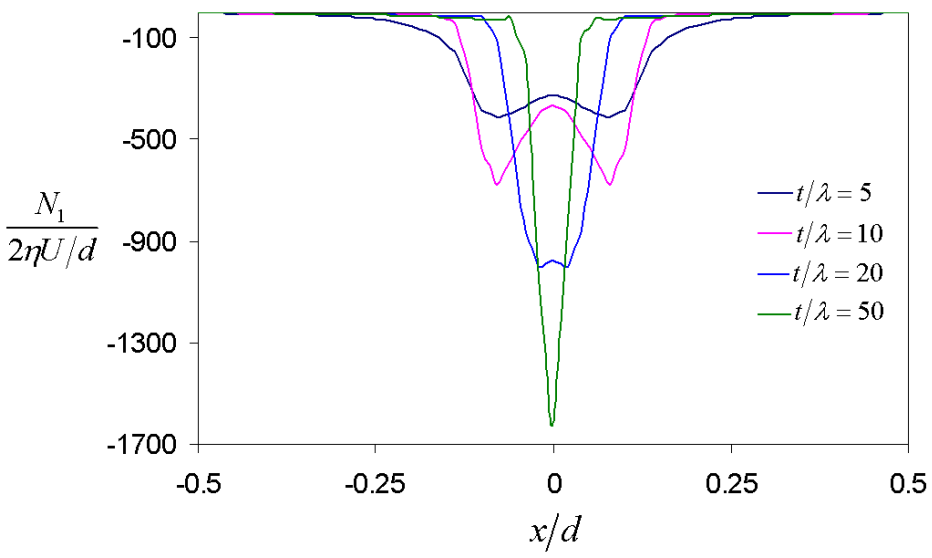

Figure 6.20: Profiles of the normalised first normal stress difference along the symmetry line of the inlet channel for the FENE-CD-JS model ($L^2 = 100$) at $Wi = 0.22$

The distinction in the behaviour of the these two models, which are differentiated only by Larson's hydrodynamic friction law, is very intriguing and shows how polymer molecules may behave under different levels of extensional stress generated in the cross-slot flow. Different stress-relief mechanisms are adopted by the models, which result in their unique time-dependent behaviour. For the FENE-CR model, it appears to be more energetically favourable to "disperse" the stress away from the stagnation point by adopting a strong asymmetric flow configuration. For FENE-CD-JS, a much higher stress is generated at the start of the flow and it is more energetically favourable for the flow to localise the stress in this region. It is also noticeable at the start-up ($t/\lambda = 5$) of the flow that the extension developed along the symmetry axis for FENE-CD-JS is much greater than that generated along the walls of the inlet channel in comparison to the FENE-CR model.

6.6 Conclusions

In this chapter, the network-theory-based Phan-Thien Tanner model and the FENE dumbbell models have been evaluated in the cross-slot. The model parameters were

selected for matching peak extensional viscosities in simple homogeneous flow. Using the Larson friction law, the distinction between the steady-state extensional viscosities of the constant drag and non-linear drag models is barely noticeable, yet dramatic differences in their rheological behaviour are found in the cross-slot flow. Time-dependent stability diagram were constructed based on the Weissenberg number of the flow and the strain at the stagnation point to study the transient behaviour of the fluids. In the diagrams, three distinct flow regimes were delineated, namely, steady symmetric flow, steady asymmetric flow, and unsteady asymmetric flow. A new flow transition is identified in which the flow goes directly from steady symmetric to unsteady asymmetric flow without passing through the steady asymmetric regime. The Wi for supercritical flow transition decreases with the non-linear character of the constitutive models. For the non-linear friction FENE-dumbbell model, the constitutive instability is associated with the parameters, κ, the non-linear friction coefficient and, L, the finite extensible length of the dumbbell. The non-linear character of the model increases as these parameters are increased.

These results illustrate the effect of non-linear dynamics of the polymer chain. Even for a friction law as weak as Larson's such dramatic differences in the dynamics of the fluids are predicted. This shows that the physical mechanism by which the flow evolves with polymer conformation can significantly modify the behaviour of the model because of the resulting higher extensional stress. Understanding such instability phenomena in the cross-slot may have significant implications on industrial processes in which flow instability is a common problem. This is of often encountered in applications in which highly stretching flows are generated, such as draw resonance and filament breaking instabilities in fibre spinning, which seriously affect the production rate in polymer processing [133].

Chapter 7

Elastic Instability in Contraction Flows

7.1 Introduction

Entry flows have been used for many years as a benchmark flow problem to validate numerical simulation, yet the success of simulation in predicting non-linear phenomena in this geometry has been limited. For a Newtonian fluid, the presence of the inertial term in the Navier-Stokes equation introduces non-linearity, which poses a difficulty to numerical simulations. Significant vortex activities are only observed for this fluid in the sudden expansion geometry, which is caused by the influence of inertia [134, 135]. However, in the sudden contraction flow, its behaviour is less interesting and only a Moffatt vortex is usually observed. Viscoelastic flows in sudden contractions is by far more intriguing [16, 136, 137, 138], but in the expansion flow it is found that viscoelasticity tends to suppress the vortex growth, which is evidence of the stabilising effect of elasticity on inertial flow [139]. So far, numerical simulation has predicted inertial instability for Newtonian fluids in sudden expansion flows but numerical simulations of elastic instability in contraction flows have not been previously reported.

Experimental evidence in microfluidic contraction flow [16, 138] shows rich vortex behaviour for polymer solutions in the low to moderate Reynolds number, Re, and the high Weissenberg number, Wi, flow regime. In this flow regime, elastic instability may be generated and has been observed across a range of elasticity numbers, El. In low El

flows, a Newtonian-like flow is usually observed at low Wi, which goes through several flow transitions into a symmetric time-dependent vortex growth and an asymmetric bistable vortex growth at moderate Wi, and to a divergent flow regime showing very large vortices at very high Wi [16, 82, 83, 84, 85]. In the high El flow regime, lip vortices appear at low Wi and grow into larger asymmetric dynamic vortex patterns at high Wi. The flow in this type of geometry is strongly three-dimensional by virtue of their small aspect ratios, which has a strong contribution to the observed flow patterns. The influence of the aspect ratio in three-dimensional viscoelastic flow will be discussed in Chapter 8. However, in this chapter only 2-D flows will be studied.

The transition in vortex patterns can be correlated to the dimensionless pressure drop, $\triangle\mathcal{P}$, across the channel and mapped out on the plot of Wi vs $\triangle\mathcal{P}$ [138]. This excess pressure drop experienced by polymeric fluids in the converging flow has long been suggested as a standard measure for viscoelastic flow simulation in the 4:1 contraction benchmark flow problem [140]. Experimental [136] and numerical [127] investigations have shown that the excess pressure drop is associated with an additional polymer dissipative stress on an extended polymer chain due to a strong coupling of the chain with the applied macroscopic flow field. Recent numerical studies of elastic instability in cross-slot flow suggest that the onset of flow instability may be a physical mechanism by which energy is removed from the flow, which might result in a reduction in the excess pressure drop [129].

In this chapter, simulations of elastic instability in contraction flows are reported for the first time. Time-dependent finite-volume calculations are implemented as described in Chapter 4. Thus, the numerical simulation imitates the physics of viscoelastic flows more realistically unlike steady-state simulations which often uses under-relaxation technique to evolve the solution, in which the solution does not follow the trajectory of the non-linear flow to reach the final steady-state solution.

Firstly, in Section 7.2, the prediction of the models in simple homogeneous flows and in the contraction flow is discussed with a view to discriminating between the models. In Section 7.3, the simulations presented are conducted without the effect of inertia by neglecting the inertial term in the momentum equation. In Section 7.4, the inertial term is included in the momentum equation in order to characterise the flow based on the

elasticity number. The influence of the inertial term and the contraction ratio will be studied.

7.2 Model Prediction

The present study will be conducted using the model parameters depicted by the material functions shown in Fig. 7.1. To investigate the effect of conformation-dependent drag for the FENE-CD-JS model, the value of the hydrodynamic drag coefficient, κ, is varied for a fixed extensibility parameter, $L^2 = 100$. These plots show increasing elongational viscosity with κ. Matching rheological fluids are sought through peak extensional viscosity for the FENE-CD-JS model ($\kappa = 0.1$,$L^2 = 100$) with non-linear friction coefficient, the constant friction FENE-CD-JS model ($\kappa = 0$,$L^2 = 160$), and the L-PTT model ($\epsilon = 0.006$) to investigate the effect of the constitutive model. For all the fluids represented by the various plots, their shear viscosities are reasonably close for the selected shear-thinning parameter, $\xi = 0.075$. This value is necessary in order to stabilise the numerical solution up to a level of Wi that is significantly higher than would be attained for a vanishing value of ξ. The stabilising effect of shear-thinning is more effective when the inertial term is taken into consideration in the momentum equation.

In Fig. 7.2, the transient data of the homogeneous flow elongational viscosity for L-PTT ($\epsilon = 0.006$), FENE-CD-JS ($\kappa = 0, L^2 = 160$), and FENE-CD-JS ($\kappa = 0.1, L^2 = 100$) is plotted in order to compare the dynamic behaviour of the fluids at two arbitrary Weissenberg numbers, $Wi = 0.5$ and 25. Note that the steady-state values of the data can be deduced from Fig. 7.1. At the value $Wi = 0.5$, a large discrepancy is already noticeable in the evolution of the elongational viscosity of the models, with the variable drag model predicting the largest elongational viscosity. For $Wi = 25$, the discrepancy between the models is much greater. The elongational viscosity of the L-PTT model rises much more slowly compared with the FENE dumbbell model. The FENE dumbbell model also predicts overshoots in the elongational viscosity, which are often seen during start-up of viscometric flows.

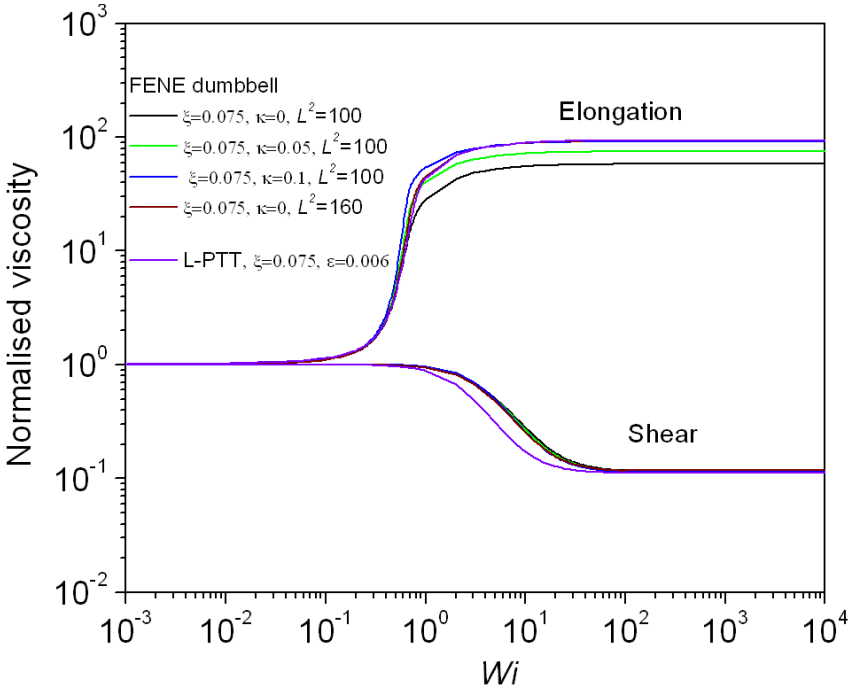

Figure 7.1: Prediction of shear and elongational viscosities for the FENE dumbbell model with constant and non-linear friction coefficient, and for the L-PTT model in homogeneous flow

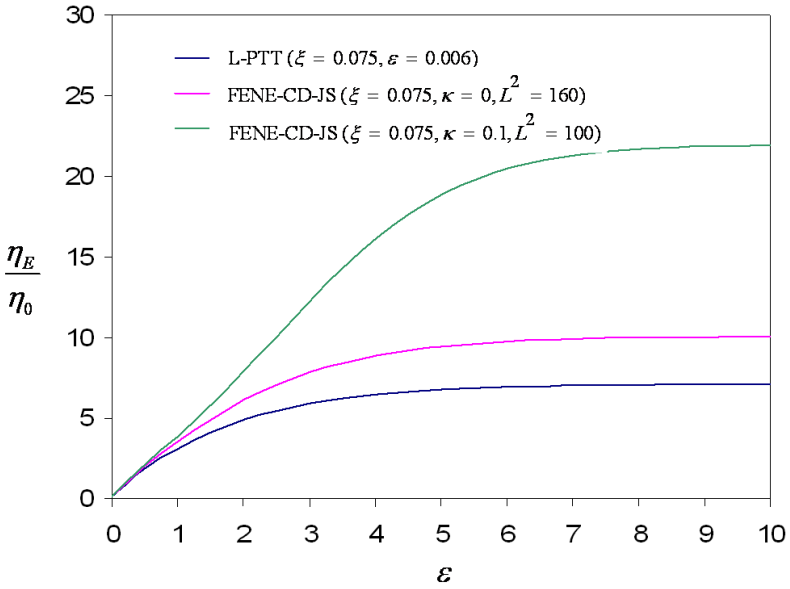

Figure 7.2: Plot of transient elongational viscosity, η_E, normalised by η_0, at $Wi = 0.5$ for L-PTT and FENE-CD-JS

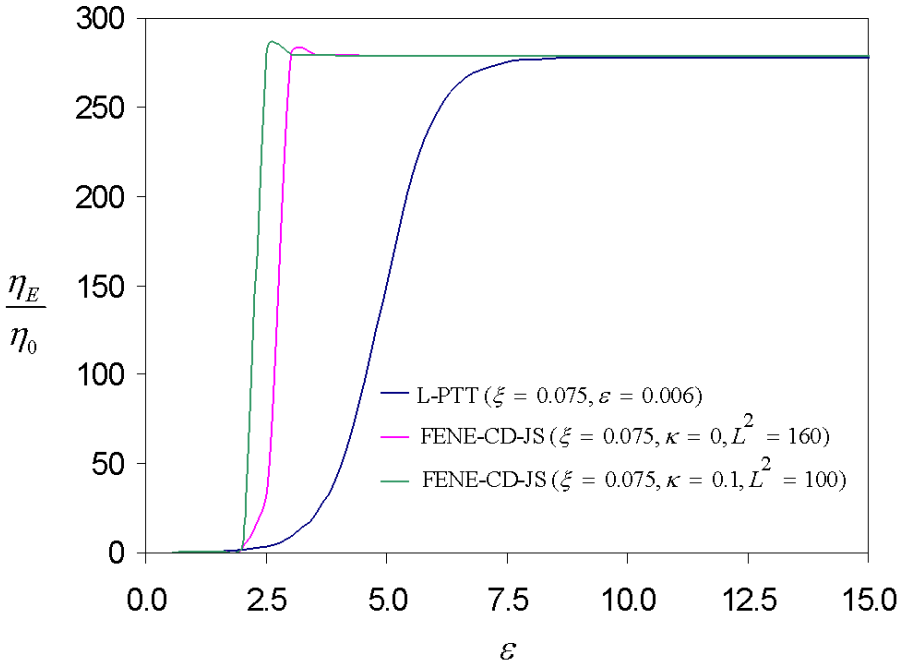

Figure 7.3: Plot of transient elongational viscosity, η_E, normalised by η_0, at $Wi = 25$ for L-PTT and FENE-CD-JS.

7.3 Purely Elastic Flow

7.3.1 Geometry and Mesh

In line with recent experiments [16], the study will be conducted using a 16:1 contraction geometry. In order to validate solution convergence with mesh refinement, numerical simulations have been performed using two meshes M1 and M2 as shown in Fig. 7.4. The number of control volumes are 42,520 and 83,700 and their minimum dimensions are given by $\triangle x_{min}/w_c = \triangle y_{min}/w_c = 0.014$ and 0.01 for M1 and M2, respectively. The lengths of the upstream and downstream channels are 300 and 200 widths of the downstream channel, w_c, respectively, to allow for complete flow development along the channels. The simulations presented were performed using the following boundary conditions. At the inlet boundary a Dirichlet condition is applied for the velocities, the stress is set to zero, and a homogeneous Neumann condition is applied for the pressure field. A homogeneous Neumann condition is prescribed for the velocity and stress fields at the outlet boundary, while a vanishing pressure is prescribed at the outlet boundary. A no-slip condition is prescribed along the walls.

Fig. 7.5 and 7.6 show plots of instantaneous profiles of the normalised streamwise velocity, v_x, and the normalised first normals stress difference, N_1, along the centreline of the contraction at $Wi = 4$. The simulations were performed using the variable drag FENE-CD-JS model ($\xi = 0.075, \kappa = 0.1, L^2 = 100$). The time, t, of the flow process is normalised by the relaxation time, λ, of the fluid. In these results, the profiles are almost indistinguishable at the same instance in time $t/\lambda = 1$, 40, and 125, which suggests that the evolution of the solutions is not dependent on the mesh. Noticeably, there is a significant growth in the velocity and stress fields between $t/\lambda = 1$ and 40 because of the start-up flow period. After the flow reaches this state, the changes in the flow field in the upstream channel far from the entry region is very small relative to the fluctuations in the vicinity of the re-entrant corner. Downstream of the re-entrant corner, significant dynamic behaviour takes place up to a channel length equal to approximately 30 widths of the downstream channel. The simulation results show that the flow remains time-dependent for a long period of time. No steady-state solution was reached.

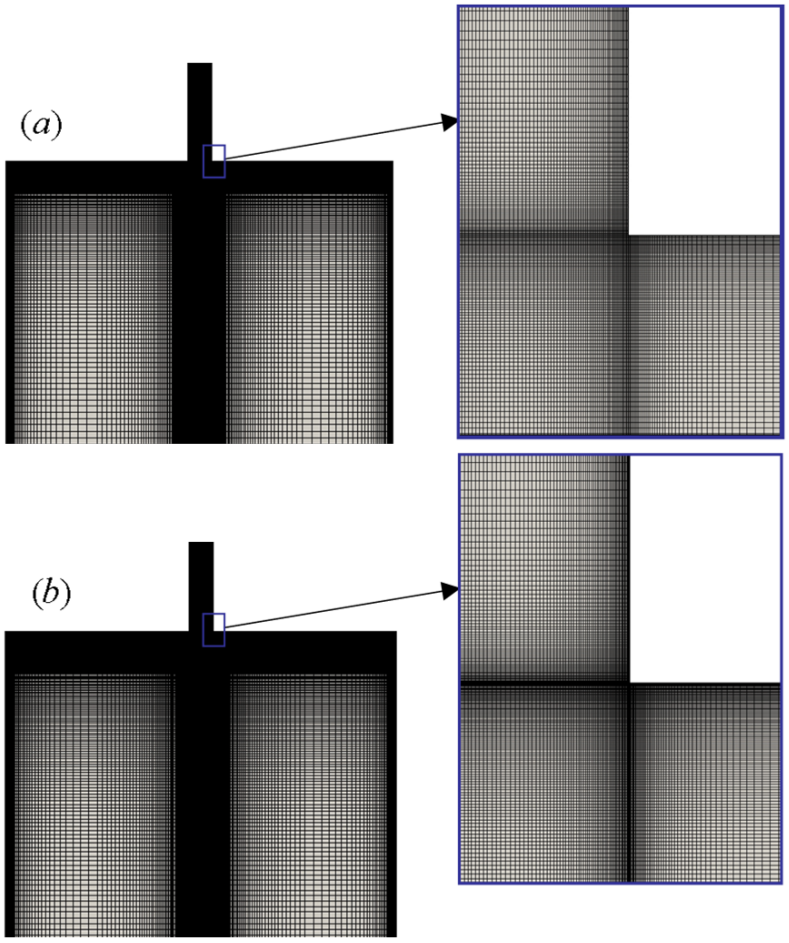

Figure 7.4: Computational geometry and grid for 16:1 2-D planar contraction showing mesh refinement around the re-entrant corner for (a) M1 (b) M2

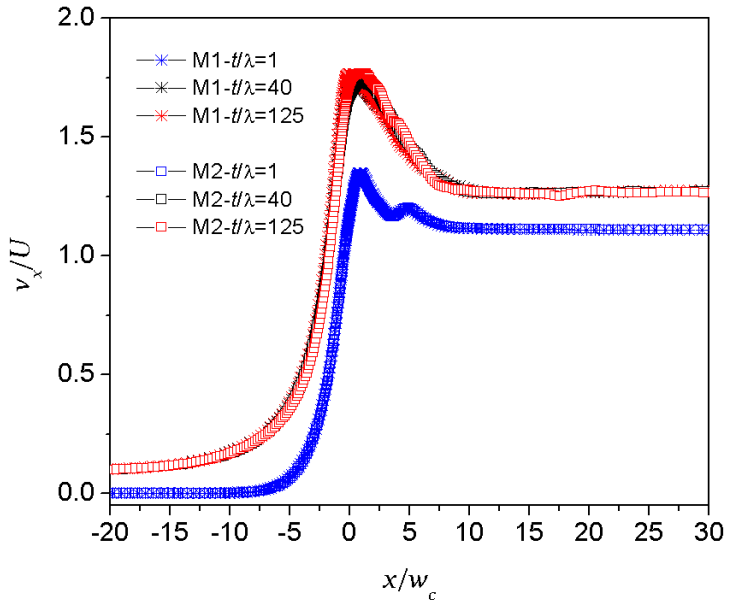

Figure 7.5: Instantaneous profile of streamwise velocity, v_x, along the centrline of the geometry, normalised by the mean velocity, U, in the downstream channel. The results are based on the FENE-CD-JS model at $Wi = 4$

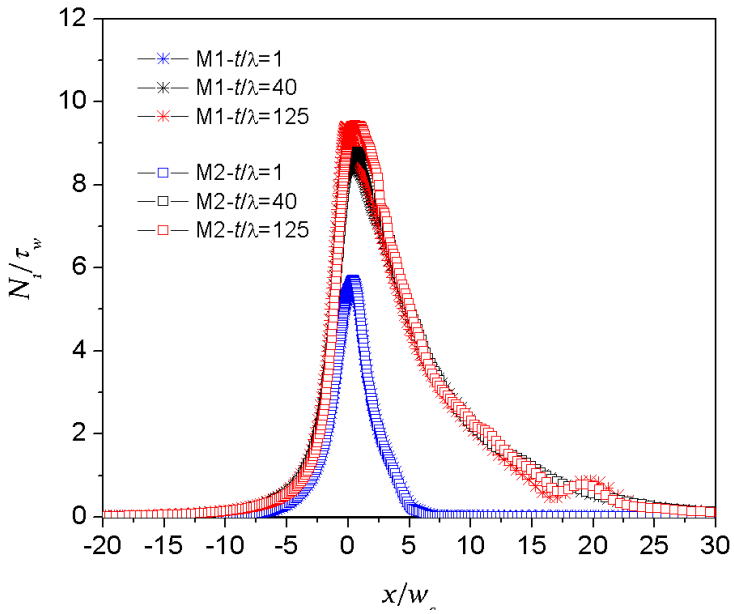

Figure 7.6: Instantaneous profile of the first normal stress difference, N_1, along the centre-line of the geometry, normalised by the wall shear stress, τ_w, in the downstream channel. The results are based on the FENE-CD-JS model at $Wi = 4$

7.3.2 Effect of Constitutive Models

The effect of the constitutive model is investigated using L-PTT ($\epsilon = 0.006$), FENE-CD-JS ($\kappa = 0, L^2 = 160$), and FENE-CD-JS ($\kappa = 0.1, L^2 = 100$), which have been shown in Section 7.2 to exhibit similar steady elongational viscosities but differ significantly in the transient flow.

The flow pattern for the fluids are shown in Fig. 7.7-7.9 for increasing Wi. For the three fluids, a Newtonian-like flow is obtained at the low Wi value of 0.5, which is characterised by a Moffatt-like corner vortex. Over the range of the Wi examined, the vortex pattern of the L-PTT model remains fairly steady. The vortex pattern of the constant drag FENE-CD-JS model in Fig. 7.8 is also fairly steady at low Wi, but as Wi is increased the flow becomes unsteady and slightly asymmetric around the lip region. This is more clearly seen in the snapshots of the streamlines shown in Fig. 7.11, in which the vortex has become slightly asymmetric in the re-entrant corner at $t/\lambda = 32$. A more dramatic time-dependent flow pattern is seen for the FENE-CD-JS ($\kappa = 0.1, L^2 = 100$) model. At $Wi = 3$ (Fig. 7.9) this fluid has become significantly asymmetric with one corner vortex becoming much larger than the other, having merged with the lip vortex. At the higher Wi value of 5, the vortices have grown larger and the asymmetry is more pronounced.

The snapshots of the vortex patterns shown in Fig. 7.10-7.12 for $Wi = 5$ show that vortex growth takes place initially by a lip mechanism in the FENE-CD-JS ($\kappa = 0.1, L^2 = 100$), which then grows and merges with the corner vortex. The lip vortex mechanism becomes increasingly dominating with fluid type. Comparing the three models at $t/\lambda = 4$, the size of the lip vortices are largest in the FENE-CD-JS ($\kappa = 0.1, L^2 = 100$) model and smallest for the L-PTT model. The results of the image sequence captured in Fig. 7.12 also show that the size of the corner vortices fluctuates non-periodically in the FENE-CD-JS ($\kappa = 0.1, L^2 = 100$) model causing the asymmetric pattern to flip from corner-to-corner while the flow remains unsteady.

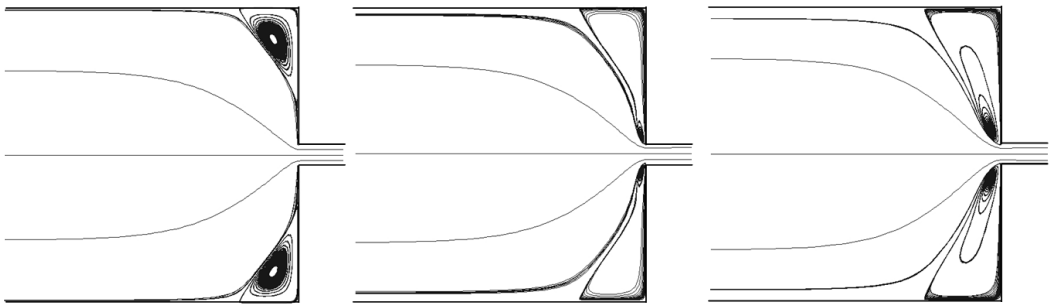

Figure 7.7: Streamlines for L-PTT showing the effect of increasing Wi on the flow pattern ($t/\lambda = 226$) (a) $Wi = 0.5$ (b) $Wi = 3$ (c) $Wi = 5$

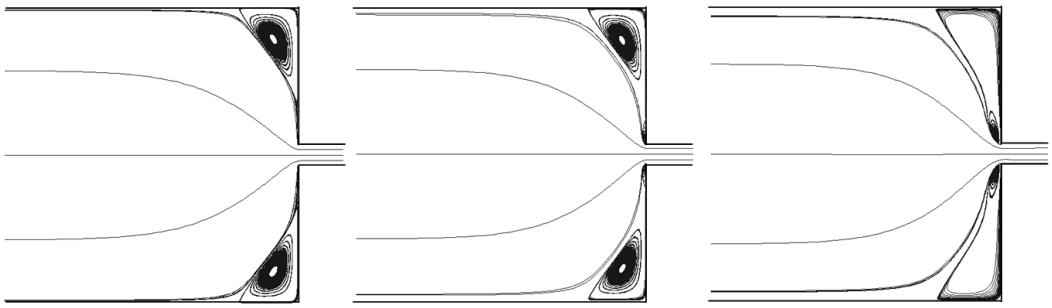

Figure 7.8: Streamlines for FENE-CD-JS ($\kappa = 0, L^2 = 160$) showing the effect of increasing Wi on the flow pattern ($t/\lambda = 206$) (a) $Wi = 0.5$ (b) $Wi = 3$ (c) $Wi = 5$

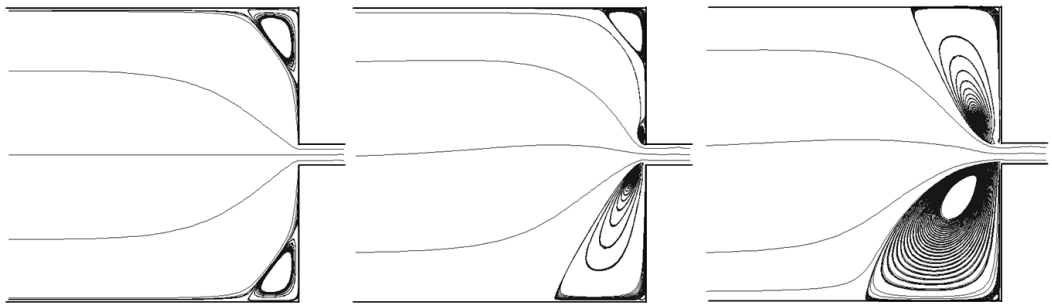

Figure 7.9: Streamlines for FENE-CD-JS ($\kappa = 0.1, L^2 = 100$) showing the effect of increasing Wi on the flow pattern ($t/\lambda = 110$) (a) $Wi = 0.5$ (b) $Wi = 3$ (c) $Wi = 5$

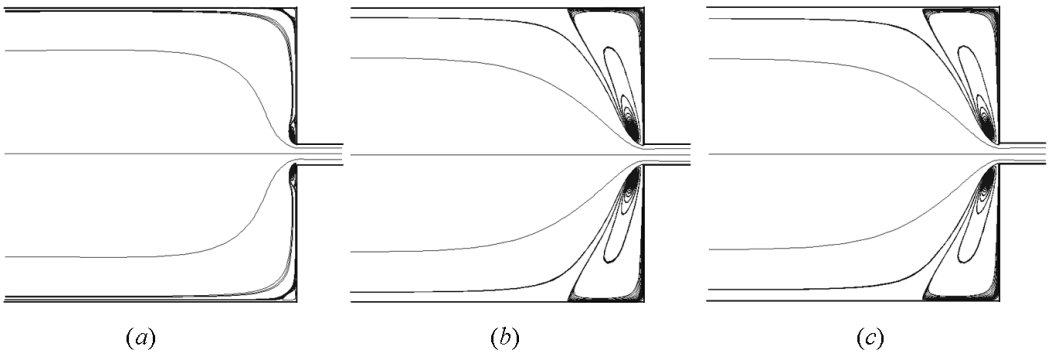

Figure 7.10: Snapshots of streamlines for L-PTT at $Wi = 5$ (a) $t/\lambda = 4$ (b) $t/\lambda = 32$ (c) $t/\lambda = 226$

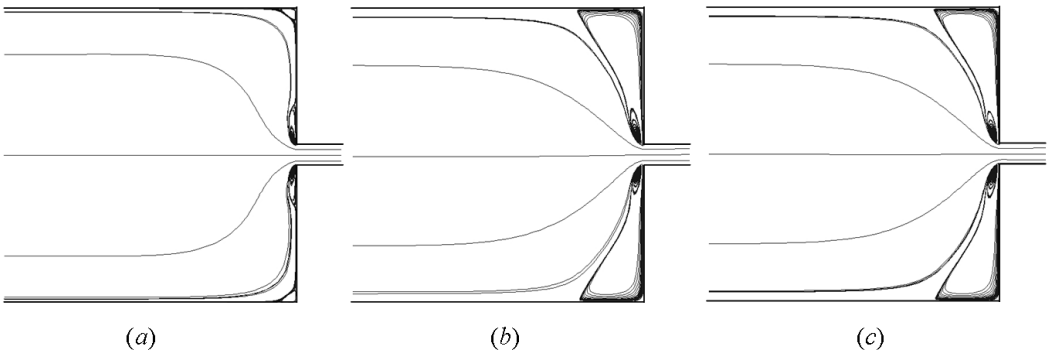

Figure 7.11: Snapshots of streamlines for FENE-CD-JS ($\kappa = 0, L^2 = 160$) at $Wi = 5$ (a) $t/\lambda = 4$ (b) $t/\lambda = 32$ (c) $t/\lambda = 204$

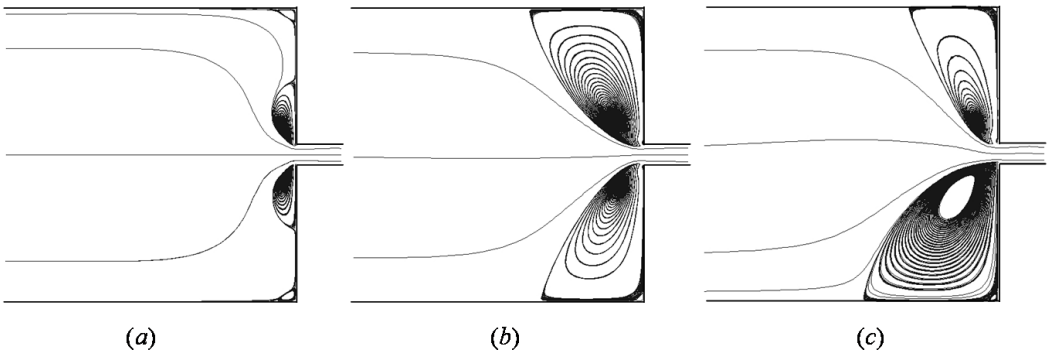

Figure 7.12: Snapshots of streamlines for FENE-CD-JS ($\kappa = 0.1, L^2 = 100$) at $Wi = 5$ (a) $t/\lambda = 4$ (b) $t/\lambda = 79$ (c) $t/\lambda = 110$

The vortex pattern predicted by the FENE-CD-JS ($\kappa = 0.1, L^2 = 100$) model behaves similarly to those observed in microfluidic experiments in the high El flow regime ($El \approx 89$) using a 16:1 contraction ratio [16]. However, there is a notable difference between the predicted flow patterns and the experiment. Much stronger recirculating three-dimensional patterns are observed in the experiment due to the small aspect ratio, AR, (i.e. ratio of the channel width to its depth) of the flow device, which are in the range of 0.05 and 0.5 for the upstream and downstream sections, respectively. This is expected to have a strong influence on the flow patterns, whereas the present simulations are two-dimensional. In three-dimensional contraction flows with such small aspect ratios, the effect of the confining walls is to increase the strain on the fluid leading to much stronger recirculating patterns even for a Newtonian fluid [134].

Elastically-induced asymmetric behaviour of dilute polymer solutions is a characteristic of the high El flow regime because of the dominating influence of the fluid elasticity. Neglecting inertia in the present simulations implies that $El \to \infty$. In experiments, such phenomenon has been reported at El of the orders of 500 [85].

Fig. 7.13 compares the profiles of the first normal stress difference, N_1, along the centreline of the contraction for the three fluids. N_1 is normalised by the wall shear stress, τ_w, which is calculated for a fully developed flow in the downstream channel. As shown, the profiles for L-PTT and FENE-CD-JS ($\kappa = 0, L^2 = 160$) are almost identical, which indicates similar range of extensional stresses in the fluid. By contrast, for the FENE-CD-JS ($\kappa = 0.1, L^2 = 100$) fluid, a much greater N_1 is predicted. The value of N_1 is greatest in the vicinity of the re-entrant corner because the fluid in this region is subject to a very high strain, which persists a long way down the downstream channel. Far upstream and downstream of the re-entrant corner the fluid is relaxed and all three models predict identical N_1.

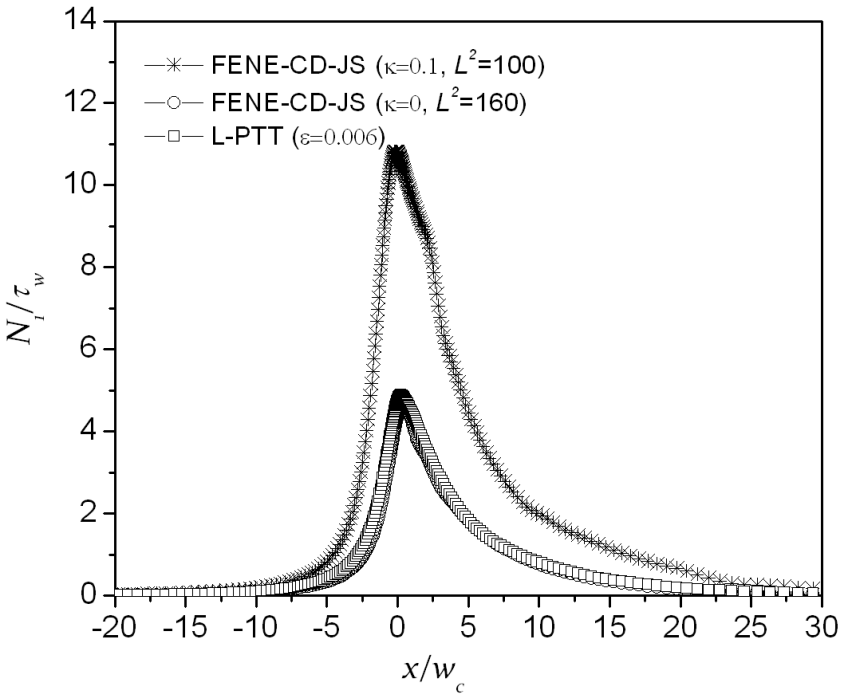

Figure 7.13: Profiles of the first normal stress difference, N_1, along the centreline normalised by the wall shear stress, τ_w, in the downstream channel

The effect of the hydrodynamic drag coefficient is illustrated by reducing the parameter, κ, to 0.05 for the FENE-CD-JS model. The simulation results presented in Fig. 7.14 show that the model also predicts asymmetric flow patterns but generally smaller vortices. At $Wi = 3$ small asymmetric lip vortices can be seen as well as standing corner vortices which appear to be symmetric, in contrast to the asymmetric vortices shown at this Wi for the higher drag model. At $Wi = 5$ large asymmetric vortices are also predicted. Snapshots of the streamlines for this model are presented in Fig. 7.15, which show a similar behaviour as the higher drag model. The vortex dynamics is also dominated by a lip vortex mechanism and the vortices evolve from the re-entrant corners and grow larger in size with time.

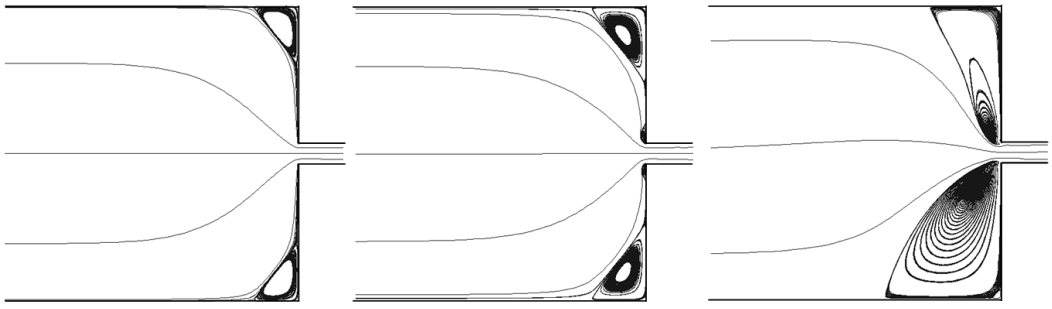

Figure 7.14: Streamlines for FENE-CD-JS ($\kappa = 0.05, L^2 = 100$) showing the effect of increasing Wi on the flow pattern ($t/\lambda = 97$) (a) $Wi = 0.5$ (b) $Wi = 3$ (c) $Wi = 5$

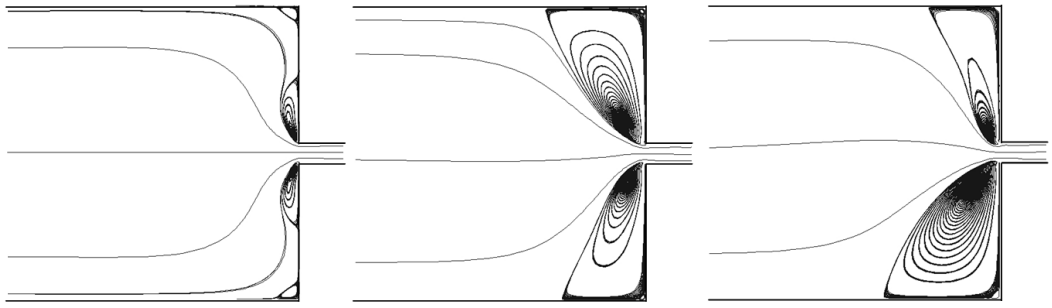

Figure 7.15: Snapshots of streamlines for FENE-CD-JS ($\kappa = 0.05, L^2 = 100$) at $Wi = 5$ (a) $t/\lambda = 4$ (b) $t/\lambda = 71$ (c) $t/\lambda = 97$

7.4 Finite Elasticity Number Flow

In this section, the inertial term in the momentum equation will be included and the effect of the contraction ratio on the asymmetric flow patterns will be investigated. Simulations are conducted using the FENE-CD-JS ($\kappa = 0.01, L^2 = 100$) model for different contraction ratios. Firstly, the effect of the inertial term on the flow patterns will be discussed based on the 16:1 contraction ratio. Snapshots of the flow patterns for this geometry with and without the influence of inertia are compared in Fig. 7.16 and 7.17. For these simulations $Re \approx 0.0278$ and $Wi = 5$, which gives $El \approx 180$, therefore elasticity is expected to dominate in this flow regime. The results show that between $t/\lambda = 4$ and 32 a much smaller lip vortex and a smaller corner vortex are predicted in the non-vanishing Re flow. Following the image sequence captured in the figure, it may be seen that for the purely elastic flow ($El \to \infty$), the top wall vortex develops to become greater in size than the bottom wall vortex with time. The influence of inertia seems to have an opposing effect on this trend.

In order to study the evolution of the vortex with time, a bifurcation parameter, DX, will be defined as proposed by [141], which is given in terms of the distance between the vortex reattachment points on the upper and lower walls, $DX = (\mathcal{L}_U - \mathcal{L}_D)/(\mathcal{L}_U + \mathcal{L}_D)$, where $\mathcal{L}_U$ and $\mathcal{L}_D$ are the sizes of the vortex on the upper and lower walls, respectively. Therefore, for a symmetric vortex growth, $DX = 0$, and otherwise it implies a transition from a symmetric to an asymmetric vortex growth. For $DX > 0$ the top wall vortex is larger and for $DX < 0$ the bottom wall vortex is larger.

The evolution of DX with the normalised time, t/λ, is shown in Fig. 7.18. At the start of the flow $DX = 0$ for both the inertial and inertialess flow. The transition from symmetric to asymmetric flow takes place at $t/\lambda \approx 15$ in the inertialess flow and at $t/\lambda \approx 19$ with inertial effect. Comparing the oscillatory behaviour of the DX for the flows suggests that the inertialess flow appears to be more stable and displays stronger deviation from symmetric behaviour compared with the inertial flow. The inertial flow fluctuates with a shorter period of about 50 times the relaxation time of the fluid. The result suggests that the elastically-induced asymmetric flow pattern is stabilised by the elasticity number, whereas inertia has an opposing effect on the flow pattern, which is

supported by experimental evidence [16].

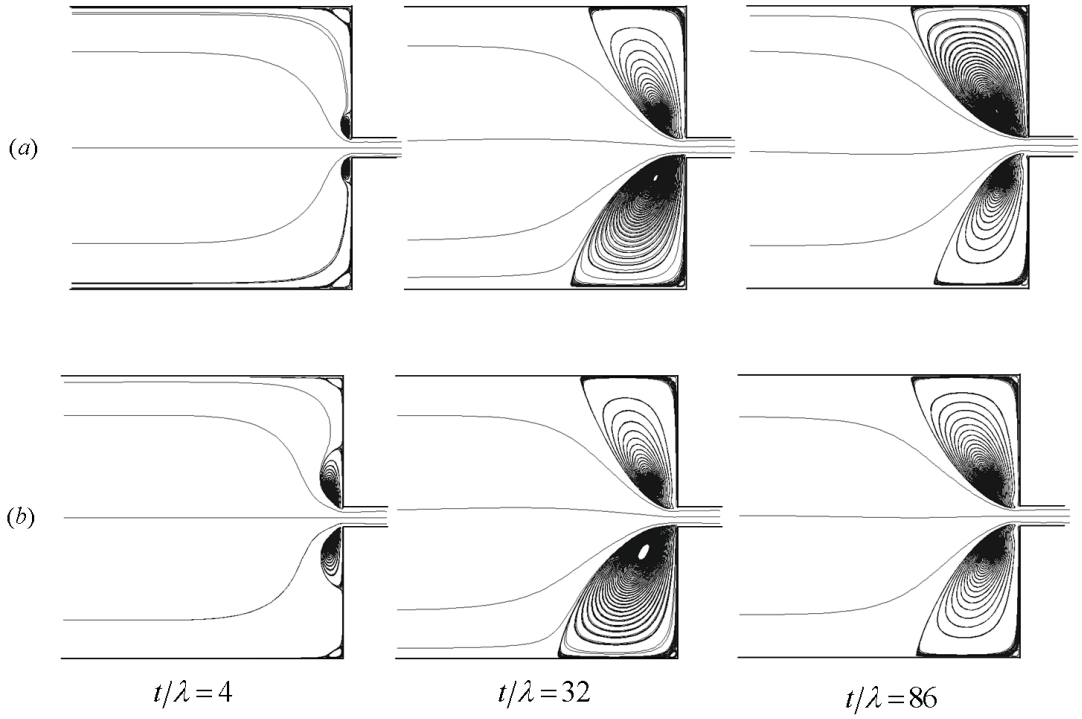

Figure 7.16: Snapshots of streamlines for FENE-CD-JS ($\kappa = 0.1, L^2 = 100$) at $Wi = 5$ (a) with inertial effect ($Re = 0.0278$) (b) without inertial effect ($Re = 0$)

The results reported so far are consistent with experimental observations for the 16:1 contraction flow. It should be noted that although the experiments were performed using a contraction-expansion geometry, the contraction throat of the experimental geometry is long enough for the effect of the expansion section to be neglected. As shown by the profile of the first normal stress difference in Fig. 7.13, the fluid is fully relaxed at about 30 widths of the downstream section. The unstable flow behaviour of polymer solutions in this geometry largely originates in the region of high strain during the converging flow in the re-entrant corner, as depicted by the high first normal stress difference in this region. For a relatively short re-entry length in the contraction-expansion flow, it is expected that the upstream flow pattern would be influenced by the inertial effect that may arise in the expansion section further downstream. As discussed in the introduction, viscoelasticity usually has a quelling effect on the downstream flow pattern in sudden expansion flows, and disturbances propagating from the upstream and downstream channels might act to

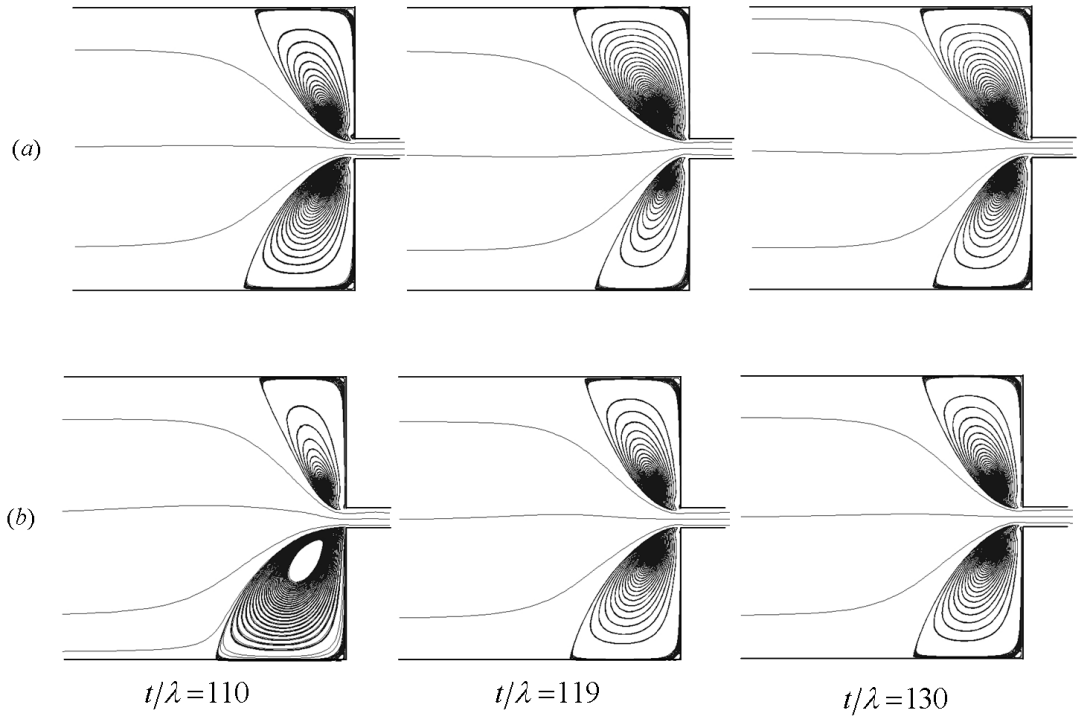

Figure 7.17: Snapshots of streamlines for FENE-CD-JS ($\kappa = 0.1, L^2 = 100$) at $Wi = 5$ (a) with inertial effect ($Re = 0.0278$) (b) without inertial effect ($Re = 0$)

effectively cancel out each other. It will be interesting to investigate the effect of the re-entry length in such a geometry. Other geometric parameters which may also greatly influence the flow patterns in this geometry are the contraction ratio and the aspect ratio.

Bearing in mind the effect of the contraction ratio on the flow patterns in the contraction flow, it is desirable to construct a general stability diagram that can account for the effect of the contraction ratio. Such a stability diagram will be very useful for illustrating the various flow regimes achievable in contraction flows regardless of the contraction ratio, at least for a simple case such as a 2-D flow without a diverging flow section. In the discussions following, the effect of the contraction ratio will be investigated using contraction ratios of 4, 8 and 16. The geometries are designed by varying the upstream width of the channels for a fixed downstream width for the three channels. Based on the conventional definition of the elasticity number, $El = Wi/Re$, for a given fluid, El will be fixed for the three channels, and on a $Wi - Re$ diagram the flows will be represented by the same trajectory, i.e. $El \approx 180$ in this case. However, the flow patterns due to the

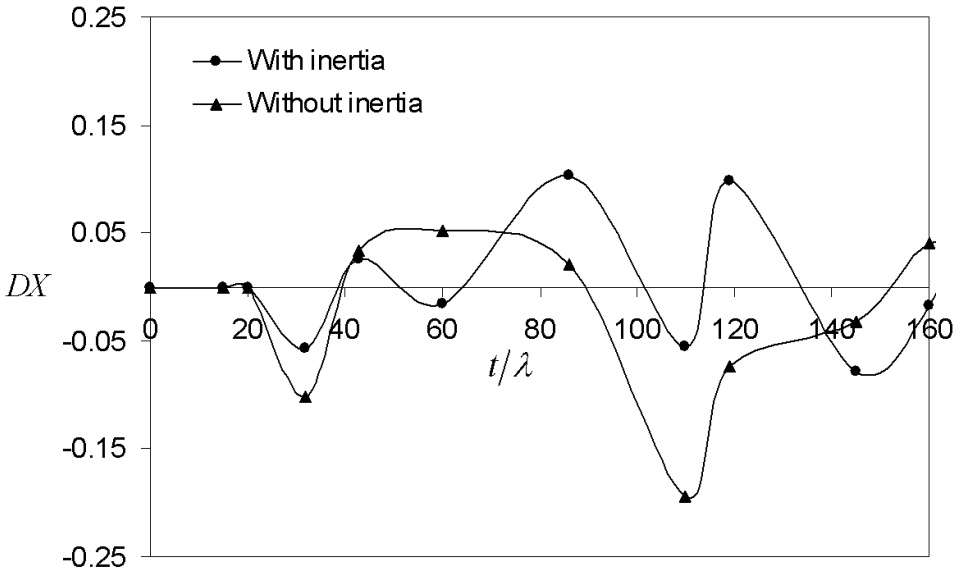

Figure 7.18: DX diagram for the FENE-CD-JS ($\kappa = 0.1, L^2 = 100$) model comparing the transient behaviour of the vortex pattern with and without effect of inertia

different contraction ratios are expected to be significantly different since the fluid will experience different total Hencky strains given by the logarithm of the contraction ratio, $\varepsilon_H = \ln(w_u/w_c)$. Hence, a stability diagram constructed based on $Wi - Re$ alone may not be sufficient to describe the flow in the contraction geometry. To include the effect of the contraction ratio, the dimensionless parameter $El^\beta = \beta Wi/Re$ will be defined, where $\beta = w_u/w_c$ is the contraction ratio of the geometry. El^β may also be written in terms of the Hencky strain, ε_H, as follows

$$El^\beta = \frac{Wi}{Re}\beta = \frac{\lambda\eta}{\rho w_c^2}e^{\varepsilon_H} \tag{7.1}$$

Fig. 7.19 shows the $Wi - Re/\beta$ diagram constructed for the various contraction ratios. The slope of El^β now scales with β to map out the different flow patterns obtainable in the different contraction ratios. Essentially, the differences in the flow patterns are due to the contraction ratios, which reflects the Hencky strain experienced by the polymer molecules. This diagram is comparable in many respect with the $Wi - Re$ diagram obtained in our laboratory for similar contraction ratios in the microfluidic experiment [83]. It may be seen that decreasing the contraction ratio essentially results in more stable flows, indicating less severe fluid stretching in the lower contraction ratio geometries. The flow patterns in

the 4:1 and 8:1 geometries are time-dependent but more symmetric compared with the 16:1 flow at high Wi. In the 16:1 flow, which represents the high El^{β} flow regime, the vortices are more asymmetric and fluctuates in time with a period that is greater than that which is displayed by the fluid in the lower contraction ratios.

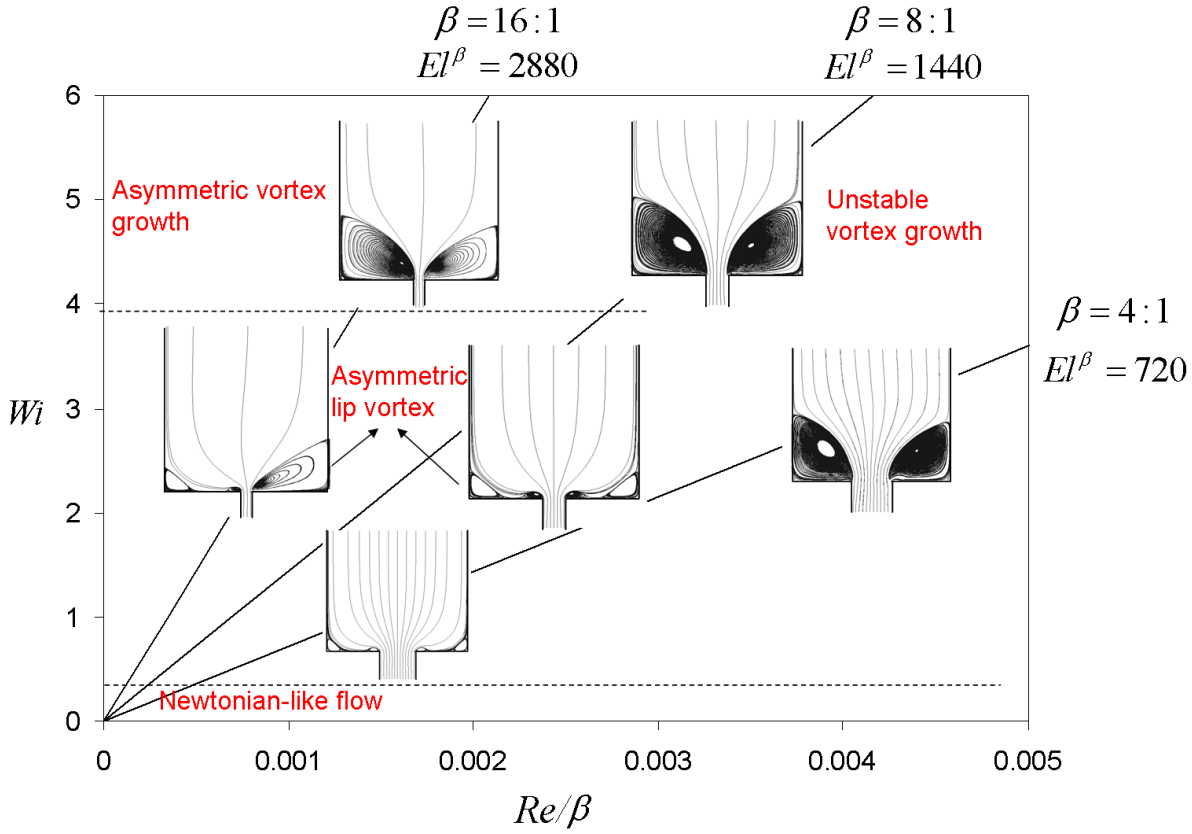

Figure 7.19: Stability diagram for the FENE-CD-JS ($\kappa = 0.1, L^2 = 100$) model showing the effect of fluid elasticity for various contraction ratios on the flow pattern.

7.5 Conclusions

Elastic flow instability has been simulated in the contraction geometry using the FENE-CD-JS model with the non-linear model parameter $\kappa > 0$. Substantial time-dependent asymmetric flow patterns were predicted as seen in experiments. The constant drag FENE-CD-JS model also showed some time-dependent behaviour, but only asymmetric lip vortices were predicted. The Phan-Thien-Tanner model predicted fairly stable flow patterns over the range of the Wi investigated. For the three models, matching steady

elongational viscosities in homogeneous flow were sought by the choice of model parameters but the predictions of the models in transient flow were significantly different.

Further investigations were carried out to study the effect of the inertial term and the contraction ratio on the elastic flow pattern. It appears that inertia destabilises the elastically-induced asymmetric structure of the fluid. A stability diagram has also been constructed to illustrate the effect of the contraction ratio on the fluid, which represents the flow of any given fluid by the trajectory of the dimensionless parameter $El^{\beta} = \beta Wi/Re$. The results show very similar flow patterns to those obtained experimentally using similar contraction ratios.

Chapter 8

Three-dimensional Flow of Polymer Solutions in a Planar Contraction

8.1 Introduction

The contents provided in this chapter have been published [15] as a conference proceedings following a presentation at the 5th Annual European Rheology Conference, Cardiff. The purpose of this work is to illustrate the effect of the aspect ratio in a three-dimensional contraction flow. This research is motivated by a better understanding of the non-linear dynamics of polymer solutions and developing microfluidic rheometry. Some researchers have conducted experiments in microfluidics without taking the aspect ratio into account. This has often led to results that are contrary to expectations because of the three-dimensional nature of the flow. For example, contraction flow experiments in which only the width of the downstream channel is varied in order to increase the Hencky strain endured by the fluid may effectively result in the opposite effect due to the higher downstream aspect ratio. The Hencky strain in three dimensional contraction flow is strongly influenced by both the contraction ratio and the aspect ratio of the geometry. Evidence from our laboratory [83, 142, 84, 85] suggests that the aspect ratio is very influential on the flow patterns in microfluidic devices. Unfortunately, the dimensionless parameters for characterising these flows such as the Weissenberg number, Reynolds number, and elasticity number, are often based on only one characteristic length scale, i.e. the width of the downstream channel. In microfluidic experiments, $Wi - Re$ stability diagrams are often

constructed based on only the width of the downstream length. Our 3-D numerical simulations show that such flow diagrams may be mis-leading in strongly three-dimensional flow without quoting the aspect ratio of the geometry.

In this chapter, three-dimensional flow of an exponential PTT fluid (E-PTT) in 8:1 planar contraction channels with various aspect ratios is studied. The model is fully characterised using material functions of a semi-dilute PEO solution. Numerical simulations are performed using the POLYFLOW finite element solver [31] based on one-quarter of the 3-D geometry and slightly rounded re-entrant corners. It is expected that rounding the re-entrant corner will have a favourable impact on numerical stability. The effect of the aspect ratio on the flow fields is studied by a series of upstream aspect ratios, AR, defined as the ratio of the depth, h, to the upstream width, w_u, of the channel, from ideal 2-D flow ($AR >> 1$) to strongly 3-D flow ($AR = 1/4$).

8.2 Parameter Estimation

The material functions used in the E-PTT model were extracted from a well-characterised semi-dilute solution of polyethylene oxide based on the linear and non-linear rheometric data [142]. A four-mode relaxation spectrum was obtained from the dynamic frequency sweep data. The shear-thinning parameter, ξ, of the E-PTT model was obtained by fitting the steady-shear viscosity data to the model. The resulting material functions and model parameters are given in Table 8.1. The value of the parameter ϵ, which controls the extensional viscosity, is taken as 0.001. The mean relaxation time is evaluated using the viscosity-average relaxation time given by

$$\lambda_m = \frac{\sum_i \lambda_i^2 G_i}{\sum_i \lambda_i G_i} \tag{8.1}$$

which gives a value of $\lambda_m = 28.73$ms.

The predictions of the E-PTT model in simple shear flow based on the material functions obtained are shown in Fig. 8.1. The figure shows the shear viscosity, η, the first normal stress coefficient, $\psi_1 = (\tau_{xx} - \tau_{yy})/\dot{\gamma}_{xy}^2$, and the ratio of the first normal stress difference to the shear stress N_1/τ_{xy} as a function of shear rate. The left vertical axis represents η and ψ_1, and the right vertical axis represents N_1/τ_{xy}. The prediction of

Table 8.1: Relaxation spectrum and estimated material parameter ξ of the E-PTT model

Mode i	G_i[Pa]	λ_i[ms]	η_i[mPa.s]	ξ
1	8.860	0.114	1.01	$5.00e^{-7}$
2	0.696	3.130	2.18	$5.81e^{-6}$
3	0.336	13.20	4.43	$9.77e^{-4}$
4	0.028	89.40	2.53	$1.60e^{-3}$
Solvent	-	-	1.00	–
Total			11.15	

the Trouton ratio, Tr, defined as the ratio of the extensional viscosity, η_E, to the zero shear-rate viscosity, η_0, is shown in Fig. 8.2.

8.2.1 Numerical solver

The numerical simulations have been performed using a parallel version (3.12) of the POLYFLOW solver [143]. A mixed finite element method (EVSS/SU), which combines the elastic-viscous split stress (EVSS) method [115] and streamline upwinding (SU) scheme [144] was used for discretising the governing equations. The streamline upwind finite element technique is based on the idea of introducing a streamline diffusion term into the constitutive equation. This technique is attractive for solving complex multi-dimensional flow problems because it removes spurious crosswind diffusion, which is caused by the addition of artificial diffusion to a convection-dominated convection/diffusion problem. Furthermore, the SU scheme has been reported to be very stable, especially when equations are solved in a coupled manner with a hybrid direct/iterative solver. An evolution technique was applied to advance the solution from purely Newtonian to fully viscoelastic flow. The boundary conditions used are as follows: fully developed velocity and stress profiles were prescribed at the inlet section. This was implemented in POLYFLOW by solving a finite-element problem along the boundary section, based on a specified flow rate. At the outlet section, a zero tangential velocity and a fully developed normal velocity profile were prescribed, and Neumann conditions for stresses. A no-slip condition was prescribed along the walls.

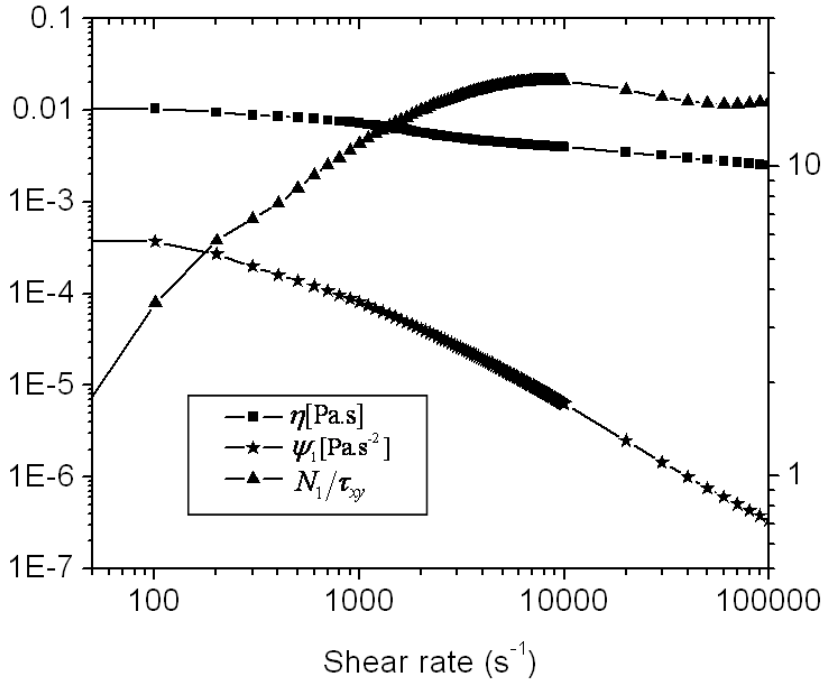

Figure 8.1: Prediction of the E-PTT model in simple shear flow. The left vertical axis represents η and ψ_1, and the right vertical axis represents N_1/τ_{xy}.

8.2.2 Dimensionless parameters

The relevant dimensionless numbers are the Reynolds number, Re, the Weissenberg number, Wi, and the elasticity number, El. These are defined as follows.

Reynolds number.

The Reynolds number is given by

$$Re = \frac{\rho U_c l_c}{\eta_0} \tag{8.2}$$

where ρ is the density of the fluid, U_c is the mean velocity in the contraction channel, η_0 is the zero-shear rate viscosity, and l_c is the characteristic length of the channel. For 3-D flow geometry, it is typical to take l_c as the hydraulic diameter of the contraction channel [16, 145], which is given by $D_{h,c} = 2hw_c/(h+w_c)$. Following from this definition, 2-D flow represents the limiting case $h/w_c \gg 1$, for which $D_{h,c} \to 2w_c$. Therefore, for 2-D flow, we take $l_c = 2w_c$ instead of w_c, which is commonly used. The mean velocity is taken as by $U_c = Q/(hw_c)$, based on the downstream channel, where Q is the flow rate.

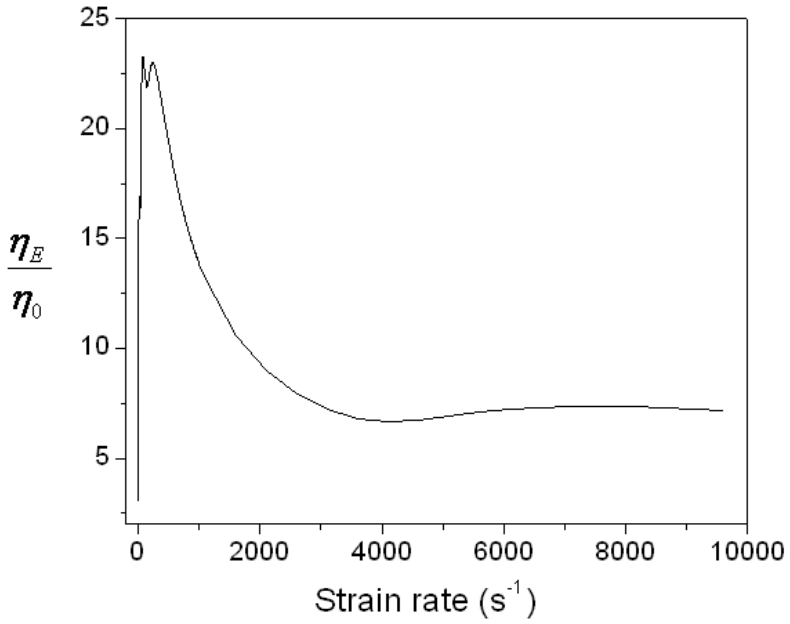

Figure 8.2: Prediction of Trouton ratio by the E-PTT model under uniaxial extensional flow.

Weissenberg number.

The Weissenberg number is defined as the product of the characteristic relaxation time, λ_m, of the fluid and the mean shear rate in the downstream channel, $\dot{\gamma}_c = U_c/(w_c/2)$

$$Wi = \lambda\dot{\gamma}_c = \frac{\lambda_m U_c}{w_c/2} \tag{8.3}$$

Note that in comparing 3-D results of different aspect ratios at the same Wi, we consider flows at the same mean velocity, U_c, but different flow rate, Q, since Q varies with the aspect ratio.

Elasticity number.

The elasticity number is defined as the ratio of the Weissenberg number to the Reynolds number as follows,

$$El = \frac{Wi}{Re} = \frac{2\lambda_m\eta_0}{\rho w_c D_h} = \frac{\lambda_m\eta_0(w_c+h)}{\rho h w_c^2} \tag{8.4}$$

Eq. 8.4 shows that El is independent of the kinematics of the flow but depends only on fluid properties and flow geometry.

8.3 Geometry and Mesh

Mesh density dependence of the solution is conducted using three 2-D meshes, M1, M2 and M3 having 1035, 1280, 2760 elements respectively. The geometries are designed with a corner curvature of radius, $R_c = 0.1w_c$. Solution convergence with mesh refinement is demonstrated by comparing the profiles of the velocity and the first normal stress difference along the centreline, and at a position $y = 0.4w_c$ cross-stream, measured from the centre. The velocity profiles shown in Figs. 8.3 are almost identical for the three meshes, with only slight deviations in the entry region. Similar results are obtained for the profiles of the first normal stress difference shown in Fig. 8.4.

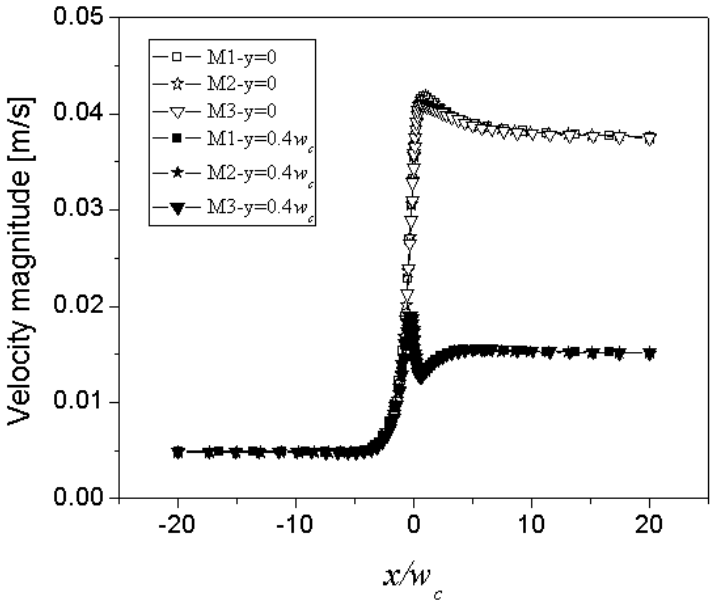

Figure 8.3: Velocity magnitude along x direction at the positions $y = 0$ and $y = 0.4w_c$ ($Re = 0.465, Wi = 15$).

The velocity and stress fields resulting from slightly rounded-corner contractions are expected to be quantitatively similar to those obtained from equivalent sharp-corner geometries in the majority of the flow domain except at the entry region where they might be slightly different. Rothstein and McKinley [81] demonstrated that the vortex length and pressure drop data obtained from both sharp and rounded-corner contractions can be plotted on a single master curve by using an equivalent definition for Wi, given by $Wi_s = \lambda_m U_c/(w_c/2 + R_c)$, for rounded-corner geometries. In the present work, using

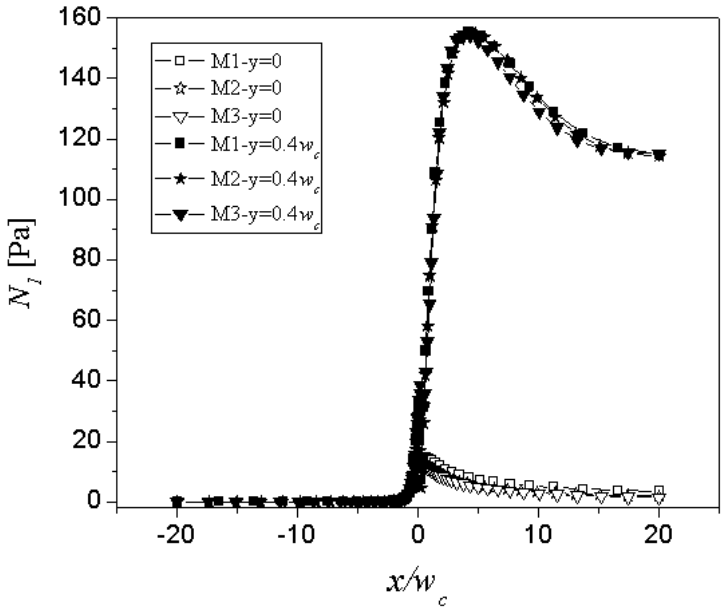

Figure 8.4: First normal stress along x direction at the positions $y = 0$ and $y = 0.4w_c$ $(Re = 0.465, Wi = 15)$.

$R_c = 0.1w_c$ in this expression gives a scaling factor of $Wi/Wi_s = 1.2$.

Fig. 8.5 shows the geometry and computational mesh for one-quarter of the full 3-D geometry with planes of symmetry defined along the boundaries $y = 0$ and $z = 0$. Fig. 8.6 shows the graded mesh along the plane of symmetry $z = 0$, and a magnified view of the entry region showing the corner curvature of radius R_c.

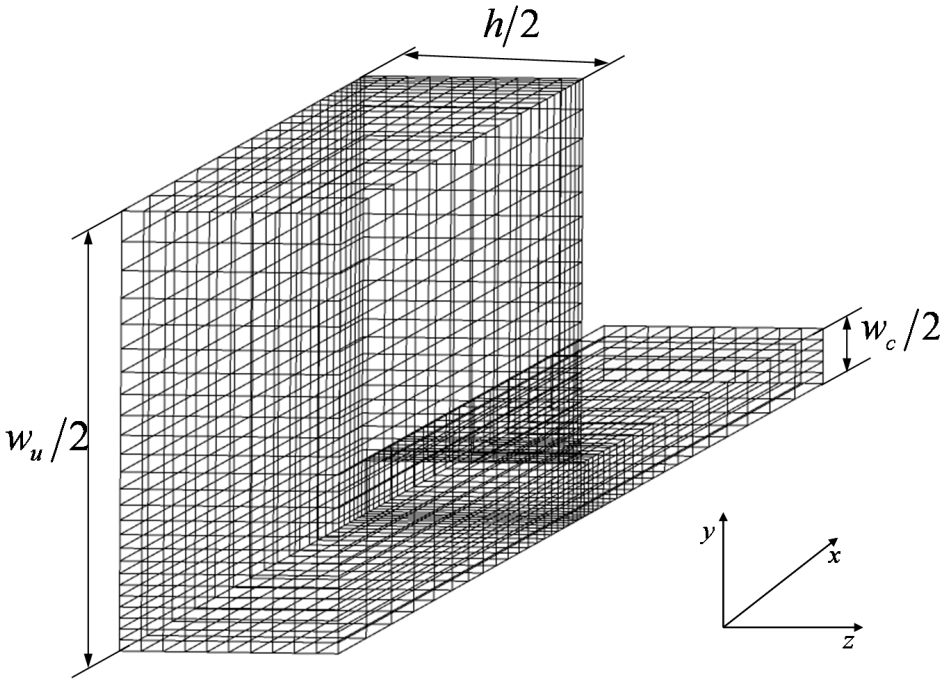

Figure 8.5: 3-D planar contraction geometry and graded mesh. The computational domain is one-quarter of the flow geometry.

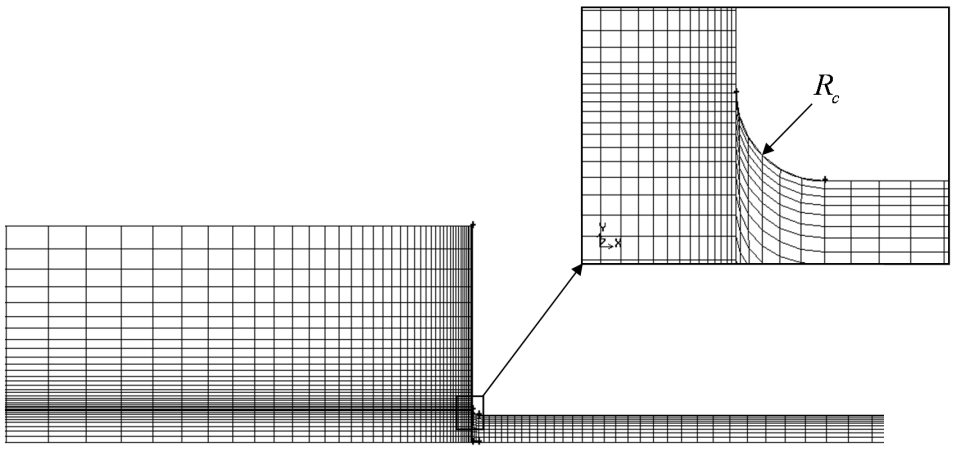

Figure 8.6: Plane of symmetry $z = 0$ showing graded mesh and a magnified view of the entry region.

8.4 Effect of the aspect ratio on vortex growth dynamics

The effect of the aspect ratio on the flow kinematics is investigated using the upstream aspect ratios, $AR = 1$, $1/2$, and $1/4$. Fig. 8.7 shows the vortex patterns of 2-D simulations for $Wi = 1.44$, 5.75 and 10. The elasticity number for this geometry is fixed and it is given by $El = 32.2$. Fig. 8.8 shows corresponding results of 3-D simulations along the plane $z = 0$ for $AR = 1$ and $El = 36.3$. The two set of results show a similar trend, i.e., as Wi is increased a salient corner vortex can be seen growing into a larger corner vortex and fingering towards the re-entrant corner. These results are in agreement with the salient-corner vortex enhancement mechanism that is often observed with the PTT fluid in 2-D simulations [71, 73], and in 3-D simulations using $AR = 1$ [62]. The vortices in the 2-D simulations are, however, generally larger in size than the corresponding 3-D results for the same Wi. Xue *et al.* [62] suggested that 2-D flow approximation is valid only when the aspect ratio of the channel is at least greater than 10. However, such high aspect ratios are not very common in microfluidic applications.

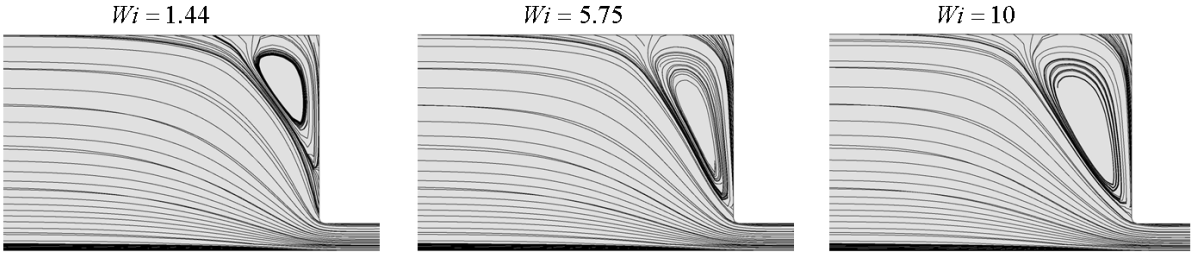

Figure 8.7: Streamline patterns for 2-D flow ($AR \gg 1$ and $El = 32.2$).

Fig. 8.9 shows the vortex patterns along the plane $z = 0$ for 3-D simulations with $AR = 1/2$ and $El = 40.3$. The results are presented at $Wi = 3.5$, 5.75 and 7. These results also show a salient-corner vortex growth mechanism, although the vortex sizes are smaller compared with those observed in the $AR \gg 1$ and $AR = 1$ configurations. By contrast, the 3-D simulations with $AR = 1/4$ and $El = 48.3$ (see Fig. 8.10) show a lip vortex growth mechanism. A lip vortex appears at $Wi = 3.75$, which grows downstream and fingering towards the salient corner at $Wi = 5.75$. At $Wi = 7$, the vortex has grown into a convex-shaped corner vortex (looking from left to right) in contrast to the

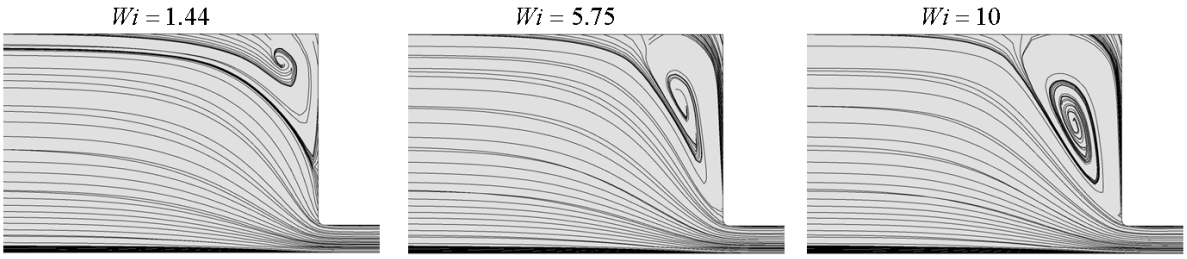

Figure 8.8: Streamline patterns for 3-D flow with $AR = 1$ and $El = 36.3$ along the plane $z = 0$.

concave-shaped vortices seen in the higher aspect ratio results.

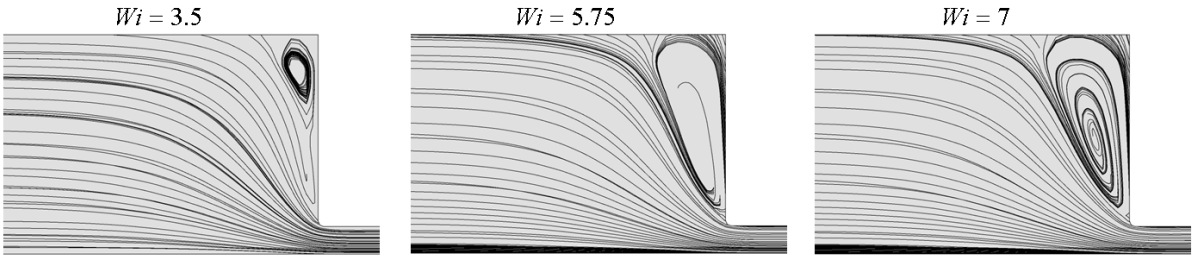

Figure 8.9: Streamline patterns for 3-D flow with $AR = 1/2$ and $El = 40.3$ along the plane $z = 0$.

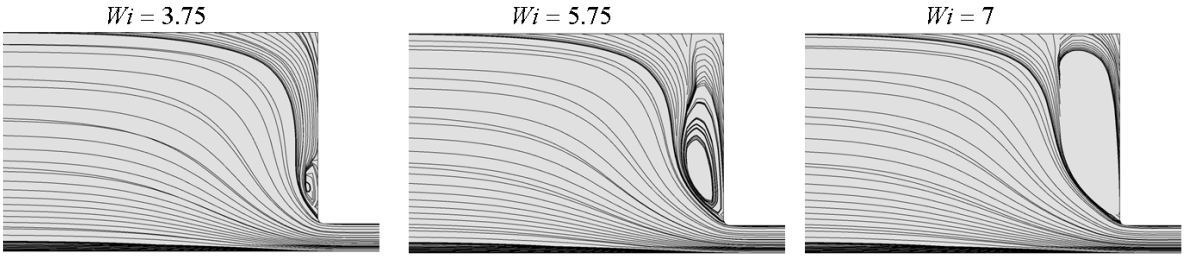

Figure 8.10: Streamline patterns for 3-D flow with $AR = 1/4$ and $El = 48.3$ along the plane $z = 0$.

These results are summarised on the $Wi - Re$ vortex pattern map in Fig. 8.11. The diagram is only semi-quantitative. It shows the trajectories followed by the E-PTT fluid in 8:1 contraction channels with the aspect ratio decreasing from a 2-D flow ($AR \gg 1$) to $AR = 1/4$, which correspond to the elasticity numbers in the range $32.2 \leq El \leq 48.3$. The figure also shows the two regions of vortex growth mechanism separated by a

transition zone. The transition from a corner vortex mechanism to a lip vortex mechanism is predicted between $AR = 1/2$ and $1/4$ (i.e. $El = 40.3$ and 48.3).

A similar transition in vortex growth mechanism is usually observed in experiments and simulations involving increasing El, which is achieved either by varying the fluid properties for a fixed geometry [16, 80], or by increasing the contraction ratio for a given fluid [61, 72]. By considering the definition of the elasticity number (see Eq. 8.4), it can be seen that varying any of the fluid properties (λ_m, η_0, or ρ) will directly affect El. The effect of increasing the contraction ratio is often associated with higher total Hencky strain, defined as $\ln(w_u/w_c)$ for planar contractions, experienced by polymer molecules during the converging flow. We note that the contraction ratio, w_u/w_c, can either be increased by increasing w_u for a fixed w_c, or by decreasing w_c for a fixed w_u, the latter of which will directly affect El. The role of the aspect ratio on El can be similarly explained in terms of h.

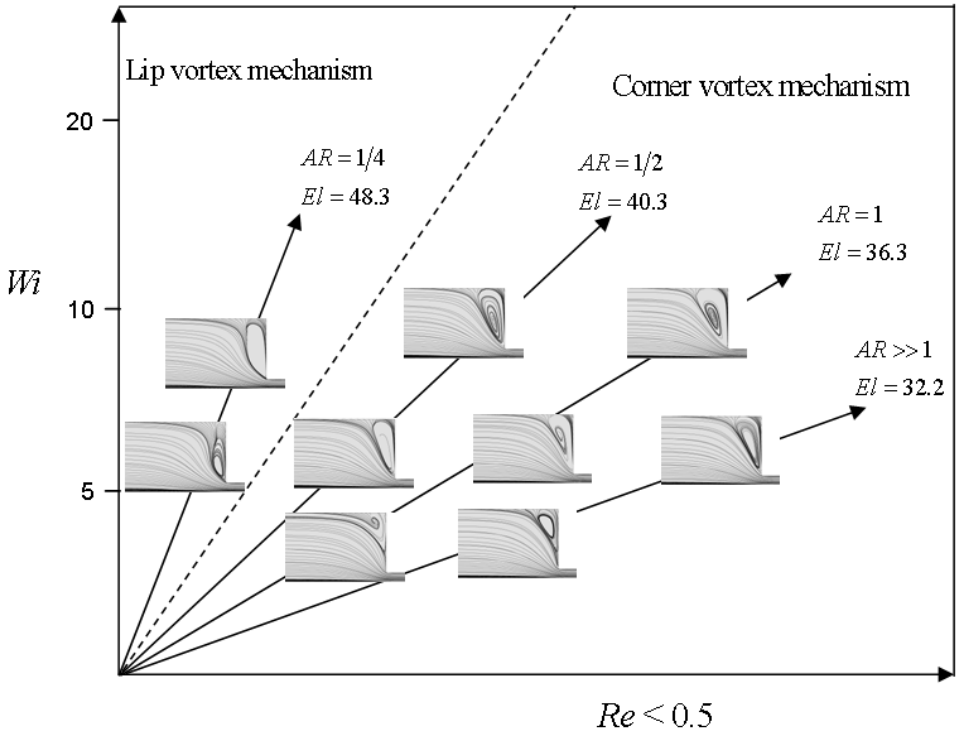

Figure 8.11: $Wi - Re$ diagram for the E-PTT fluid obtained by changing the aspect ratio of 8:1 contraction channels. The dashed line (- - -) represents the transition zone between the salient-corner vortex enhancement mechanism and the lip vortex enhancement mechanism.

In Fig. 8.12, the size of the corner vortices is plotted in dimensionless form, χ_L, (normalised by the half width of the downstream channel) as a function of the aspect ratio. The plot shows the variation of the dimensionless vortex length with the aspect ratio at Wi 5.75. The dimensionless vortex length undergoes a significant shrink in size as the aspect ratio is decreased from 1/2 to 1/4, which is a result of the transition in the vortex mechanism. The result for $AR \gg 1$ is represented by an asymptotic (dashed) line, which is given by $\chi_L = 3.23$.

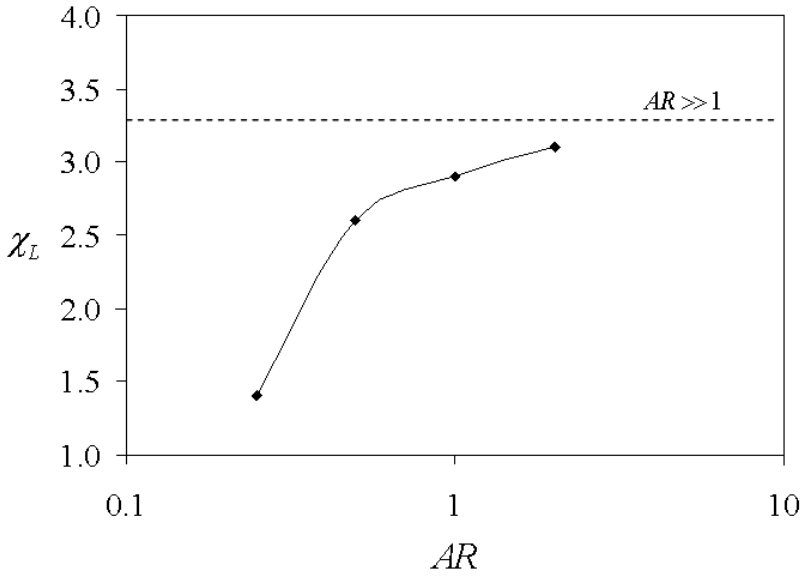

Figure 8.12: Variation of dimensionless vortex length, χ_L, with the aspect ratio at $Wi = 5.75$. The asymptotic (dashed) line represents the result for $AR \gg 1$ ($\chi_L = 3.23$)

The above transition in vortex growth mechanism can also be seen from the 3-D views in Figs. 8.13 and 8.14. These results are reported for the $AR = 1/2$ and 1/4 simulations at $Wi = 5.75$. Fig. 8.13 shows the vortex patterns in the planes $z = -h/4$ and $y = w_u/4$, and Fig. 8.14 shows the pathlines for the above flows. In Fig. 8.13, the streamlines in the plane $y = w_u/4$ show a bifurcation line separating the primary flow zone from the re-circulation zone, which increases in the z direction from the plane of symmetry ($z = 0$) to the side wall ($z = -1/2$). This can also be seen from the pathlines in Fig. 8.14. For $AR = 1/2$, the recirculation zone can be seen increasing more rapidly towards the side wall compared with $AR = 1/4$.

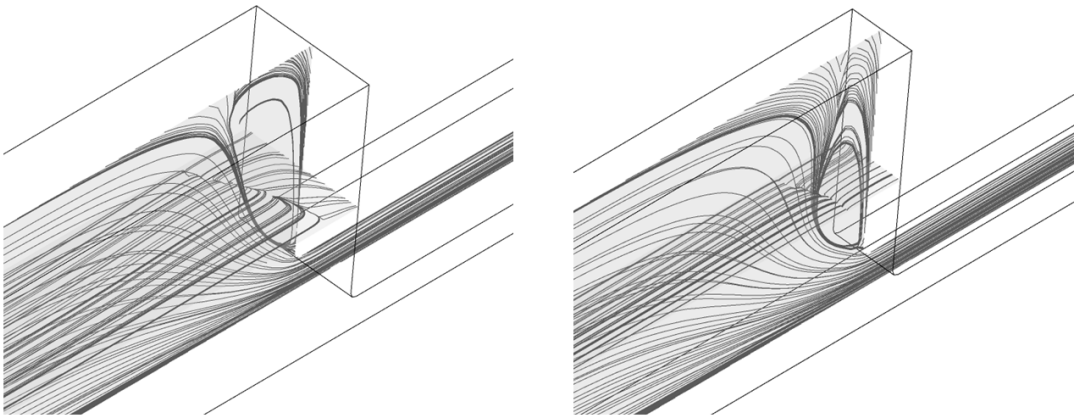

Figure 8.13: 3-D view showing vortex patterns along the planes $z = -h/4$ and $y = w_u/4$ for (a) $AR = 1/2$ and (b) $AR = 1/4$ at $Wi = 5.75$.

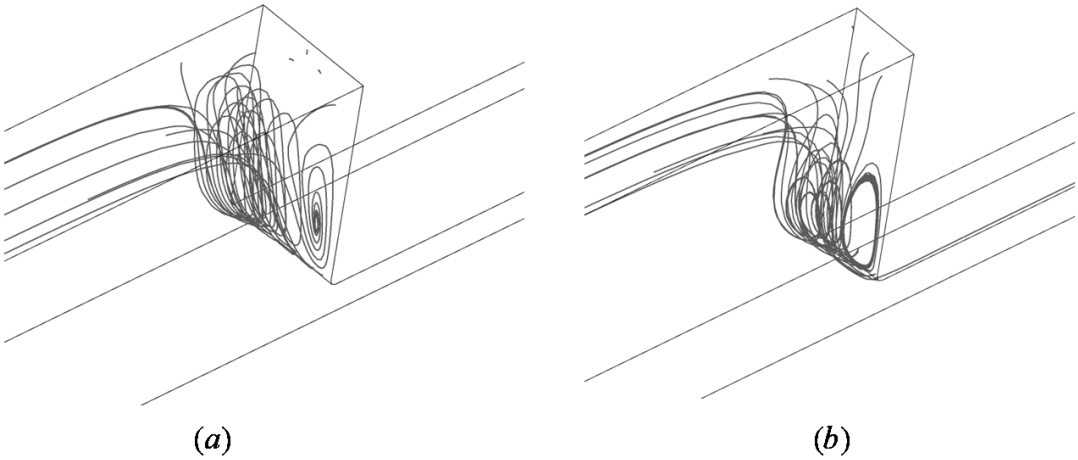

Figure 8.14: 3-D view showing pathlines for (a) $AR = 1/2$ and (b) $AR = 1/4$ at $Wi = 5.75$.

8.5 Effect of the aspect ratio on dynamic fields

In Fig. 8.15, we compare profiles of the first normal stress difference, N_1, normalised by $(w_c/2)(-dp/dx)_{c,FD}$ for different aspect ratios at $Wi = 5.75$, in which $(-dp/dx)_{c,FD}$ is the (constant) pressure gradient calculated for fully developed flow in the downstream channel. The inset is a plot of the maximum values of the normalised first normal stress difference, $N_{1,max}/((w_c/2)(-dp/dx)_{c,FD})$, as a function of the aspect ratio. The first normal stress difference is found to increase rapidly with decreasing aspect ratio. This result depicts a non-linear correlation between the aspect ratio and the first normal stress difference.

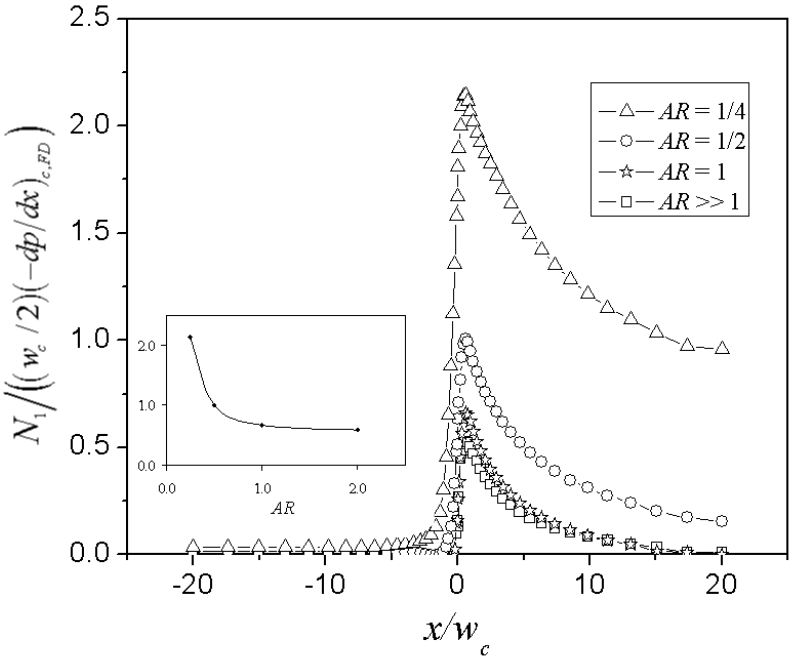

Figure 8.15: Profiles of normalised first normal stress difference along the x direction (at the position $y = 0$, $z = -h/4$) at $Wi = 5.75$ for different AR. The inset is a plot of the maximum values of normalised first normal stress difference, $N_{1,max}/((w_c/2)(-dp/dx)_{c,FD})$, as a function of AR.

Figs. 8.16(a)-(c) show the plot of the dimensionless pressure distribution, $\frac{p-p_{ref}}{(w_c/2)(-dp/dx)_{c,FD}}$, in the entry region for the range $1.44 \leq Wi \leq 7$. In the figure, the results for the various aspect ratios are presented as follows, $AR \gg 1$ in (a), $AR = 1/2$ in (b), and $AR = 1/4$ in (c). The pressure distributions clearly show distinct trends. Fig. 8.16(d) plots the

Couette correction coefficient, C, against Wi. For all the aspect ratios, C is found to be a negative decreasing non-linear function of Wi. Within the range of Wi investigated C is similar for all the aspect ratios, except for $AR = 1/4$, in which C is much greater due to stronger 3-D effects. Note that the curve for $AR = 1/4$ is almost linear in a range of Wi up to 5.75, within which the flow is dominated by the lip vortex growth mechanism.

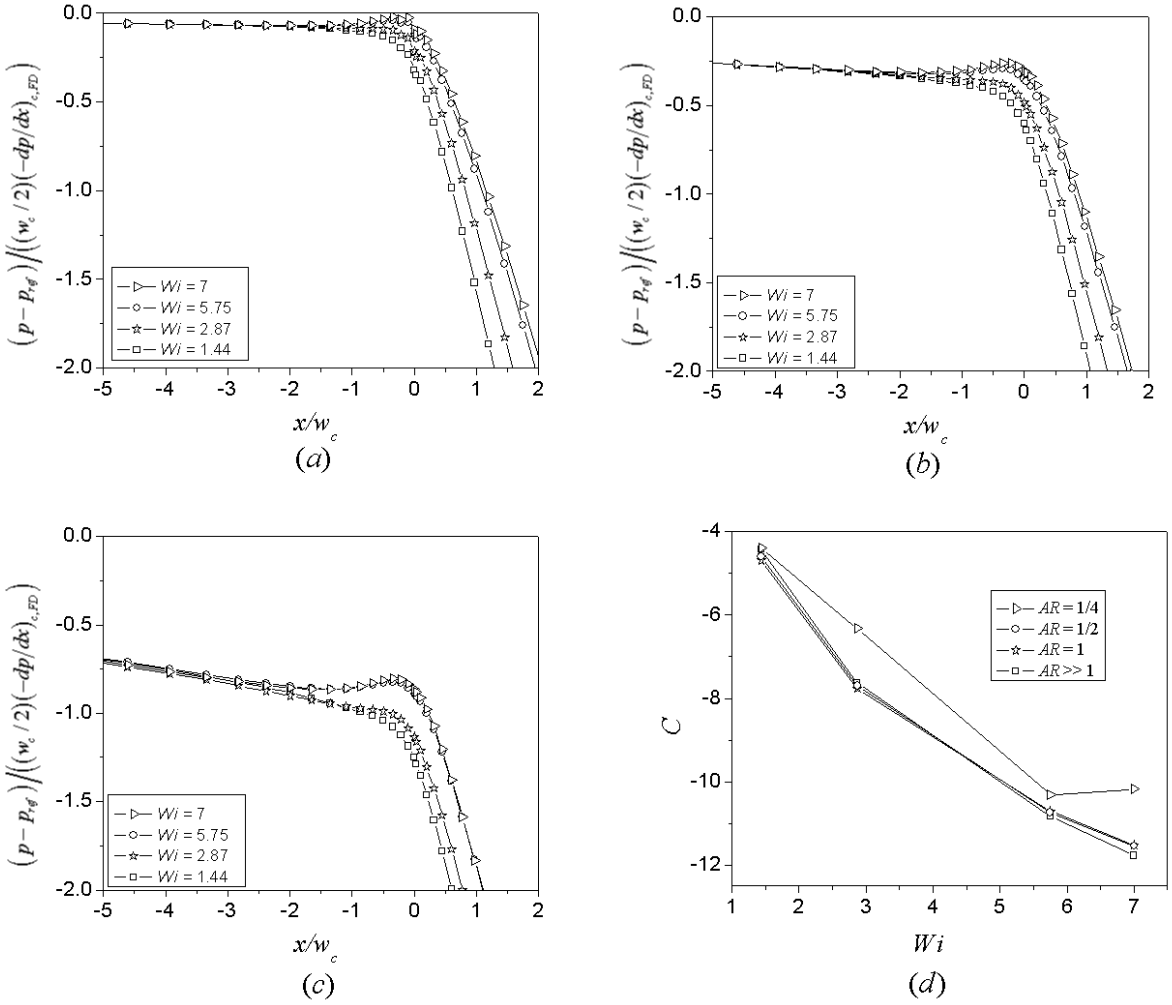

Figure 8.16: Dimensionless pressure distribution, $(p - p_{ref})/((w_c/2)(-dp/dx)_{c,FD})$, along the x direction (at the position $y = 0$, $z = 0$ for different Wi predicted for (a) $AR \gg 1$ (ideal 2-D flow) (b) $AR = 1/2$ (c) $AR = 1/4$. (d) Couette correction, C, for different aspect ratios as a function of Wi.

8.6 Conclusions

The three-dimensional flow of a semi-dilute PEO solution in 8:1 planar contraction channels with various aspect ratios has been studied by finite element calculations using POLYFLOW. The linear and non-linear material functions of the sample were extracted by fitting its rheometric data with the E-PTT model. The effect of the aspect ratio on the flow fields has been demonstrated by a transition in vortex mechanism from a salient-corner to a lip vortex mechanism as the aspect ratio is varied from ideal 2-D flow ($AR \gg 1$) to strongly 3-D flow ($AR = 1/4$). Vortex growth dynamics are governed by a salient-corner mechanism in the channels with aspect ratio greater than 1/4, whereas for $AR = 1/4$, a lip vortex mechanism is observed. By varying the aspect ratio of the channels the elasticity number of the flow has been altered, which suggests that the aspect ratios in contraction flows might have a similar effects as varying other parameters, such as the fluid property, which influence the elasticity number. A complete $WiRe$ diagram would provide a valuable blueprint for non-linear dynamics of polymer solutions and optimisation of microfluidic designs for a wide range of applications.

Chapter 9

Summary and Future Work

9.1 Summary

This work has evaluated the capability of selected constitutive models to predict elastic flow phenomena in complex flows. The work is embodied within an integrated experimental and computational approach with the ultimate goal of developing a better understanding of the non-linear dynamics of polymer solutions obtainable in microfluidic systems. In the present study, the cross-slot and contraction geometries have been used as benchmark flow problems.

A numerical scheme based on the finite volume method has been implemented within the OpenFOAM framework and rigorously tested against very reliable literature results in the benchmark flow. The FENE dumbbell model has been modified to allow for the non-affine deformation of polymer solutions. This modification replaces the upper convected time derivative in the FENE dumbbell model with the Johnson-Segalman derivative, which enabled the prediction of some non-linear material functions including the shear-thinning behaviour of the shear viscosity and a non-vanishing second normal stress difference. Due to the stabilising effect of the J-S derivative and the non-linear coupling between the evolution of the polymer microstructure and the macroscopic flow fields, the model can predict strong viscoelastic flow phenomena which have been observed in the high El flow regime for dilute polymer solutions in benchmark flows.

Numerical simulations have been conducted in 2-D cross-slot and contraction flows in the high El flow regime. In the cross-slot, time-dependent stability diagrams were

constructed based on the fluid elasticity, Wi, and the applied strain, ε, on the fluid calculated at the stagnation point. The FENE-CD-JS model predicted a substantially extended and broader birefringence in comparison to the L-PTT and FENE-CR models. In the stability diagrams, three distinct flow regimes were delineated for all three models, namely, steady symmetric flow, steady asymmetric flow, and unsteady asymmetric flow. The FENE-CD-JS model also predicted a flow transition in which the flow goes directly from a steady symmetric to an unsteady asymmetric flow without passing through the steady asymmetric flow regime.

For the 2-D computations in the 16:1 planar contraction, three models, namely, the L-PTT model, the FENE-CD-JS model with constant drag, and the FENE-CD-JS model with non-linear drag were compared in steady-state and transient homogeneous flows. The dynamic behaviour of the fluids in transient flow differs significantly from their steady-state prediction. In the contraction flow, the conformation-dependent FENE-CD-JS model clearly shows a transition from a Newtonian-like flow to asymmetric vortex growth regime, in which the vortex in one corner becomes significantly larger than the other. Asymmetric lip vortices were also predicted at lower Wi. Snapshots of the streamlines at higher Wi associated the lip vortex mechanism with the onset of the time-dependent flow behaviour. For the constant drag FENE-CD-JS model, unsteady asymmetric lip vortices were seen at $Wi = 5$, whereas the L-PTT model did not show any noticeable time-dependent behaviour. The effect of the contraction ratio was studied using a stability diagram based on the dimensionless parameter, El^{β}, which accounts for the contraction ratio of the geometry. The trajectories represented by El^{β} describes the flow regime of a given fluid for a given contraction ratio.

Further investigations were carried out to study the effect of the aspect ratio on the flow of a polymer solution in a three-dimensional contraction geometry. The simulations were conducted by systematically varying the depth of the channel for a fixed contraction ratio and the results were mapped on a $Wi - Re$ flow diagram, which showed that varying the aspect ratio of the geometry effectively alters the elasticity number of the fluid. The simulations also predicted a transition from a corner vortex to a lip vortex mechanism as the aspect ratio is reduced from an ideal 2-D flow to a strongly 3-D flow.

9.2 Perspectives and Future Work

The outcomes of this thesis may have significant implications with regards to our understanding of the dynamics of polymer solutions in complex geometries. The work has shown that the fundamental mechanism by which polymer molecules are rapidly extended in flow is an important physical process, which is represented by a non-linear coupling between the applied macroscopic flow fields and the evolution of the polymer microstructure. Based on this idea, highly elastic flow phenomena have been studied using such a constitutive model as simple as the FENE-CD-JS for dilute polymer solutions. This suggests that such flow regimes, which were recently explored by microfluidic experimental techniques are readily accessible by numerical simulations using suitable models and stable computational techniques. The experimental techniques can probe very high deformation rates and, thus very short time scales of the fluid, which gives rise to intriguing flow phenomena even for very dilute polymer solutions. Therefore, as shown in this work it is possible to predict these flows using simple mechanical models. However, for concentrated solutions the basic assumptions of the dumbbell model will breakdown and polymer-polymer interactions must be considered.

Further work will fully characterise the FENE-CD-JS model using multi-mode material functions based on dilute to semi-dilute polymer solutions and perform three-dimensional numerical simulations in order to make quantitative comparisons with experimental results. Such simulations will be very useful given the enormous amount of efforts often involved in performing microfluidic experiments, for example, the exasperating task of dislodging a trapped air bubble from the device. Although numerical simulations are not substitutes for experiments, they can serve as a handy back-up tool for experiments in predicting complex flow phenomena such as the onset of instabilities as well as for the optimisation of geometric designs for a wide range of applications.

Further work will also attempt to simulate more complicated dynamics of concentrated polymers and suspension systems by techniques such as the micro-macro simulation approach, in which the polymer stress is computed with a molecular simulation technique and coupled with the macroscopic flow fields [11]. Such a simulation technique has the potential to better capture the behaviour of polymer solutions in complex flows.

Appendix A

Non-linear Modification to the FENE Dumbbell Model - An Alternative Argument To Drag Force

In this thesis, we have considered the conformation-dependent drag FENE dumbbell model as a modification to the hydrodynamic drag coefficient. We give an alternative argument based on a modification to the spring force constant.

We can write the FENE-CD-JS model as follows,

$$\overset{\triangledown}{\boldsymbol{A}} + \frac{1}{2}\xi(\boldsymbol{D}\cdot\boldsymbol{A} + \boldsymbol{A}\cdot\boldsymbol{D}) = -\frac{f(\mathrm{tr}(\boldsymbol{A}))}{\lambda h(\mathrm{tr}(\boldsymbol{A}))}(\boldsymbol{A}-\boldsymbol{I}) \tag{A.1}$$

substituting for $f(\mathrm{tr}(\boldsymbol{A}))$ and $h(\mathrm{tr}(\boldsymbol{A}))$ in this equation gives,

$$\overset{\triangledown}{\boldsymbol{A}} + \frac{1}{2}\xi(\boldsymbol{D}\cdot\boldsymbol{A} + \boldsymbol{A}\cdot\boldsymbol{D}) = -\frac{\boldsymbol{A}-\boldsymbol{I}}{\lambda\left(1-\frac{\mathrm{tr}(\boldsymbol{A})}{L^2}\right)\left(1-\kappa+\kappa\sqrt{\frac{1}{2}\mathrm{tr}(\boldsymbol{A})}\right)} \tag{A.2}$$

thus we can define a non-linear function, $\mathcal{F}(\mathrm{tr}(\boldsymbol{A}))$, such that

$$\mathcal{F}(\mathrm{tr}(\boldsymbol{A})) = -\frac{1}{\left(1-\frac{\mathrm{tr}(\boldsymbol{A})}{L^2}\right)\left(1-\kappa+\kappa\sqrt{\frac{1}{2}\mathrm{tr}(\boldsymbol{A})}\right)} \tag{A.3}$$

hence Eq. A.2 becomes,

$$\overset{\triangledown}{\boldsymbol{A}} + \frac{1}{2}\xi(\boldsymbol{D}\cdot\boldsymbol{A} + \boldsymbol{A}\cdot\boldsymbol{D}) = -\frac{\mathcal{F}(\mathrm{tr}(\boldsymbol{A}))}{\lambda}(\boldsymbol{A}-\boldsymbol{I}) \tag{A.4}$$

In this equation the introduction of $\mathcal{F}(\mathrm{tr}(\boldsymbol{A}))$ in Eq. A.4 may be considered as a direct modification to the Hookean spring force law now given as $\boldsymbol{F} = \mathcal{H}(\mathrm{tr}(\boldsymbol{A}))\boldsymbol{Q}$, in which the modified spring force constant, $\mathcal{H}(\mathrm{tr}(\boldsymbol{A})) = \mathcal{F}(\mathrm{tr}(\boldsymbol{A}))H$, is expressed in terms of a constant drag coefficient, ζ_0, and relaxation time, λ_0. For $\kappa = 0$, $\mathcal{F}(\mathrm{tr}(\boldsymbol{A})) = 1 - \frac{\mathrm{tr}(\boldsymbol{A})}{L^2}$ and the Warner [90] spring force law is recovered.

Fig. A.1 shows the plot of the spring force constant, $\mathcal{H}(\mathrm{tr}(\boldsymbol{A}))$, with dumbbell extension, $\mathrm{tr}(\boldsymbol{A})$, for some non-linear spring force laws. Thus as shown by the plots, the Warner spring force law is modified by κ yielding other spring force laws. For a given spring force law the spring stiffness increases with the end-to-end dumbbell extension, but with increasing κ the spring force law predicts a greater extension. The spring due

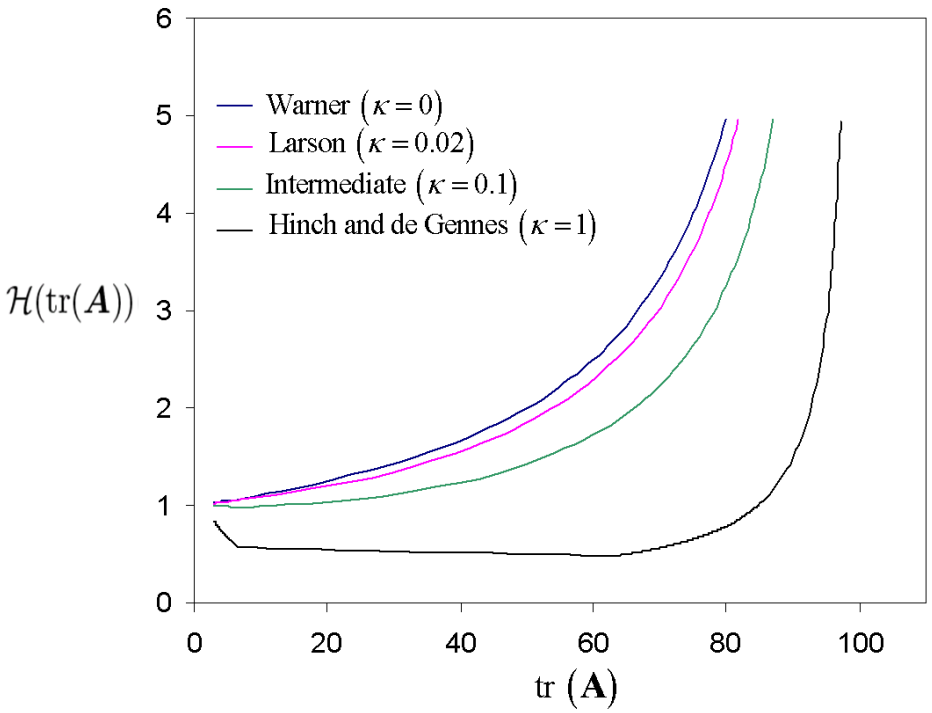

Figure A.1: Non-linear spring force laws for the FENE dumbbell model using $\xi = 0$, $L^2 = 100$, and $\zeta_0 = \lambda_0 = 1$

to Hinch [96] and de Gennes [97] displays a non-monotonic behaviour and predicts an excessively large extension, which suggests that this spring force law may not be suitable for dilute polymer solutions as observed by Harrison et al [146]. By contrast, the prediction of the Larson spring [1] and the intermediate spring agrees reasonably well with the Warner spring at very low extension and are within acceptable limits of extensibility.

This discussion has shown that the so-called non-linear drag model may also be considered as a direct modification to the spring force law. The alternative argument of non-linear drag coefficient assumes that the spring force must increase to counterbalance the hydrodynamic drag force [96, 147]. In either view, the spring force law is effectively modified.

Bibliography

[1] RG Larson. The unraveling of a polymer chain in a strong extensional flow. *Rheologica Acta*, 29(5):371–384, 1990.

[2] D.F. James and JH Saringer. Extensional flow of dilute polymer solutions. *Journal of Fluid Mechanics*, 97(04):655–671, 1980.

[3] G. Ryskin. Turbulent drag reduction by polymers: a quantitative theory. *Physical review letters*, 59(18):2059–2062, 1987.

[4] JM Rallison and EJ Hinch. Do we understand the physics in the constitutive equation? *Journal of Non-Newtonian Fluid Mechanics*, 29:37–55, 1988.

[5] LTD OPENCFD. OpenFOAM: The Open Source CFD Toolbox.

[6] M.A. Alves, P.J. Oliveira, and F.T. Pinho. Benchmark solutions for the flow of Oldroyd-B and PTT fluids in planar contractions. *Journal of Non-Newtonian Fluid Mechanics*, 110(1):45–75, 2003.

[7] H. Bible. King James Version. *New York, Scarborough, Ontario*, 1974.

[8] M. Reiner. The deborah number. *Physics Today*, 17:62, 1964.

[9] M.J. Crochet and K. Walters. Computational rheology: a new science. *Endeavour*, 17(2):64–77, 1993.

[10] R.G. Owens and T.N. Phillips. *Computational rheology*. Imperial College Press, 2002.

[11] R.G. Owens A. Lozinski and T.N. Phillips. The Langevin and Fokker-Planck Equations in Polymer Rheology. *Endeavour*, 17(2):64–77, 1993.

[12] R. Keunings. Micro-macro methods for the multiscale simulation of viscoelastic flow using molecular models of kinetic theory. *Rheology Reviews*, pages 67–98, 2004.

[13] R. Keunings. A survey of computational rheology. In *Proceedings of the XIIIth International Congress on Rheology*, volume 1, pages 7–14.

[14] R. Keunings. On the high Weissenberg number problem. *status: published*.

[15] SC Omowunmi and X.F. . Modelling the three-dimensional flow of a semi-dilute polymer solution in microfluidicson the effect of aspect ratio. *Rheologica Acta*, 49(6):585–595, 2010.

[16] L.E. Rodd, T.P. Scott, D.V. Boger, J.J. Cooper-White, and G.H. McKinley. The inertio-elastic planar entry flow of low-viscosity elastic fluids in micro-fabricated geometries. *Journal of Non-Newtonian Fluid Mechanics*, 129(1):1–22, 2005.

[17] L.E. Rodd, T.P. Scott, D.V. Boger, J.J. Cooper-White, and G.H. McKinley. The inertio-elastic planar entry flow of low-viscosity elastic fluids in micro-fabricated geometries. *Journal of Non-Newtonian Fluid Mechanics*, 129(1):1–22, 2005.

[18] X.F. Yuan, J. Odell, Z. Li, A. Lanzaro, S. Omowunmi, S. Haward, S. Yeates, C. Booth, and A. Kamp. Quantitative Characterization of Complex Fluids in Microfluidics. In *AIP Conference Proceedings*, volume 1027, page 252, 2008.

[19] P.E. Arratia, CC Thomas, J. Diorio, and JP Gollub. Elastic instabilities of polymer solutions in cross-channel flow. *Physical review letters*, 96(14):144502, 2006.

[20] C.J. Pipe and G.H. McKinley. Microfluidic rheometry. *Mechanics Research Communications*, 36(1):110–120, 2009.

[21] PJ Oliveira, FT Pinho, and GA Pinto. Numerical simulation of non-linear elastic flows with a general collocated finite-volume method. *Journal of Non-Newtonian Fluid Mechanics*, 79(1):1–43, 1998.

[22] A.I.A. Malkin, A.Y. Malkin, and A.I. Isayev. *Rheology: concepts, methods & applications*. Chem Tec Pub, 2006.

[23] DG Baird and M. Renardy. Report on the VIIth International Workshop on Numerical Methods in Non-Newtonian Flow. To appear. *J. Non-Newtonian Fluid Mech*, 1993.

[24] PJ Cable and DV Boger. A comprehensive experimental investigation of tubular entry flow of viscoelastic fluids: Part I. Vortex characteristics in stable flow. *AIChE Journal*, 24(5):869–879, 1978.

[25] PJ Cable and DV Boger. A comprehensive experimental investigation of tubular entry flow of viscoelastic fluids: Part III. Unstable flow. *AIChE Journal*, 25(1):152–159, 1979.

[26] RE Evans and K. Walters. Flow characteristics associated with abrupt changes in geometry in the case of highly elastic liquids. *Journal of Non-Newtonian Fluid Mechanics*, 20:11–29, 1986.

[27] RE Evans and K. Walters. Further remarks on the lip-vortex mechanism of vortex enhancement in planar-contraction flows. *Journal of Non-Newtonian Fluid Mechanics*, 32(1):95–105, 1989.

[28] JM Marchal and MJ Crochet. Hermitian finite elements for calculating viscoelastic flow. *Journal of Non-Newtonian Fluid Mechanics*, 20:187–207, 1986.

[29] JM Marchal and MJ Crochet. A new mixed finite element for calculating viscoelastic flow. *Journal of Non-Newtonian Fluid Mechanics*, 26(1):77–114, 1987.

[30] M. Fortin and A. Fortin. A new approach for the FEM simulation of viscoelastic flows. *Journal of Non-Newtonian Fluid Mechanics*, 32(3):295–310, 1989.

[31] MJ Crochet, R. Keunings, B. Debbaut, and JM Marchal. Polyflow: a multi-purpose finite element program for continuous polymer flows. *Computer Modeling for Extrusion and Other Continuous Polymer Processes*, pages 25–50, 1992.

[32] K.M. Dhanasekharan and J.L. Kokini. Design and scaling of wheat dough extrusion by numerical simulation of flow and heat transfer. *Journal of Food Engineering*, 60(4):421–430, 2003.

[33] RPG Rutgers and MR Mackley. Predicting extrusion surface instabilities for linear low density polyethylene. *The World of Polyflow*, 6:2–3, 2010.

[34] G.O. Aloku and X.F. Yuan. Numerical simulation of polymer foaming process in extrusion flow. *Chemical Engineering Science*, 2010.

[35] A.N. Brooks and T.J.R. Hughes. Streamline upwind/Petrov-Galerkin formulations for convection dominated flows with particular emphasis on the incompressible Navier-Stokes equations. *Computer methods in applied mechanics and engineering*, 32(1-3):199–259, 1982.

[36] R.G. Owens and T.N. Phillips. *Computational rheology*. Imperial College Pr, 2002.

[37] J. Yul Yoo and Y. Na. A numerical study of the planar contraction flow of a viscoelastic fluid using the SIMPLER algorithm. *Journal of non-newtonian fluid mechanics*, 39(1):89–106, 1991.

[38] MS Darwish, JR Whiteman, and MJ Bevis. Numerical modelling of viscoelastic liquids using a finite-volume method. *Journal of Non-Newtonian Fluid Mechanics*, 45(3):311–337, 1992.

[39] GP Sasmal. A finite volume approach for calculation of viscoelastic flow through an abrupt axisymmetric contraction. *Journal of Non-Newtonian Fluid Mechanics*, 56(1):15–47.

[40] SS Edussuriya, AJ Williams, and C. Bailey. A cell-centred finite volume method for modelling viscoelastic flow. *Journal of Non-Newtonian Fluid Mechanics*, 117(1):47–61, 2004.

[41] G.S. Jiang, D. Levy, C.T. Lin, S. Osher, and E. Tadmor. High-resolution nonoscillatory central schemes with nonstaggered grids for hyperbolic conservation laws. *SIAM Journal on Numerical Analysis*, 35(6):2147–2168, 1998.

[42] MA Alves, P. Cruz, A. Mendes, FD Magalhaes, FT Pinho, and PJ Oliveira. Adaptive multiresolution approach for solution of hyperbolic PDEs. *Computer Methods in Applied Mechanics and Engineering*, 191(36):3909–3928, 2002.

[43] MA Alves, PJ Oliveira, and FT Pinho. A convergent and universally bounded interpolation scheme for the treatment of advection. *International Journal for Numerical Methods in Fluids*, 41(1):47–75, 2003.

[44] T. Sato and S.M. Richardson. Explicit numerical simulation of time-dependent viscoelastic flow problems by a finite element/finite volume method. *Journal of Non-Newtonian Fluid Mechanics*, 51(3):249–275, 1994.

[45] P. Wapperom and MF Webster. Simulation for viscoelastic flow by a finite volume/element method. *Computer Methods in Applied Mechanics and Engineering*, 180(3-4):281–304, 1999.

[46] M. Aboubacar and MF Webster. A cell-vertex finite volume/element method on triangles for abrupt contraction viscoelastic flows. *Journal of Non-Newtonian Fluid Mechanics*, 98(2-3):83–106, 2001.

[47] TN Phillips and AJ Williams. Comparison of creeping and inertial flow of an Oldroyd B fluid through planar and axisymmetric contractions. *Journal of Non-Newtonian Fluid Mechanics*, 108(1-3):25–47, 2002.

[48] OG Harlen, JM Rallison, and P. Szabo. A split Lagrangian-Eulerian method for simulating transient viscoelastic flows. *Journal of non-newtonian fluid mechanics*, 60(1):81–104, 1995.

[49] M. Laso and HC
"Ottinger. Calculation of viscoelastic flow using molecular models: the CONNFFESSIT approach. *Journal of Non-Newtonian Fluid Mechanics*, 47:1–20, 1993.

[50] T. Shima, H. Kuni, Y. Okabe, M. Doi, X.F. Yuan, and T. Kawakatsu. Self-consistent-field theory of viscoelastic behavior of inhomogeneous dense polymer systems. *Macromolecules*, 36(24):9199–9204, 2003.

[51] F. Dupret, JM Marchal, and MJ Crochet. On the consequence of discretization errors in the numerical calculation of viscoelastic flow. *Journal of Non-Newtonian Fluid Mechanics*, 18(2):173–186, 1985.

[52] DD Joseph and JC Saut. Change of type and loss of evolution in the flow of viscoelastic fluids. *Journal of Non-Newtonian Fluid Mechanics*, 20:117–141, 1986.

[53] D.D. Joseph. *Fluid dynamics of viscoelastic liquids*. Springer New York, 1990.

[54] R. Fattal and R. Kupferman. Constitutive laws for the matrix-logarithm of the conformation tensor. *Journal of Non-Newtonian Fluid Mechanics*, 123(2-3):281–285, 2004.

[55] Y.J. Lee and J. Xu. New formulations, positivity preserving discretizations and stability analysis for non-Newtonian flow models. *Computer methods in applied mechanics and engineering*, 195(9-12):1180–1206, 2006.

[56] R. Fattal and R. Kupferman. Time-dependent simulation of viscoelastic flows at high Weissenberg number using the log-conformation representation. *Journal of Non-Newtonian Fluid Mechanics*, 126(1):23–37, 2005.

[57] A. Afonso, PJ Oliveira, FT Pinho, and MA Alves. The log-conformation tensor approach in the finite-volume method framework. *Journal of Non-Newtonian Fluid Mechanics*, 157(1-2):55–65, 2009.

[58] A. Afonso, MA Alves, FT Pinho, and PJ Oliveira. Benchmark calculations of viscoelastic flows with a finite-volume method using the log-conformation approach. In *3rd Annual European Rheology Conference*, pages 27–29.

[59] B. Purnode and MJ Crochet. Flows of polymer solutions through contractions Part 1: Flows of polyacrylamide solutions through planar contractions. *Journal of Non-Newtonian Fluid Mechanics*, 65(2-3):269–289, 1996.

[60] RE Evans and K. Walters. Further remarks on the lip-vortex mechanism of vortex enhancement in planar-contraction flows. *Journal of non-newtonian fluid mechanics*, 32(1):95–105, 1989.

[61] RE Evans and K. Walters. Flow characteristics associated with abrupt changes in geometry in the case of highly elastic liquids. *J. Non-Newtonian Fluid Mech*, 20(11), 1986.

[62] S.C. Xue, N. Phan-Thien, and RI Tanner. Three dimensional numerical simulations of viscoelastic flows through planar contractions. *Journal of Non-Newtonian Fluid Mechanics*, 74(1-3):195–245, 1998.

[63] K. Walters and MF Webster. On dominating elastico-viscous response in some complex flows. *Philosophical Transactions of the Royal Society of London. Series A, Mathematical and Physical Sciences*, pages 199–218, 1982.

[64] S. Xue, N. Phan-Thien, and R.I. Tanner. Numerical investigations of Lagrangian unsteady extensional flows of viscoelastic fluids in 3-D rectangular ducts with sudden contractions. *Rheologica Acta*, 37(2):158–169, 1998.

[65] S.C. Xue, RI Tanner, and N. Phan-Thien. Three-dimensional numerical simulations of viscoelastic flows–predictability and accuracy. *Computer Methods in Applied Mechanics and Engineering*, 180(3-4):305–331, 1999.

[66] PJ Oliveira and FT Pinho. Plane contraction flows of upper convected Maxwell and Phan-Thien–Tanner fluids as predicted by a finite-volume method. *Journal of Non-Newtonian Fluid Mechanics*, 88(1-2):63–88, 1999.

[67] D. V. Boger and R. J. Binnington. Circular entry flows of fluid m1. *Journal of Non-Newtonian Fluid Mechanics*, 35(2-3):339 – 360, 1990.

[68] H. Matallah, P. Townsend, and MF Webster. Recovery and stress-splitting schemes for viscoelastic flows. *Journal of Non-Newtonian Fluid Mechanics*, 75(2-3):139–166, 1998.

[69] M. Aboubacar, H. Matallah, HR Tamaddon-Jahromi, and MF Webster. Numerical prediction of extensional flows in contraction geometries: hybrid finite volume/element method. *Journal of Non-Newtonian Fluid Mechanics*, 104(2-3):125–164, 2002.

[70] M. Aboubacar, H. Matallah, and MF Webster. Highly elastic solutions for Oldroyd-B and Phan-Thien/Tanner fluids with a finite volume/element method: planar contraction flows. *Journal of Non-Newtonian Fluid Mechanics*, 103(1):65–103, 2002.

[71] M.A. Alves, P.J. Oliveira, and F.T. Pinho. Benchmark solutions for the flow of Oldroyd-B and PTT fluids in planar contractions. *Journal of Non-Newtonian Fluid Mechanics*, 110(1):45–75, 2003.

[72] M.A. Alves, P.J. Oliveira, and F.T. Pinho. On the effect of contraction ratio in viscoelastic flow through abrupt contractions. *Journal of Non-Newtonian Fluid Mechanics*, 122(1-3):117–130, 2004.

[73] MA Alves, PJ Oliveira, and FT Pinho. Numerical simulation of viscoelastic contraction flows. *Computational Fluid and Solid Mechanics. Amsterdam: Elsevier*, pages 826–829, 2003.

[74] MA Alves, FT Pinho, and PJ Oliveira. Effect of a high-resolution differencing scheme on finite-volume predictions of viscoelastic flows. *Journal of Non-Newtonian Fluid Mechanics*, 93(2-3):287–314, 2000.

[75] M.S.N. Oliveira, P.J. Oliveira, F.T. Pinho, and M.A. Alves. Effect of contraction ratio upon viscoelastic flow in contractions: The axisymmetric case. *Journal of Non-Newtonian Fluid Mechanics*, 147(1-2):92–108, 2007.

[76] H. Nguyen and DV Boger. The kinematics and stability of die entry flows. *J. Non-Newtonian Fluid Mech*, 5:353–368, 1979.

[77] S. A. White, A. D. Gotsis, and D. G. Baird. Review of the entry flow problem: Experimental and numerical. *Journal of Non-Newtonian Fluid Mechanics*, 24(2):121 – 160, 1987.

[78] J.P. Rothstein and G.H. McKinley. Extensional flow of a polystyrene Boger fluid through a 4: 1: 4 axisymmetric contraction/expansion. *Journal of Non-Newtonian Fluid Mechanics*, 86(1-2):61–88, 1999.

[79] S. Nigen and K. Walters. Viscoelastic contraction flows: comparison of axisymmetric and planar configurations. *Journal of Non-Newtonian Fluid Mechanics*, 102(2):343 – 359, 2002.

[80] LE Rodd, JJ Cooper-White, DV Boger, and GH McKinley. Role of the elasticity number in the entry flow of dilute polymer solutions in micro-fabricated contraction geometries. *Journal of Non-Newtonian Fluid Mechanics*, 143(2-3):170–191, 2007.

[81] J.P. Rothstein and G.H. McKinley. The axisymmetric contraction–expansion: the role of extensional rheology on vortex growth dynamics and the enhanced pressure drop. *Journal of Non-Newtonian Fluid Mechanics*, 98(1):33–63, 2001.

[82] Z. Li. Quantitative Characterization of Complex Fluids in Microfluidics. *PhD Thesis*, 2010.

[83] Li Z., Yuan X-F, Haward S., Odell J. A., and Yeates S. Non-linear Dynamics of Semi-dilute Polydisperse Polymer Solutions in Microfluidics: Effects of Flow Geometry. *Submitted*.

[84] A. Lanzaro and X-F. Yuan. Effects of Contraction Ratio on Non-linear Dynamics of Semi-Dilute, Highly Polydisperse PAAm Solutions in Microfluidics. *To be submitted*, 2011.

[85] A. Lanzaro. Microscopic flows of aqueous polyacrylamide solutions: a quantitative study. *PhD Thesis*, 2011.

[86] P.G. de Gennes. *Scaling concepts in polymer physics*. Cornell Univ Pr, 1979.

[87] M. Doi and S.F. Edwards. *The theory of polymer dynamics*. Oxford University Press, USA, 1988.

[88] CF Curtiss and R.B. Bird. A kinetic theory for polymer melts. I. The equation for the single-link orientational distribution function. *The Journal of Chemical Physics*, 74:2016, 1981.

[89] R.B. Bird, C.F. Curtiss, R.C. Armstrong, and O. Hassager. Dynamics of polymeric liquids, volume 2. *Fluid Dynamics*, 2, 1987.

[90] H.R. Warner Jr. Kinetic theory and rheology of dilute suspensions of finitely extendible dumbbells. *Industrial & Engineering Chemistry Fundamentals*, 11(3):379–387, 1972.

[91] A. Peterlin. Hydrodynamics of macromolecules in a velocity field with longitudinal gradient. *Journal of Polymer Science Part B: Polymer Letters*, 4(4), 1966.

[92] MD Chilcott and JM Rallison. Creeping flow of dilute polymer solutions past cylinders and spheres. *J. Non-Newtonian Fluid Mech*, 29:381–432, 1988.

[93] M. Herrchen and H.C.
"Ottinger. A detailed comparison of various FENE dumbbell models. *Journal of Non-Newtonian Fluid Mechanics*, 68(1):17–42, 1997.

[94] EJ Hinch. Uncoiling a polymer molecule in a strong extensional flow. *Journal of Non-Newtonian Fluid Mechanics*, 54:209–230, 1994.

[95] RG Larson, H. Hu, DE Smith, and S. Chu. Brownian dynamics simulations of a DNA molecule in an extensional flow field. *Journal of Rheology*, 43:267, 1999.

[96] EJ Hinch. Mechanical models of dilute polymer solutions in strong flows. *Physics of Fluids*, 20:S22, 1977.

[97] PG De Gennes. Coil-stretch transition of dilute flexible polymers under ultrahigh velocity gradients. *Simple views on condensed matter*, page 158, 2003.

[98] J. Remmelgas, P. Singh, and L.G. Leal. Computational studies of nonlinear elastic dumbbell models of Boger fluids in a cross-slot flow. *Journal of Non-Newtonian Fluid Mechanics*, 88(1-2):31–61, 1999.

[99] KP Jackson, K. Walters, and RW Williams. A rheometrical study of Boger fluids. *Journal of Non-Newtonian Fluid Mechanics*, 14:173–188, 1984.

[100] EJ Hinch. Mechanical models of dilute polymer solutions for strong flows with large polymer deformations. *Polymères et Lubrification*, pages 351–372.

[101] M. Keentok, AG Georgescu, AA Sherwood, and RI Tanner. The measurement of the second normal stress difference for some polymer solutions. *Journal of Non-Newtonian Fluid Mechanics*, 6(3-4):303–324, 1980.

[102] MW Johnson et al. A model for viscoelastic fluid behavior which allows non-affine deformation. *Journal of Non-Newtonian Fluid Mechanics*, 2(3):255–270, 1977.

[103] N.P. Thien and R.I. Tanner. A new constitutive equation derived from network theory. *Journal of Non-Newtonian Fluid Mechanics*, 2(4):353–365, 1977.

[104] R. Guénette and M. Fortin. A new mixed finite element method for computing viscoelastic flows. *Journal of non-newtonian fluid mechanics*, 60(1):27–52, 1995.

[105] P. Constantin. On the Euler equations of incompressible fluids. *BULLETIN-AMERICAN MATHEMATICAL SOCIETY*, 44(4):603, 2007.

[106] CM Rhie and WL Chow. Numerical study of the turbulent flow past an airfoil with trailing edge separation. *AIAA Journal(ISSN 0001-1452)*, 21:1525–1532, 1983.

[107] BP Leonard. Simple high-accuracy resolution program for convective modelling of discontinuities. *International Journal for Numerical Methods in Fluids*, 8(10):1291–1318, 1988.

[108] PH Gaskell and AKC Lau. Curvature-compensated convective transport: SMART, a new boundedness-preserving transport algorithm. *International Journal for Numerical Methods in Fluids*, 8(6):617–641, 1988.

[109] A. Harten. High resolution schemes for hyperbolic conservation laws* 1. *Journal of computational physics*, 49(3):357–393, 1983.

[110] MA Alves, FT Pinho, and PJ Oliveira. Effect of a high-resolution differencing scheme on finite-volume predictions of viscoelastic flows. *Journal of Non-Newtonian Fluid Mechanics*, 93(2-3):287–314, 2000.

[111] B. Yu, Y. Kawaguchi, S. Takagi, and Y. Matsumoto. DNS study on the drag reducing flow with additives employing Giesekus fluid model and MINMOD scheme: effect of Weissenberg number on the turbulent flow structure. In *7th Symposium on Smart Control of Turbulence, University of Tokyo*, 2001.

[112] B. Yu and Y. Kawaguchi. Effect of Weissenberg number on the flow structure: DNS study of drag-reducing flow with surfactant additives. *International Journal of Heat and Fluid Flow*, 24(4):491–499, 2003.

[113] D. Rajagopalan, R.C. Armstrong, and R.A. Brown. Finite element methdos for calculation of steady, viscoelastic flow using constitutive equations with a Newtonian viscosity. *Journal of Non-Newtonian Fluid Mechanics*, 36:159–192, 1990.

[114] M. A. Mendelson, P. W. Yeh, R. A. Brown, and R. C. Armstrong. Approximation error in finite element calculation of viscoelastic fluid flows. *Journal of Non-Newtonian Fluid Mechanics*, 10(1-2):31 – 54, 1982.

[115] R. Guénette and M. Fortin. A new mixed finite element method for computing viscoelastic flows. *Journal of Non-Newtonian Fluid Mechanics*, 60(1):27–52, 1995.

[116] RI Issa. Solution of the implicitly discretised fluid flow equations by operator-splitting. *Journal of Computational Physics*, 62(1):40–65, 1986.

[117] JH Ferziger and M. Peric. Computational Methods for Fluid Dynamics. 2002.

[118] AN Brooks and TJR Hughes. Streamline upwind/Petrov-Galerkin formulations for convection dominated flows with particular emphasis on the incompressible Navier-Stokes equations. *Computer methods in applied mechanics and engineering*, pages 199–259, 1990.

[119] N. Clemeur, RPG Rutgers, and B. Debbaut. Numerical simulation of abrupt contraction flows using the Double Convected Pom–Pom model. *Journal of Non-Newtonian Fluid Mechanics*, 117(2-3):193–209, 2004.

[120] TN Phillips and AJ Williams. Viscoelastic flow through a planar contraction using a semi-Lagrangian finite volume method* 1. *Journal of Non-Newtonian Fluid Mechanics*, 87(2-3):215–246, 1999.

[121] M. Aboubacar, H. Matallah, and MF Webster. Highly elastic solutions for Oldroyd-B and Phan-Thien/Tanner fluids with a finite volume/element method: planar contraction flows. *Journal of Non-Newtonian Fluid Mechanics*, 103(1):65–103, 2002.

[122] S. Nigen and K. Walters. Viscoelastic contraction flows: comparison of axisymmetric and planar configurations. *Journal of Non-Newtonian Fluid Mechanics*, 102(2):343–359, 2002.

[123] EJ Hinch. The flow of an Oldroyd fluid around a sharp corner. *Journal of Non-Newtonian Fluid Mechanics*, 50(2-3):161–171, 1993.

[124] M. Mackley. Stretching polymer chains. *Rheologica acta*, 49(5):443–458, 2010.

[125] S.H. Spiegelberg and G.H. McKinley. Stress relaxation and elastic decohesion of viscoelastic polymer solutions in extensional flow* 1. *Journal of Non-Newtonian Fluid Mechanics*, 67:49–76, 1996.

[126] NV Orr and T. Sridhar. Stress relaxation in uniaxial extension* 1. *Journal of Non-Newtonian Fluid Mechanics*, 67:77–103, 1996.

[127] P.S. Doyle, E.S.G. Shaqfeh, G.H. McKinley, and S.H. Spiegelberg. Relaxation of dilute polymer solutions following extensional flow1. *Journal of Non-Newtonian Fluid Mechanics*, 76(1-3):79–110, 1998.

[128] S.J. Haward. Buckling instabilities in dilute polymer solution elastic strands. *Rheologica Acta*, pages 1–7.

[129] RJ Poole, MA Alves, and PJ Oliveira. Purely elastic flow asymmetries. *Physical review letters*, 99(16):164503, 2007.

[130] G.N. Rocha, R.J. Poole, M.A. Alves, and P.J. Oliveira. On extensibility effects in the cross-slot flow bifurcation. *Journal of Non-Newtonian Fluid Mechanics*, 156(1-2):58–69, 2009.

[131] S.J. Haward, J.A. Odell, Z. Li, and X.F. Yuan. Extensional rheology of dilute polymer solutions in oscillatory cross-slot flow: the transient behaviour of birefringent strands. *Rheologica acta*, 49(6):633–645, 2010.

[132] MJ Miles and A. Keller. Conformational relaxation time in polymer solutions by elongational flow experiments: 2. Preliminaries of further developments: chain retraction; identification of molecular weight fractions in a mixture. *Polymer*, 21(11):1295–1298, 1980.

[133] C.J.S. Petrie and M.M. Denn. Instabilities in polymer processing. *AIChE Journal*, 22(2):209–236, 1976.

[134] M.S.N. Oliveira, L.E. Rodd, G.H. McKinley, and M.A. Alves. Simulations of extensional flow in microrheometric devices. *Microfluidics and Nanofluidics*, 5(6):809–826, 2008.

[135] D. Drikakis. Bifurcation phenomena in incompressible sudden expansion flows. *Physics of Fluids*, 9:76, 1997.

[136] J.P. Rothstein and G.H. McKinley. Extensional flow of a polystyrene Boger fluid through a 4: 1: 4 axisymmetric contraction/expansion. *Journal of Non-Newtonian Fluid Mechanics*, 86(1-2):61–88, 1999.

[137] J.P. Rothstein and G.H. McKinley. The axisymmetric contraction-expansion: the role of extensional rheology on vortex growth dynamics and the enhanced pressure drop. *Journal of Non-Newtonian Fluid Mechanics*, 98(1):33–63.

[138] LE Rodd, JJ Cooper-White, DV Boger, and GH McKinley. Role of the elasticity number in the entry flow of dilute polymer solutions in micro-fabricated contraction geometries. *Journal of Non-Newtonian Fluid Mechanics*, 143(2-3):170–191, 2007.

[139] RG Larson, E.S.G. Shaqfeh, and SJ Muller. A purely elastic instability in Taylor–Couette flow. *Journal of Fluid Mechanics*, 218:573–600, 1990.

[140] O. Hassager. Working group on numerical techniques. In *Proceedings of the Vth Workshop on Numerical Methods in Non-Newtonian Flow, J. Non-Newtonian Fluid Mech*, volume 29, pages 2–5, 1988.

[141] P. Neofytou and D. Drikakis. Non-Newtonian flow instability in a channel with a sudden expansion. *Journal of Non-Newtonian Fluid Mechanics*, 111(2-3):127–150, 2003.

[142] Z. Li. Non-Linear Dynamics of Polymer Solutions in Microfluidics. *PhD Thesis*, 2010.

[143] POLYFLOW Users Manual, Version 3.12.0, ANSYS Inc. *Canonsburg, Pennsylvania*, 2008.

[144] JM Marchal and MJ Crochet. A new mixed finite element for calculating viscoelastic flow. *Journal of Non-Newtonian Fluid Mechanics*, 26(1):77–114, 1987.

[145] M.S.N. Oliveira, L.E. Rodd, G.H. McKinley, and M.A. Alves. Simulations of extensional flow in microrheometric devices. *Microfluidics and Nanofluidics*, 5(6):809–826, 2008.

[146] G.M. Harrison, J. Remmelgas, and L.G. Leal. The dynamics of ultradilute polymer solutions in transient flow: Comparison of dumbbell-based theory and experiment. *Journal of Rheology*, 42:1039, 1998.

[147] X.J. Fan and R. Byron Bird Michael. Configuration-dependent friction coefficients and elastic dumbbell rheology. *Journal of Non-Newtonian Fluid Mechanics*, 18(3):255–272, 1985.